

**CARRIER TRANSPORT IN HYBRID LEAD HALIDE PEROVSKITES  
STUDIED BY ULTRAFAST PUMP-PROBE MICROSCOPY**

by

**Jordan M. Snaider**

**A Dissertation**

*Submitted to the Faculty of Purdue University*

*In Partial Fulfillment of the Requirements for the degree of*

**Doctor of Philosophy**



Department of Chemistry

West Lafayette, Indiana

May 2019

**THE PURDUE UNIVERSITY GRADUATE SCHOOL**  
**STATEMENT OF COMMITTEE APPROVAL**

Dr. Libai Huang, Chair

Department of Chemistry

Dr. Garth Simpson

Department of Chemistry

Dr. Christina Li

Department of Chemistry

Dr. Corey Thompson

Department of Chemistry

**Approved by:**

Dr. Christine A. Hrycyna

Head of the Graduate Program

*To my grandfather, Buddy Rankin...*

## ACKNOWLEDGMENTS

First and foremost, I would like to extend my sincerest gratitude my Ph.D. advisor, my mentor, and my friend, Professor Libai Huang. Her hard work and dedication towards our research allowed me to flourish, as she went above and beyond in guiding me through my graduate school career. Libai's extensive depth of knowledge has shaped me into a substantially better spectroscopist and microscopist, which is remarkable since I had no prior knowledge in the field of ultrafast spectroscopy/microscopy. Aside from her scientific expertise, Libai has been a phenomenal life mentor, who provided priceless advice. I will always be grateful to Libai for the excellent mentoring scientifically and extremely grateful to have her as a friend.

I would like to thank my committee members, Prof. Garth Simpson, Prof. Christina Li, and Prof. Corey Thompson for their time and interests. The experience of the candidacy exam was very humbling and made me take a whole new perspective on possessing a broader range of knowledge. This played a huge role in my success at Purdue and my committee members are to thank for that.

My gratitude goes out to all our collaborators throughout my graduate career. A few names that stand out are Matthew Tantama and his group, Juan-Pablo Correa-Baena, Letian Dou, Enzheng Shi, Yao Gao, and Kai Zhu. A lot of incredible science came about from working with these scientists and I am extremely grateful to have worked with them.

Dr. Zhi Guo stands out as a major contributor to my learning experience at Purdue. As a postdoctoral member of Libai's lab, he went out of his way to teach me all he knows and take me under his wing on his projects. The hot carrier transport and cross grain transport works were heavily done by Zhi and resulted in great publications. Zhi will always be a good friend to me. Thank you!

In addition to Dr. Guo, I would like to thank all the members of Libai's lab – specifically Dr. Yan Wan, Dr. Tong Zhu, Dr. Ti Wang, Dr. Shibin Deng, and Long Yuan. They have all made my graduate career that much more enjoyable and helped me along the way. Long Yuan and I have journeyed through the Ph.D. program together and I have greatly enjoyed the friendship that we have built. He is a brilliant scientist that has taught me so much! A special thanks is extended to Dr. Deng who has answered a lot of my stupid questions and has taught me an enormous amount. Finally, I'd like to thank Dr. Tong Zhu. She has been a huge help in lab and a huge motivation to

finish strong. Aside from at work, Tong has become a dear friend of mine (and my fiancé). She is truthfully a great person and an incredible scientist.

Finally, I owe my deepest appreciation to my family – my mother (Carol), father (André), brother (Chad), sister (Sydney), grandmother (Kathleen) and soon to be wife, Christina Berti. While they might not have understood what I was working on, they certainly understood I was working towards some greater goal, by doing what I love. My absence was certainly hard for them and I thank them for the sacrifices they have made. Their support really motivated me to finish strongly and keep working hard. I love you all and thank you very much for the love and support you have given me.

## TABLE OF CONTENTS

LIST OF FIGURES .....	9
ABSTRACT .....	15
CHAPTER 1. INTRODUCTION .....	19
1.1 Solar Energy Demand .....	19
1.2 Photovoltaics .....	20
1.3 Carrier Transport .....	21
1.3.1 Direct Measurement of Carrier Transport for PV Applications .....	22
1.4 Hybrid Lead Halide Perovskites .....	23
1.4.1 Historical Background .....	23
1.4.2 Material Structure .....	24
1.4.3 Photophysical Processes .....	27
1.5 Conclusion .....	31
CHAPTER 2. MATERIAL CHARACTERIZATION METHODS .....	33
2.1 Steady-State Absorption and Reflectance .....	33
2.2 Steady-State and Time-Resolved Photoluminescence .....	34
2.3 Surface Characterization .....	35
2.4 Transient Absorption Spectroscopy .....	36
2.4.1 Global Analysis .....	37
2.5 Transient Absorption Microscopy .....	37
2.5.1 Carrier Transport .....	40
2.5.2 Spatial Precision Limiting Factors .....	41
2.5.3 Noise .....	42
CHAPTER 3. ROLE OF GRAIN BOUNDARIES IN PEROVSKITE THIN FILMS .....	43
3.1 Abstract .....	43
3.2 Introduction .....	44
3.3 Material Preparation .....	46
3.4 Material Characterization .....	47
3.5 Results and Discussion .....	48

3.5.1	Band-Edge vs. Sub-Band Gap Transient Absorption Imaging.....	48
3.5.2	Direct Visualization of Cross Grain Transport.....	55
3.6	Conclusions.....	61
CHAPTER 4. LONG RANGE HOT CARRIER TRANSPORT IN HYBRID ORGANIC-INORGANIC PEROVSKITES .....		62
4.1	Abstract.....	62
4.2	Introduction.....	62
4.3	Material Preparation.....	64
4.4	Results and Discussion .....	66
4.4.1	Determination of Hot Carrier Spectral Signature .....	66
4.4.2	Direct Visualization of Hot Carrier Transport.....	71
4.5	Conclusions.....	81
CHAPTER 5. ACCELERATION OF CARRIER TRANSPORT VIA A HOT PHONON BOTTLENECK IN HYBRID LEAD HALIDE PEROVSKITES .....		82
5.1	Abstract.....	82
5.2	Introduction.....	82
5.2.1	Hot Phonon Bottleneck.....	82
5.3	Material Preparation.....	85
5.3.1	Alkali Metal-Doped Thin Film Perovskites .....	85
5.3.2	Single Crystal MAPbI <sub>3</sub> Nanoplates.....	85
5.4	Results and Discussion .....	86
5.4.1	Observation and Impact of Low-Threshold Hot Phonon Bottleneck .....	86
5.4.2	Enhancement of Carrier Transport .....	93
5.4.3	Monte Carlo Modeling for Hot Carrier Transport.....	99
5.5	Conclusions.....	103
CHAPTER 6. COLLABORATIVE WORK ON ALLOYED PEROVSKITE THIN FILMS AND HYBRID QUANTUM WELL PEROVSKITES .....		104
6.1	Homogenization of Carrier Dynamics in Alloyed Perovskite Thin Films .....	104
6.1.1	Abstract.....	104
6.1.2	Introduction.....	104
6.1.3	Material Preparation .....	107

6.1.4	Material Characterization .....	108
6.1.5	Results and Discussion .....	108
6.1.6	Conclusion .....	115
6.2	Hybrid Perovskite Quantum Wells .....	115
6.2.1	Abstract.....	115
6.2.2	Introduction.....	116
6.2.3	Material Preparation .....	118
6.2.4	Material Characterization .....	120
6.2.5	Results and Discussion .....	121
6.2.6	Conclusion .....	129
	REFERENCES .....	130
	VITA.....	147
	PUBLICATIONS.....	148

## LIST OF FIGURES

Figure 1.1 Generalized structure of a photovoltaic cell.....	20
Figure 1.2 Generalized cubic crystal structure for ABX <sub>3</sub> perovskites.....	25
Figure 1.3 Schematic representation of the energy generation and loss pathways in MAPbI <sub>3</sub> semiconductor material.....	31
Figure 2.1 Schematic of home-built confocal PL microscope.....	35
Figure 2.2 Schematic representation of transient absorption spectroscopy setup. OPA: optical parametric amplifier; YAG: Yttrium aluminum garnet; CCD: charge-coupled device. ....	36
Figure 2.3 Schematic of home-built transient absorption microscopy set up. BS = beam splitter, AOM = acoustic optical modulator, OPA = optical parametric amplifier, APD = avalanche photodiode.....	39
Figure 3.1 XRD patterns for film 1 (red) and film 2 (black).....	47
Figure 3.2 Photoluminescent microscopy images for film 1 and film 2 showing average grain sizes of >1 μm and <500 nm for films 1 and 2, respectively. ....	48
Figure 3.3 SEM images for perovskite thin films with grain sizes > 1 μm (film 1, a) and ~200 nm (film 2, b). Scale bars represent 1 μm. (c) Absorption spectra for film 1 and film 2. (d) PL lifetime measurements for film 1 and film 2. Excitation wavelength 447 nm; fluence 0.5 μJ/cm <sup>2</sup> . (e) Ensemble transient absorption spectra at 10 ps time delays (630 nm pump) for film 1 and film 2. (f) Carrier dynamics pumped at 630 nm, probed at 755 nm and probed at 785 nm for film 1. The pump fluence is 1 μJ/cm <sup>2</sup> .....	49
Figure 3.4 Tauc plot for Film 1 (black) and Film 2 (red). Blue and green lines are tangent lines that extrapolate to the energy corresponding to the bandgap. The tauc analysis was done by determining the absorption coefficient ( $\alpha$ ) of the material from the following equation: $\alpha = (2.303 * A)/z$ , where $z$ is the thickness of the film (537 nm). Lastly, $(\alpha * hv)^2$ will be the y-axis in the tauc plot, where $hv$ is the photon energy. Film 1 has a band gap of 1.588 eV (781 nm) and Film 2 has a band gap of 1.580 eV (785 nm).....	50
Figure 3.5 Ground state bleach dynamics at various pump fluence for film 1 (left) and film 2 (right). Based upon the power dependence for film 2, any fluence less than 24 μJ/cm <sup>2</sup> will be suitable for the measurements. All powers measured for film 1 are acceptable for diffusion measurements. 1 μJ/cm <sup>2</sup> was chosen for subsequent measurements.....	52
Figure 3.6 Ground state bleach dynamics at different laser repetition rates (200 kHz – black, 400 kHz – red) for small grain sample. The resulting time between pulses are 2.5 μs (red) and 5.0 μs (black). The pump wavelength is 400 nm with a fluence of ~7μJ/cm <sup>2</sup> . ....	52
Figure 3.7 Morphological TAM images of film 1 (a) and film 2 (b) taken at a 10 ps time delay between the pump (630 nm) and probe (755 and 785 nm). Scale bars are 1 μm. (c) Carrier dynamics probed at 755 nm within a grain and at the boundary of film 1. Solid lines are fits to equation 3.2. (d) Comparing carrier dynamics probed at 785 nm at the boundary for film 1 and film 2. Solid	

lines are fits to equation 3.2. The pump fluence is  $1 \mu\text{J}/\text{cm}^2$ . The carrier lifetime at the grain boundaries is determined from the fits to be  $9 \pm 1$  and  $5 \pm 1$  ns for film 1 and film 2, respectively.

..... 53

Figure 3.8 Carrier transport confined in a grain. TAM images of the carrier transport at a time delay of 10 ps (a) and 6 ns (b and c). The probe wavelength for a) and b) are 755 nm and 785 for c). The profile of the 630 nm pump beam is denoted by the dashed line circle in the center of each image. The pump fluence is  $1 \mu\text{J}/\text{cm}^2$  for all the images. Scale bars represent  $1 \mu\text{m}$ . ..... 56

Figure 3.9 Carrier transport across a grain boundary in film 1. (a) Morphological TAM images of a perovskite thin film taken at a 10 ps time delay between the pump (630 nm) and probe (755 nm). The pump location is indicated by the dashed circle. (b) Correlated PL image of the same area as (a). (c) Carrier transport TAM images at 10 ps and 5 ns time delays. The pump wavelength is 630 nm, and the probe wavelength is 755 nm. Scale bars represent  $1 \mu\text{m}$ . (d) The carrier dynamics taken at pump-probe spatial separations of 600 (black), 1050 (blue), and 1350 nm (yellow) across the boundaries and within the grain. These areas are denoted by the corresponding colors in (a), (b) and (c). (e) Kinetic modeling of the carrier dynamics at a pump-probe separation of 1050 nm for transport across and within a grain. The red solid lines are fits to equation 3.2. .... 58

Figure 3.10 Simulation results from fitting the carrier dynamics taken at a pump probe separation of 1350 nm to obtain diffusion constants of  $0.20 \pm 0.05 \text{ cm}^2\text{s}^{-1}$  and  $0.12 \pm 0.05 \text{ cm}^2\text{s}^{-1}$  for within grain and across boundaries, respectively. The red lines are the results of fitting to equation 3.2. .... 59

Figure 3.11 Carrier transport across grain boundaries in film 2. (a) Morphological TAM images of the perovskite thin film taken at a 10 ps time delay between the pump (630 nm) and probe (755 nm). The pump location is indicated by the dashed circle. Carrier transport TAM images at 10 ps (b), 2.5 ns (c), and 5 ns (d) time delays. The pump wavelength is 630 nm, and the probe wavelength is 755 nm. Scale bars represent  $1 \mu\text{m}$ . .... 60

Figure 4.1 Illustration of hot carriers within the band structure. .... 63

Figure 4.2 Scanning electron microscopy (SEM) image of the  $\text{CH}_3\text{NH}_3\text{PbI}_3$  thin film used in this work. .... 65

Figure 4.3 Absorption and Photoluminescence spectra of the  $\text{MAPbI}_3$  investigated in this work. .... 66

Figure 4.4 Illustration depicting increasing pump photon energy to generate hot carriers. Energy selective contact is included to show to potential for extraction of hot charge carriers. .... 67

Figure 4.5 (A) Ensemble transient absorption spectra taken at 200 fs delay with different pump photon energies and change of transmission  $\Delta T/T$  was plotted. The pump fluences were calibrated to the same carrier density of  $10^{17} \text{ cm}^{-3}$ . (B) Decay-associated spectra (DAS) for a pump photon energy of 3.14 eV obtained by performing global analysis on the transient spectra. (C) Carrier density dependence of  $\Delta T/T$  of the PIA band (taken at maximum value) and that of the GSB band (4 ps time delay) for a pump photon energy of 3.14 eV and a probe energy of 1.58 eV. (D) Hot-carrier cooling dynamics obtained by subtracting the carrier relaxation kinetics driven by 3.14 eV photon excitation from those induced by 1.68 eV excitation plotted along with a biexponential fit. .... 69

- Figure 4.6 Ensemble transient absorption spectra taken at different pump-probe delays with a pump photon energy of 3.14 eV and change of transmission  $\Delta T/T$  was plotted to observe the growth of broad blue shifted PIA, as hot carriers decay..... 70
- Figure 4.7 Decay associated spectra (DAS) for pump photon energy of 1.97 eV through performing global analysis on the transient spectra..... 70
- Figure 4.8 Carrier density dependent dynamics when pump and probe beams are overlapped in the center. Pump = 3.14 eV, probe = 1.65 eV. .... 72
- Figure 4.9 TAM images probing at 1.58 eV with two pump photon energies— (A) 3.14 eV and (B) 1.97 eV— at different pump-probe delay times, as labeled. Scale bars, 1  $\mu\text{m}$ . (C) Hot-carrier distribution at 0-ps delay for 3.14 eV excitation over a radial distance obtained by averaging all angles compared to the IRF, as defined in the text. Solid lines are Gaussian fits. (D) One-dimensional TAM image profile at 1.2 ps for 3.14 eV pump excitation. The red solid line is fit as described in the text. The red dashed line in (A) indicates where the 1D distribution was obtained in (D)..... 74
- Figure 4.10 One-dimensional carrier distribution at 0 ps delay for 1.97 eV pump excitation compared to an instrument response function (IRF) =  $(\sigma^2(\text{pump}) + \sigma^2(\text{probe}))^{1/2}$  ..... 77
- Figure 4.11 One-dimensional carrier distribution at 100 ps delay for 3.14 eV pump excitation. The TAM signal was fitted as the sum of the two types of signals:  $\Delta TGSBx, t + \Delta TPIAx, t$  ..... 77
- Figure 4.12 Nonequilibrium to diffusive transport transition. (A)  $\sigma t^2$  plotted as a function of pump-probe delay time up to 6 ns for 1.97 eV and 3.14 eV pump photon energies. Linear fits are shown in dashed red lines to indicate diffusive transport with  $L^2 = \sigma t^2 - \sigma_0 t^2 = 2Dt$ . (B) Zoomed in view of (A) for the time scale up to 100 ps. (C) TAM images at 2 ps and 100 ps for 3.14 eV and 1.97 eV pump photon energies. Scale bar: 1  $\mu\text{m}$ ..... 78
- Figure 4.13 (A) Effective diffusion constant,  $D(t)$ , calculated as a function of delay time for 3.14-eV photon excitation. The red solid line is the fit to a biexponential decay function. (B) Kinetics probed at pump-probe distances as labeled for pump photon energy of 3.14 eV..... 79
- Figure 5.1 A representative scanning electron microscopy image of a RbCsMAFA perovskite thin film deposited on glass substrates used in the optical measurements..... 87
- Figure 5.2 Normalized absorption spectrum (black) and photoluminescence spectrum (red) of a RbCsMAFA perovskite thin film. .... 87
- Figure 5.3 (a) TA spectra taken at various delay times with pump photon energy of 3.10 eV at an injected carrier density  $N_0$  of  $1 \times 10^{18} \text{ cm}^{-3}$  in the RbCsMAFA thin film. (b) Symbols are time-dependent carrier temperatures at different pump photon energies and carrier densities as extracted by fitting the high-energy tail of the GSB signal in the RbCsMAFA thin film as described in the text. Solid lines are fitting to  $\tau c = \tau_0 + \rho \rho c$  as described in the text. (c) The carrier dynamics probed at the bandgap of 1.65 eV in the RbCsMAFA thin film. (d) Schematic drawing of large polaron formation and overlap of two large polarons. Figure 5.4 TA spectra taken at various delay time with pump photon energy of 2.25 eV and a carrier density of  $10^{18} \text{ cm}^{-3}$  of a RbCsMAFA perovskite thin film. .... 89

Figure 5.5 Transient absorption spectra of a RbCsMAFA perovskite thin film taken at 200 fs delay with different pump photon energies and change of transmission  $\Delta T/T$  was plotted. The pump fluences were calibrated to the same carrier density of  $10^{18} \text{ cm}^{-3}$ . ..... 90

Figure 5.6 (a) TA spectra taken at various delay times with pump photon energy of 3.10 eV at an injected carrier density  $N_0$  of  $1.2 \times 10^{18} \text{ cm}^{-3}$  in the MAPbI<sub>3</sub> single crystal. (b) Symbols are time-dependent carrier temperatures of the MAPbI<sub>3</sub> single crystal at different carrier densities as extracted by fitting the high-energy tail of the GSB signal. Solid lines are fitting to  $\tau c = \tau_0(1 + \rho \rho c)$  as described in the text. .... 91

Figure 5.7 Morphological transient absorption microscopy (TAM) image of a RbCsMAFA thin film taken at 0 ps time delay with a pump photon energy of 3.10 eV and a probe photon energy of 1.65 eV. In this mode of TAM imaging, the pump and probe beams are always spatially overlapped and scan simultaneously. The intensity presents the TA signal at each position. .... 94

Figure 5.8 (a) The TAM images of the carrier transport at various delay times. Probe energy = 1.65 eV, pump energy = 3.10 eV,  $N_0 = 1 \times 10^{18} \text{ cm}^{-3}$ . Color scale represents the intensity of pump-induced differential transmission ( $\Delta T$ ) of the probe and every image has been normalized by peak value. Scale bar: 500 nm. (b) Cross-sections of the TAM images shown in (a) fitted with Gaussian functions, with the maximum  $\Delta T$  signal normalized. (c)  $\sigma t^2 - \sigma_0 ps^2$  plotted as a function of pump-probe delay time of RbCsMAFA at different initial carrier densities and pump energies. Probe energy = 1.65 eV. Solid lines are the linear fits described in the text. (d)  $\sigma t^2 - \sigma_0 ps^2$  plotted as a function of pump-probe delay time of a MAPbI<sub>3</sub> single-crystal nanoplate at different initial carrier densities. Probe energy = 1.65 eV. Solid lines are the linear fits described in the text. (e)  $\sigma t^2 - \sigma_0 ps^2$  plotted as a function of pump-probe delay time of a GaAs single crystal at different injected carrier densities. Probe energy = 1.45 eV. Solid line is the linear fits described in the text. .... 95

Figure 5.9 Carrier dynamics at different injected carrier densities when pump and probe beams are overlapped in space. (a) RbCsMAFA thin film. (b) MAPbI<sub>3</sub> single crystal. The similar kinetics with  $N_0$  from  $5 \times 10^{17} \text{ cm}^{-3}$  to  $3 \times 10^{18} \text{ cm}^{-3}$  suggest that annihilation effects are negligible for the carrier density range for the RbCsMAFA thin film and the MAPbI<sub>3</sub> single crystal. .... 97

Figure 5.10 The effective diffusion constant for the 3.10 eV excitation for the RbCsMAFA thin film (a) and the MAPbI<sub>3</sub> single crystal (b). The dashed lines denote the equilibrium diffusion constant. .... 98

Figure 5.11 (a) Schematic showing the scattering process (b) Simulated 2D maps of 5000 carriers at time delay of 5 ps (left), 100 ps (middle), 500 ps (right). The scale bar is 0.5  $\mu\text{m}$ . (c) Time evolution of the simulated (open) and experimental (solid) spatial profile with  $N_0$  of  $3 \times 10^{18} \text{ cm}^{-3}$  and  $5 \times 10^{17} \text{ cm}^{-3}$  respectively. (d)  $\tau sm^*$  as a function of temperature extracted from the simulations shown in (c). .... 100

Figure 6.1.1 (A) Schematic of the perovskite solar cells studied, accompanied by (B) the cross-sectional TEM for CsRb-I/Br device. .... 109

Figure 6.1.2 Device power conversion efficiency for various alkali metal perovskites at different stoichiometric ratios of  $\text{PbX}_2:\text{AX}$ . .... 110

Figure 6.1.3 Time-resolved photoluminescence decay for various alkali metal doped perovskite compositions ..... 111

Figure 6.1.4 (A-D) halide distribution by X-ray fluorescence imaging, indicating homogenous distribution of Br upon alkali metal incorporation. Br-poor areas have been marked. (E-H) Transient absorption microscopy images of the relative change in TA signal  $[\Delta T(0 \text{ ps}) - \Delta T(5 \text{ ns})] / \Delta T(0 \text{ ps})$ , mapped as function of sample location. The pump wavelength is at 700 nm with a pump fluence of  $10 \mu\text{J}/\text{cm}^2$ . All scale bars are  $1 \mu\text{m}$ . ..... 112

Figure 6.1.5 The relative change of TA signal in samples with different alkali ion additions. Distribution is taken from a line of data points off of the maps shown in Figure 6.1.4 E-H..... 114

Figure 6.1.6 Charge carrier dynamics as measured by TAM. (A-D), the relative change in TA signal  $[\Delta T(0 \text{ ps}) - \Delta T(5 \text{ ns})] / \Delta T(0 \text{ ps})$  is mapped as function of sample location. The pump wavelength is at 700 nm with a pump fluence of  $10 \mu\text{J}/\text{cm}^2$ . The corresponding time resolved traces below each TAM panel show carrier dynamics taken at positions as indicated. The perovskites studied are: MAFA (A, E), 5% CsMAFA (B, F), 5% RbMAFA (C, G) and 5% Cs 5% RbMAFA (D, H). Scale bars:  $1 \mu\text{m}$ . ..... 114

Figure 6.2.1 Schematic illustration of a two-dimensional hybrid halide perovskite ..... 117

Figure 6.2.2 Chemical structures of the newly designed conjugated organic ligands with an ammonium ion as the end group..... 121

Figure 6.2.3 (a) Optical microscopy images of the assembled 2D crystals grown on  $\text{SiO}_2/\text{Si}$  substrates:  $(2\text{T})_2\text{PbI}_4$  (a1),  $(4\text{Tm})_2\text{PbI}_4$  (a2),  $(4\text{TCNm})_2\text{PbI}_4$  (a3),  $(\text{BTm})_2\text{PbI}_4$  (a4). All scale bars are  $10 \mu\text{m}$ . The insets are images for mono-layer thick single quantum well structures. All scale bars in the insets are  $5 \mu\text{m}$ . (b) Corresponding PL image of the assembled 2D crystals under UV excitation. All scale bars are  $10 \mu\text{m}$ . The insets are the PL images for the corresponding mono-layer thick single quantum well structures. All scale bars in the insets are  $5 \mu\text{m}$ . (c) Corresponding steady state PL spectra of the mono-layers (red curves), bulk crystals (dark red curves). In c1 inset,  $(\text{BA})_2\text{PbI}_4$  mono-layers (grey solid curves) and bulk crystals (grey dashed curves) are shown for comparison. In c2 and c3 insets, the PL for the 4Tm and 4TCNm ligands (blue curves) are shown for comparison. The weak signals come from both the organic ligands and the perovskite layers. (d) Semi-quantified band structures of the hybrid 2D perovskite superlattices..... 123

Figure 6.2.4 (a) Absorption spectra of polycrystalline thin films of 2D hybrid halide perovskites based on conjugated ligands. (b) Absorption spectra of polycrystalline thin films of 2D hybrid halide perovskites based on BT conjugated ligands with different thickness of the perovskite layer. (c) Absorption spectra of thin films of pure organic conjugated ligands. .... 124

Figure 6.2.5 (a) Steady state photoluminescence spectra of thin films of pure organic conjugated ligands. (b) Steady state photoluminescence spectra of thin films of 2D hybrid halide perovskite based on conjugated ligands. Normalized steady state photoluminescence spectra of thin films of 4T (c) and 4TCN (d) based 2D perovskites. .... 125

Figure 6.2.6 (a) Transient absorption spectra of a  $(\text{BA})_2\text{PbI}_4$  crystal. (b) Transient absorption spectra of a  $(2\text{T})_2\text{PbI}_4$  crystal. (c) Transient absorption spectra of a  $(4\text{Tm})_2\text{PbI}_4$  crystal. (d) Transient absorption spectra of a  $(4\text{TCNm})_2\text{PbI}_4$  crystal. (e) Transient absorption spectra of a  $(\text{BTm})_2\text{PbI}_4$  crystal..... 126

Figure 6.2.7 (a) Time-resolved PL spectra of  $(2T)_2PbI_4$  (a1),  $(4Tm)_2PbI_4$  (a2),  $(4TCNm)_2PbI_4$  (a3),  $(BTm)_2PbI_4$  (a4) 2D crystals. The PL decay curves for  $(BA)_2PbI_4$  (grey dashed curves) and pure organic ligands (deep grey curves) are shown for comparison. (b) Bleach dynamics and extraction of the energy and charge transfer time of the corresponding 2D crystals. The blue curves indicate the difference of exciton bleaching dynamics between the new 2D perovskites with  $(BA)_2PbI_4$ . Energy and charge transfer times were extracted based on these data. .... 127

Figure 6.2.8 Photos of 2D hybrid halide perovskite thin films with different organic ligands under UV irradiation before (top) and after (bottom) immersion in water. From left to right:  $(BA)_2PbI_4$ ,  $(2T)_2PbI_4$ ,  $(4Tm)_2PbI_4$ ,  $(4TCNm)_2PbI_4$ ,  $(BTm)_2PbI_4$ . .... 128

## ABSTRACT

Author: Snaider, Jordan, M. PhD

Institution: Purdue University

Degree Received: May 2019

Title: Carrier Transport in Hybrid Lead Halide Perovskites Studied by Ultrafast Pump-Probe Microscopy

Committee Chair: Libai Huang

Insight into the nanoscale carrier transport in the rapidly developing class of solution-processed semiconductors known as metal halide perovskites is the focal point for these studies. Further advancement in fundamentally understanding photophysical processes associated with charge carrier transport is needed to realize the true potential of perovskites for photovoltaic applications. In this work, we study photogenerated carrier transport to understand the underlying transport behavior of the material on the 10s to 100s nanometer lengthscales. To study these processes, we employ a temporally-resolved and spatially-resolved technique, known as transient absorption microscopy, to elucidate the charge carrier dynamics and propagation associated with metal halide perovskites. This technique provides a simultaneous high temporal resolution (200 fs) and spatial resolution (50 nm) to allow for direct visualization of charge carrier migration on the nanometer length scale. There are many obstacles these carriers encounter between photogeneration and charge collection such as morphological effects (grain boundaries) and carrier interactions (scattering processes). We investigate carrier transport on the nanoscale to understand how morphological effects influence the materials transport behavior. Morphological defects such as voids and grain boundaries are inherently small and traditionally difficult to study directly. Further, because carrier cooling takes place on an ultrafast time scale (fs to ps), the combined spatial and temporal resolution is necessary for direct probing of hot (non-equilibrium) carrier transport. Here we investigate a variety of ways to enhance carrier transport lengthscales by studying how non-equilibrium carriers propagate throughout the material, as well as, carrier cooling mechanisms to extend the non-equilibrium regime.

For optoelectronic devices based on polycrystalline semiconducting thin films, grain boundaries are important to consider since solution-based processing results in the formation of well-defined grains. In Chapter 3, we investigate equilibrium carrier transport in metal halide

perovskite thin films that are created via the highly desired solution processing method. Carrier transport across grain boundaries is an important process in defining efficiency due to the literary discrepancies on whether the grains limit carrier transport or not. In this work, we employ transient absorption microscopy to directly measure carrier transport within and across the boundaries. By selectively imaging sub-bandgap states, our results show that lateral carrier transport is slowed down by these states at the grain boundaries. However, the long carrier lifetimes allow for efficient transport across the grain boundaries. The carrier diffusion constant is reduced by about a factor of 2 for micron-sized grain samples by the grain boundaries. For grain sizes on the order of  $\sim 200$  nm, carrier transport over multiple grains has been observed within a time window of 5 ns. These observations explain both the shortened photoluminescence lifetimes at the boundaries as well as the seemingly benign nature of the grain boundaries in carrier generation. The results of this work provide insight into why this defect tolerant material performs so well.

Photovoltaic performance (power conversion efficiency) is governed by the Shockley-Queisser limit which can be overcome if hot carriers can be harvested before they thermalize. To convert sunlight to usable electricity, the photogenerated charge carriers need to migrate long distances and or live long enough to be collected. It is unclear whether these hot carriers can migrate a long enough distance for efficient collection. In Chapter 4, we report direct visualization of hot-carrier migration in methylammonium lead iodide ( $\text{CH}_3\text{NH}_3\text{PbI}_3$ ) thin films by ultrafast transient absorption microscopy. This work demonstrates three distinct transport regimes. (i) Quasiballistic transport, (ii) nonequilibrium transport, and (iii) diffusive transport. Quasiballistic transport was observed to correlate with excess kinetic energy, resulting in up to 230 nanometers of transport distance that could overcome grain boundaries. The nonequilibrium transport persisted over tens of picoseconds and  $\sim 600$  nanometers before reaching the diffusive transport limit. These results suggest potential applications of hot-carrier devices based on hybrid perovskites to ultimately overcome the Shockley-Queisser limit.

In the next work, we investigated a way to extend non-equilibrium carrier lifetime, which ultimately corresponds to an accelerated carrier transport. From the knowledge of the hot carrier transport work, we showed a proof of concept that the excess kinetic energy corresponds to long range carrier transport. To further develop the idea of harvesting hot carriers, one must investigate a way to make the carriers stay hot for a longer period (i.e. cool down slower). In Chapter 5, we slow down the cooling of hot carriers via a phonon bottleneck, which points toward the potential

to overcome the Shockley-Queisser limit. Open questions remain on whether the high optical phonon density from the bottleneck impedes the transport of these hot carriers. We show a direct visualization of hot carrier transport in the phonon bottleneck regime in both single crystalline and polycrystalline lead halide perovskites, more specifically, a relatively new class of alkali metal doped perovskites (RbCsMAFA), which has one of the highest power conversion efficiencies. Remarkably, hot carrier diffusion is enhanced by the presence of a phonon bottleneck, the exact opposite from what is observed in conventional semiconductors such as GaAs. These results showcase the unique aspects of hot carrier transport in hybrid perovskites and suggest even larger potential for hot carrier devices than previously envisioned by the initial results presented in Chapter 4.

The final chapter will be divided into two sections, as we summarize and highlight our collaborative efforts towards homogenization of carrier dynamics via doping perovskites with alkali metals and our work on two-dimensional hybrid quantum well perovskites. Further studies on the champion solar cell (RbCsMAFA) were performed to elucidate the role inorganic cations play in this material. By employing transient absorption microscopy, we show that alkali metals  $\text{Rb}^+$  and  $\text{Cs}^+$  are responsible for inducing a more homogenous halide ( $\text{I}^-$  and  $\text{Br}^-$ ) distribution, despite the partial incorporation into the perovskite lattice. This translates into improved electronic dynamics, including fluorescence lifetimes above  $3 \mu\text{s}$  and homogenous carrier dynamics, which was visualized by ultrafast microscopy. Additionally, there is an improvement in photovoltaic device performance. We find that while Cs cations tend to distribute homogeneously across the perovskite grain, Rb and K cations tend to phase segregate at precursor concentrations as low as 1%. These precipitates have a counter-productive effect on the solar cell, acting as recombination centers in the device, as argued from electron beam-induced current measurements. Remarkably, the high concentration of Rb and Cs agglomerations do not affect the open-circuit voltage, average lifetimes, and photoluminescence distribution, further indicating the perovskite's notorious defect tolerance.

A new class of high-quality two dimensional organic-inorganic hybrid perovskite quantum wells with tunable structures and band alignments was studied. By tuning the functionality of the material, the strong self-aggregation of the conjugated organic molecules can be suppressed, and 2D organic-halide perovskite superlattice crystals and thin films can be easily obtained via one-step solution-processing. We observe energy transfer and charge transfer between adjacent

organic and inorganic layers, which is extremely fast and efficient (as revealed by ultrafast spectroscopy characterizations). Remarkably, these 2D hybrid perovskite superlattices are stable, due to the protection of the bulky hydrophobic organic groups. This is a huge step towards the practicality of using perovskites for optoelectronics, since stability is always a huge concern with water-sensitive materials. The molecularly engineered 2D semiconductors are on par with III-V quantum wells and are promising for next-generation electronics, optoelectronics, and photonics.

## CHAPTER 1. INTRODUCTION

### 1.1 Solar Energy Demand

In our current society, power consumption is growing rapidly to keep up with the further advancement of technology. According to the IEA (International Energy Agency), the world primary energy consumption was about 18 TWh (terawatt-hour) in 2013 and growing each year.<sup>1</sup> The majority (~85%) of our tremendous power consumption is generated by fossil fuels, while solar energy isn't being used to its full potential.<sup>2,3</sup> For example, the annual global energy potential from the sun is about 23,000 TW and society only generated about 4% of its energy from all renewable sources (wind, solar, tide, thermal, etc.).<sup>4</sup> An attractive source of renewable energy is solar energy, which is a clean and abundant source. The 23,000 TW of power generated annually is far greater than human consumption, thus it is a heavily desired form of renewable energy. Aside from the promising benefits of solar energy, there still lacks fundamental research into the many challenges associated with the light to power conversion and utilization. These challenges are heavily investigated by researchers all over the world, in efforts to utilize the full potential of the ever so promising solar energy.

To successfully utilize the power of the sun as a renewable energy source, one must understand the solar energy conversion process on a fundamental physical level. Light from the sun (photons) with an associated energy is absorbed by a semiconductor material. At this instant, the energy of radiation is captured as excited electron-hole pairs, formally known as "excitons". The excited electrons and holes are ultimately extracted for conversion to a useful form of energy (electrical power). A more technical and in-depth description of the physical processes associated with solar energy conversion will be elaborated in later sections.

## 1.2 Photovoltaics

There are many challenges to the tremendous potential of solar power as an alternative energy source remaining. The “golden triangle” for solar cells is cost, efficiency, and stability. To efficiently harvest the abundance of free solar energy is quite difficult. In the early 1960’s, William Shockley and Hans-Joachim Queisser determined the maximum theoretical efficiency of a single junction solar cell to be ~30% at bandgap energy of 1.1 eV.<sup>5</sup> This theoretical cap on efficiency is formally known as the Shockley-Queisser limit and it simply examines the amount of electrical energy that is extracted per photon of incident sunlight. The low conversion efficiency takes into consideration possible pathways for power to be lost. Such pathways for power loss include recombination, spectral losses, impedance matching, and limited mobility.<sup>6-8</sup>

The generalized structure of a photovoltaic (PV) cell is depicted by Figure 1.1. The main components of the PV cell are the anode, cathode, hole transport layer (HTL), electron transport layer (ETL), and the active layer. The ETL/anode is typically titanium dioxide (TiO<sub>2</sub>) on a conductive glass substrate, such as FTO (fluorine doped tin oxide)

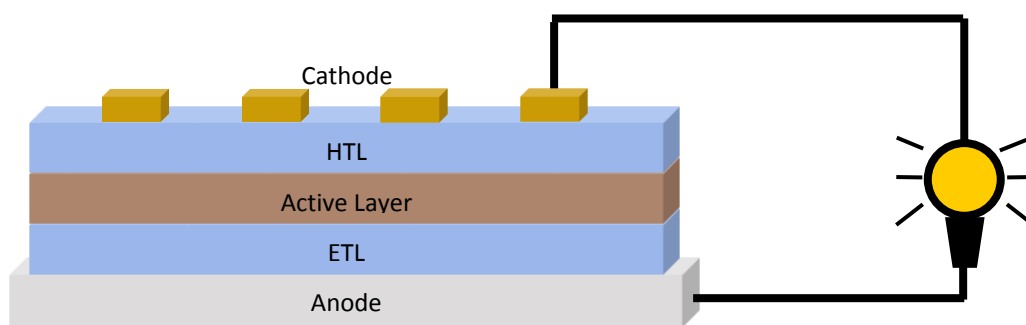


Figure 1.1 Generalized structure of a photovoltaic cell

glass.<sup>9</sup> The HTL/cathode is typically comprised of a material such as spiro-OMeTAD (2,2',7,7'-Tetrakis-(N,N-di-4-methoxyphenylamino)-9,9'-spirobifluorene) with gold contacts on top. The

primary focus of this work is on the active layer in a photovoltaic cell. The active layer is the material where light is absorbed, excitons are created, charge is separated and diffused to the collection sites. The collection of charges will complete the process and solar energy is now converted to a useful form of electricity. To achieve a highly efficient solar cell, there must exist a fundamental understanding of the underlying photophysics in the active layer. This work sets out to study how the carrier transport behavior of the active layer material.

### 1.3 Carrier Transport

A crucial factor in photovoltaic performance (power conversion efficiency) is the carrier diffusion length. From the corresponding equation (Eq. 1.1), we can see that carrier diffusion length ( $L_D$ ) is dependent on the charge carrier's lifetime,  $\tau$ , and diffusion coefficient,  $D$ .<sup>10, 11</sup>  $L_D$  is a critical parameter for photovoltaic operation because it directly influences the power conversion efficiency of charge collection in a solar cell device.<sup>10</sup>

$$L_D = \sqrt{D\tau} \quad (1.1)$$

It is particularly useful to gain insight into the carrier diffusion length by directly measuring the diffusion coefficient and the carrier lifetime. The determination of how charge moves in photovoltaic materials and how altering device fabrication procedures (material processing)<sup>12-16</sup> is critical for understanding what is limiting the power conversion efficiency. Additionally, since diffusion of charge occurs in any semiconductor due to thermal energy and energy from absorption of photons, even with no external electric field applied, it is important to study carrier diffusion on this fundamental level. There exist optical techniques to experimentally measure information

about how charges are propagating throughout a photovoltaic material, which will be expanded upon in the next section.

### 1.3.1 Direct Measurement of Carrier Transport for PV Applications

The measurement of carrier transport is crucial for PV applications to further advance and gain insight into fundamental material properties on the nanoscale. Indirect methods of measuring carrier transport lengths have been previously studied.<sup>17-20</sup> Such indirect measurements are typically based on a confocal photoluminescence (PL) for excitation and a wide field detection of the diffusion throughout the material.<sup>17</sup> There are a few drawbacks to relying on PL to study carrier transport. PL microscopy-based approaches are limited in that they only account for the emissive species present. Time resolution is another challenge for PL based measurements, since the resolution is typically on the order of 50 – 100 ps. This time scale is not sufficient enough to study fast processes such as efficient energy transfer, non-equilibrium carrier transport, and equilibrium carrier transport in the femtosecond time scale range. Direct measurement of carrier transport throughout a material has many challenges such as the requirement for high spatial and temporal resolutions, which are necessary due to the inherently short length scales that are associated with material defects.

To achieve such high temporal and spatial resolution, we utilize transient absorption microscopy (TAM) to study carrier transport on an ultrafast time scale and the nanometer length scale.<sup>21, 22</sup> This ultrafast technique addresses the aforementioned challenges associated with PL imaging techniques, by probing/investigating both emissive and non-emissive species and improving the time resolution to sub-ps. Ultrafast pump probe techniques such as TAM and transient absorption spectroscopy are particularly useful in gaining insight into the carrier diffusion length since we can directly measure the carrier diffusion coefficient and charge carrier lifetime

with high resolution temporally and spatially. An in-depth review of nonlinear ultrafast microscopy has been recently reported.<sup>23, 24</sup> In this dissertation, we focus on applying TAM as a direct approach to investigate carrier transport on the nanoscale with high temporal and spatial precision. The 200 fs temporal resolution and 50 nm spatial precision allows us to directly visualize carrier propagation in materials used for photovoltaic applications. This approach promotes the investigation into factors that limit carrier mobility, such as material defects (grain boundaries) and allows for a fundamental understanding of the behavior of carriers on the nanoscale.

## 1.4 Hybrid Lead Halide Perovskites

### 1.4.1 Historical Background

The term perovskite corresponds to a class of materials that fall under the same general crystallographic form. The material stoichiometry in the general form is  $ABX_3$ . In 1839, the naturally occurring  $CaTiO_3$  (calcium titanate) was discovered which led to a plethora of synthetic perovskite materials that exhibit unique properties.<sup>25</sup> Synthetic titanate perovskites were initially investigated for the application of pigmentation in paints.<sup>26, 27</sup> In the mid-1940's, the crystal structure of  $BaTiO_3$  (barium titanate) was confirmed<sup>28</sup> and the material was shown to have unique electronic properties, such as ferroelectricity, which sparked a broad interest in perovskite materials.<sup>29</sup> C.K. Møller determined the structure of the synthetic cesium lead halide perovskites ( $CsPbX_3$ ) and observed its photoconductivity for the first time, in the 1950's.<sup>30</sup> A German scientist (D. Weber) developed the first organic-inorganic hybrid halide perovskite in 1978 by replacing the cesium cations with an organic molecule (methylammonium ion).<sup>31</sup> At the time, the true capabilities of the methylammonium lead halide were unknown.

The 1990's began the first experiments demonstrating the photophysical properties of perovskites, such as the luminescent properties of layer perovskite materials.<sup>32, 33</sup> Once the unique optical and electronic properties of these perovskite became apparent, new findings emerged for applications such as organic-inorganic light emitting diodes and as thin film field effect transistors.<sup>32-39</sup> Since the first solar cell applications in 2009, where the power conversion efficiency was a mere 3.8%,<sup>40</sup> there has been tremendous growth to present day. To date, there have been perovskite solar cells with power conversion efficiencies as high as 22.7%.<sup>41-43</sup> The immense amount of research into the improvement of perovskite solar cells has rapidly increased power conversion efficiency and provides even more promise for the future of this material.<sup>43</sup>

#### 1.4.2 Material Structure

The chemical and crystal structure of perovskites plays an important role in the unique properties that are exhibited. While the material structure is not the focus of this dissertation, it seems important to give a concise, insightful introduction into the structure. As previously mentioned, perovskites follow the general stoichiometry of  $ABX_3$ . Each letter refers to a distinct lattice position (A site, B site, and X site), which makes up the perovskite structure, shown in Figure 1.2. These materials are crystallized from organic halide and metal halide salts to form perovskite crystals in which the A site is the monovalent organic cation, B site is the divalent metal cation, and X is the halide anion. This is where the name “organic-inorganic hybrid perovskite” is coined from – the fact that there exists both organic cations and inorganic cations coordinating with halide anions. The material structure is unique in that the B site cation has an octahedral coordination with the halide anion (X) to form a  $BX_6$  octahedral cage. Within the cage sits the A site cation. Interestingly, there has been studies to show how smaller organic cations, such as methylammonium, can freely rotate within the octahedral cage.<sup>44</sup> This leads to some unique

properties that will be covered in later chapters. These perovskites are in the tetragonal crystal structure (stretched cubic) at room temperature but undergo a phase transition at lower temperatures to a orthorhombic structure.<sup>45</sup>

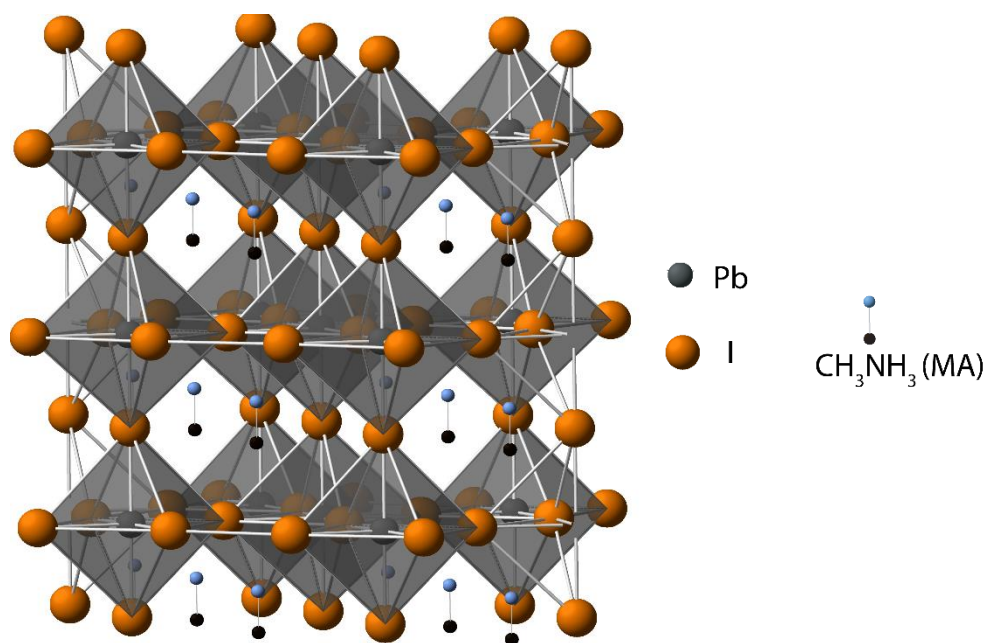


Figure 1.2 Generalized cubic crystal structure for  $ABX_3$  perovskites.

The traditional standard for perovskite solar cells is methylammonium lead iodide ( $CH_3NH_3PbI_3$  or  $MAPbI_3$ ), which is easily prepared from a 3:1 molar ratio of methylammonium iodide and lead iodide. Researchers have explored a wide variety of compositions and substitutions of anions or cations (e.g.,  $CH_3NH_3^+$ ,  $HC(NH_2)_2^+$ ,  $C_6H_5C_2H_4NH_3^+$ ).<sup>16, 46-51</sup> It has been shown that the bandgap of this material can easily be tuned by adjusting the ratio between halide anions ( $Br^-$ ,  $Cl^-$ , or  $I^-$ ). For example, Hoke et al. demonstrated that by increasing the ratio between  $Br^-$  and  $I^-$  anions, the bandgap of the material can shift to a higher energy; shorter wavelength.<sup>46</sup> This type of perovskite is referred to as a mixed-halide lead perovskite. In addition to various combinations of compositions, there is also a wide variety of morphologies that this material can

exist in, such as thin films (wide range of grain sizes), single crystal nanoplates, and nanowires.<sup>37, 52-56</sup> The vast combinations of structure and material composition (i.e. tunability) lead to many interesting and exciting photophysical properties within the realm of semiconductor materials, which will be elaborated upon later in this dissertation.

Photovoltaic efficiency is partly governed by how well the material absorbs the solar spectrum. The solar spectrum extends from the ultraviolet to the mid-infrared (~250 – 2500 nm), with its most intense spectral irradiance in the visible wavelength range (~400 – 750 nm). Therefore, an ideal material for photovoltaic applications should be able to absorb in the visible wavelength range, with a bandgap near the most intense spectral irradiance. Perovskites are quite remarkable in that they absorb the light spanning across the whole visible range, with a bandgap near 750 nm, which is suitable for solar spectrum absorption. Another attractive feature of perovskites as the active layer in the photovoltaic device is the tunability of the bandgap. This tunability is a highly desired attribute for these photovoltaic active layers as well as for light emitting diode (LED) applications, since the shift in bandgap will be shifting the emission peak from the material. The emissive properties of metal halide perovskites have been widely studied for LED applications, lasing, and other optoelectronic devices.<sup>57-62</sup> Photoluminescence for lasing in perovskites has been shown to be a result of bimolecular radiative recombination on the time scale of 10s – 100s of ns.<sup>63</sup> Alternatively, the inorganic based perovskites such as CsPbX<sub>3</sub>, have been shown to be highly efficient LEDs.<sup>60</sup> With tunable emission, high quantum efficiency, and ease of fabrication, perovskites are an ideal material to exploit its emissive properties. Ultimately, we study the transport properties and carrier dynamics associated with these optoelectronic applications.

### 1.4.3 Photophysical Processes

#### 1.4.3.1 Existence of Free Carriers

Photogenerated carriers such as the previously mentioned, Wannier-Mott and Frenkel excitons, are electron-hole pairs that are bound together by a Coulombic interaction. The extent of the exciton binding energy is partly dependent upon the dielectric constant of the material, which results in having high exciton binding energies (0.1 – 0.4 eV) in low dielectric materials such as organic semiconductors (e.g. tetracene and pentacene).<sup>22</sup> Excitons more weakly bound together (hundreds of meV) exist in inorganic 2-dimensional (2D) semiconductors such as MoS<sub>2</sub> and WS<sub>2</sub>.<sup>64</sup> Diffusion lengths of tightly bound electron-hole pairs, found in organic semiconductors, are typically on the order of 10s of nm. Energy is required to separate the charges before charge collection can occur within a solar cell, therefore a material with a very low exciton binding energy would be desirable.

Lead halide perovskites are notorious for having extremely low exciton binding energies. These values are difficult to measure directly but there have been a few techniques that have been used such as, optical absorption, temperature dependent photoluminescence, and magneto-absorption.<sup>65-68</sup> There is a range of exciton binding energies reported for MAPbI<sub>3</sub>, spanning from as low as 5 meV to 19 meV.<sup>67, 68</sup> The higher exciton binding energies reported are from low temperature measurements, due to the previously mentioned crystal structure transition which causes the carriers to be more tightly bound in the orthorhombic phase.<sup>69</sup> The extremely low exciton binding energy at room temperature is particularly useful for photovoltaic devices in which charge separation plays a crucial step before the charge collection. When binding energies are this low, the photogenerated carriers exist as free carriers since thermal energy ( $k_bT$ ) at room temperature is higher than the binding energy ( $\sim 25$  meV), resulting in a fast, thermally activated exciton dissociation.<sup>70</sup> Definitionally, free carriers represent the lowest electronic excited state

that can freely propagate throughout the lattice of the material without the transfer of electric charge.<sup>71,72</sup> After photoexcitation, excitons will already have dissociated and the free carriers may undergo different recombination pathways which is of particular interest due to its detrimental effects in a solar cell or beneficial effects in LEDs or lasers.

#### 1.4.3.2 Recombination Mechanisms

Aside from ultrafast pump-probe microscopy, we are also interested in time-resolved spectroscopy. Many important parameters can be elucidated from time-resolved spectroscopy as a kinetic description of the photogenerated process. In a general scenario, rapid dephasing and cooling of photogenerated carriers occurs after initial excitation. There is also an additional loss of energy from the nonequilibrium state over a longer timescale, which occurs radiatively (emission of light) or non-radiatively (e.g. vibrational, heat, carrier-carrier interactions). By altering the excitation intensity and photon energy, one can appropriately model/fit the time-resolved dynamics and monitor the steady-state PL intensity, which can provide physical insight into the photophysical processes associated with the return to the ground state. Understanding the predominate pathways associated with energy loss at various carrier densities is crucial to optimizing optoelectronic devices (operating conditions and device configurations), specifically photovoltaics, LEDs, and lasers.<sup>70</sup>

Defects and microscale inhomogeneities act as pathways for non-radiative loss, which is detrimental to photovoltaic devices and light emission devices. Techniques such as steady state PL spectroscopy, time-resolved PL spectroscopy, transient absorption spectroscopy, and confocal PL imaging have been employed to elucidate the carrier dynamics in semiconductor materials.<sup>15, 17, 18, 46, 64, 73-78</sup> Typically there are three distinct classes of possible generation and recombination pathways – trap mediated, band edge, and excitonic. For MAPbI<sub>3</sub> we will focus on the trap

mediated and band edge energy loss pathways and will assume hole trapping mechanisms are negligible. Figure 1.3 represents a schematic that illustrates the possible generation and recombination pathways for this material. Pathway 1 (blue) is representative of direct population of a sub-bandgap state in the trap mediated regime. This can exist via photoexcitation and have direct population into the semiconductor's Urbach Tail.<sup>43, 79, 80</sup> Pathway 2 (red) represents the trapped carriers recombining radiatively, whereas pathway 3b (green) is the nonradiative recombination, such as a phonon-assisted process. The band edge carriers can become initially trapped through a common population pathway such as nonradiative localization (3a – green), before ultimately succumbing to nonradiative recombination (3b – green). Aside from the trap mediated regime, there exists a band edge regime. To populate the band edge, the material must be excited through a direct resonant excitation (i.e. pump at the energy of the bandgap), depicted by pathway 4 – purple. Bimolecular recombination, shown by pathway 5 – orange, is a radiative recombination process (such as PL). Alternatively, a three-carrier nonradiative Auger process can occur (pathway 6 – black). The carrier generation and annihilation processes can be modeled together using the following equation (Eq. 1.2). In this equation,  $n$  is the total carrier concentration as a function of time and  $G$  is the carrier generation term which relates to the excitation intensity by  $G = \alpha I$ . The generation term is usually negligible for this work since the ultrafast (fs) excitation pulses are used. The single component term is associated with trap mediated (sub-band gap states) recombination or geminate recombination, while the bimolecular term is associated with nongeminate recombination (exciton-exciton annihilation). The last term is representative of a nonradiative three-carrier interaction, such as Auger recombination (depicted by pathway 6 – black).

$$\frac{dn}{dt} = G - k_1 n - k_2 n^2 - k_3 n^3 \quad (1.2)$$

In comparison to GaAs, MAPbI<sub>3</sub> has a comparable bandgap and near-edge absorption coefficient, yet Auger rates are enhanced nearly two orders of magnitude.<sup>81, 82</sup> Yang et al. state that this strange behavior could arise from carrier localization or enhanced Coulombic interactions between carriers.<sup>82</sup> There lacks evidence for carrier localization to be the cause of such high Auger rates. Alternatively, enhanced Coulombic interactions has been shown to increase the probability of spatial overlap between carriers and enhance Auger recombination in semiconductors.<sup>43, 82, 83</sup> Since bimolecular and trimolecular recombination rate constants are primarily intrinsic properties of a given semiconductor, it implies that these constants cannot be manipulated, without altering the material itself.

Contrarily, monomolecular energy loss processes associated with trap assisted recombination are extrinsic properties, which means that materials processing can focus on improving this aspect of the material in the fabrication process. The fundamental understanding of these extrinsic and intrinsic recombination processes leads to future improvement of the performance in optoelectronic devices. The time-resolved PL dynamics and transient absorption dynamics in this work elucidate these recombination mechanisms in attempt to shed light on the underlying photo-physics associated with this material's exceptional device performance.

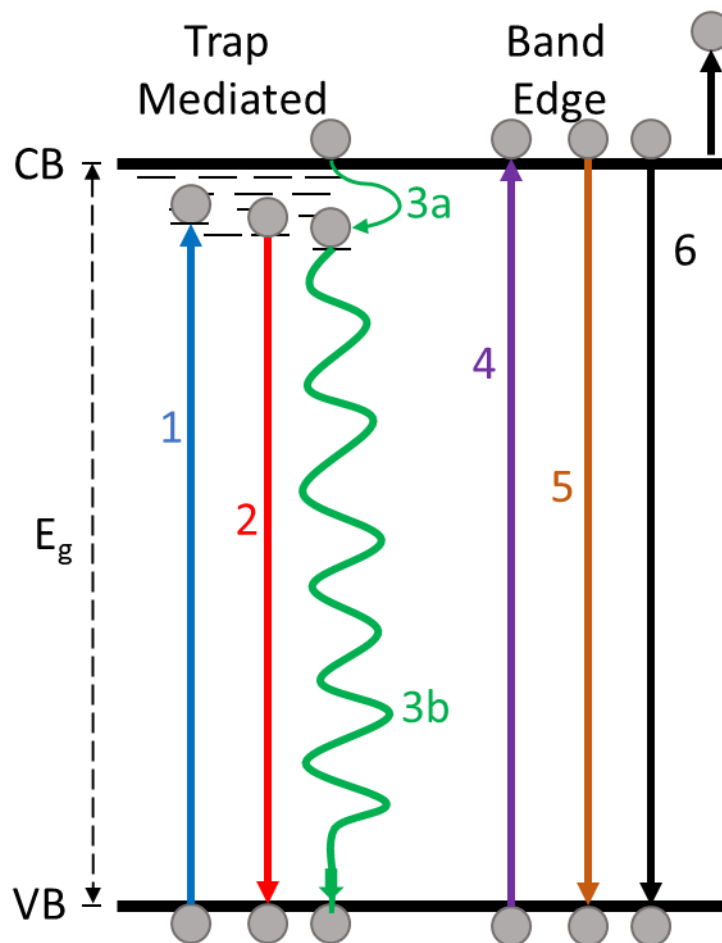


Figure 1.3 Schematic representation of the energy generation and loss pathways in MAPbI<sub>3</sub> semiconductor material.

## 1.5 Conclusion

In conclusion, we have utilized ultrafast pump-probe microscopy and spectroscopy to investigate how photogenerated charges propagate throughout semiconductor materials for photovoltaic applications. We have studied factors that impact carrier diffusion length such as grain boundaries, nonequilibrium carriers, and recombination mechanisms to gain a fundamental understanding on the photophysical properties of the material in efforts to potentially provide

insight into devices with higher power conversion efficiencies. Ultimately, the nature of photogenerated carriers within the perovskite absorber material is heavily probed on a fundamental level in this dissertation.

This dissertation is divided into several chapters, each containing a detailed introduction to their respective projects. The organization of our work is as follows: we will first discuss the background on experimental methods used in this work, in Chapter 2. The remaining chapters display the main results from each of the projects. In Chapter 3, we unravel a widely debated question on the role of grain boundaries in lead halide perovskite thin films. We utilized TAM to directly clarify the dispute into whether grain boundaries are detrimental to carrier transport or not, which ultimately impacts solar cell performance. Chapter 4 summarizes our study on the direct visualization of hot carrier transport in perovskites by implementing TAM. In Chapter 5, we examine the acceleration of carrier transport via a hot phonon bottleneck in perovskite films. Here, we see that extending the cooling time of nonequilibrium carriers leads to an acceleration in carrier transport. Lastly, we summarize our collaborative efforts which explore the effects of incorporating alkali metals on the homogenization of carrier dynamics in alloyed perovskite materials and discusses the exciting new class of hybrid perovskite quantum wells. These two-dimensional materials exhibit efficient energy transfer between the organic and inorganic components of the material and shed light onto the exciting potential that these new materials have.

## CHAPTER 2. MATERIAL CHARACTERIZATION METHODS

### 2.1 Steady-State Absorption and Reflectance

Ensemble absorption measurements were conducted on an Agilent Cary 6000i UV-Vis-NIR spectrophotometer. This instrument was used in the Purdue Chemistry Department Research Instrumentation Center.

Differential reflection spectra were obtained by using a home-built micro-reflection setup (Figure 2.1). In summary, the white light from a stabilized tungsten-halogen light source (Thorlabs) was spatially filtered by focused on a pinhole with 10  $\mu\text{m}$  diameter, then collimating the light. After, the collimated white light is focused onto the sample with a 50 $\times$  (NA = 0.95) objective. The beam size of white light is about 3  $\mu\text{m}$ . The reflected light was collected with the same objective, then dispersed with a monochromator (Andor Technology – Shamrock) and ultimately detected by a TE cooled charge-coupled device (CCD) camera (Andor Technology – Newton). The differential reflectance is defined as:

$$\delta R(\lambda) = \frac{R_{sample} - R_{substrate}}{R_{substrate}} \quad (2.1)$$

where  $R_{sample}$  is the reflectance intensity of sample with substrate and  $R_{substrate}$  is the reflectance intensity of the bare substrate. For thin films on a transparent substrate, the differential reflection is directly related to the absorption by the following equation<sup>84</sup>:

$$\delta R(\lambda) = \frac{4}{n_{sub}^2 - 1} A(\lambda) \quad (2.2)$$

where  $n_{sub}$  is the refractive index of substrate and  $A(\lambda)$  is the absorption coefficient.

## 2.2 Steady-State and Time-Resolved Photoluminescence

Steady-state photoluminescence and time-resolved photoluminescence measurements were performed by employing a home-built confocal micro-photoluminescence setup, schematic shown in Figure 2.1. A picosecond pulsed diode laser (Pico-Quant, LDH-P-C-450B) with an excitation wavelength of 447 nm (FWHM = 50 ps) and a repetition rate of 40 MHz was used to excite the sample for measurements, which was focused by a 50 $\times$  (NA = 0.95) objective. The beam size in PL measurements is <1  $\mu$ m. The PL emission was collected with the same objective, dispersed with a monochromator (Andor Technology – Shamrock) and detected by a TE cooled charge coupled device (CCD) camera (Andor Technology – Newton). For time resolved PL measurements, the repetition rate of the laser was 2.5 MHz. The dynamics of PL were measured using a single photon avalanche diode (Pico-Quant, PDM series) and a single photon counting module (Pico-Quant). The time resolution of this setup is  $\sim$ 100 ps.

Steady-state PL images were taken one of two ways: On the same home-built confocal PL microscope, with the addition of 2D galvanometer scanning mirrors or on a commercial fluorescence microscope (Olympus BX-51 Optical Microscope) in the Purdue Chemistry Department Research Instrumentation Center.

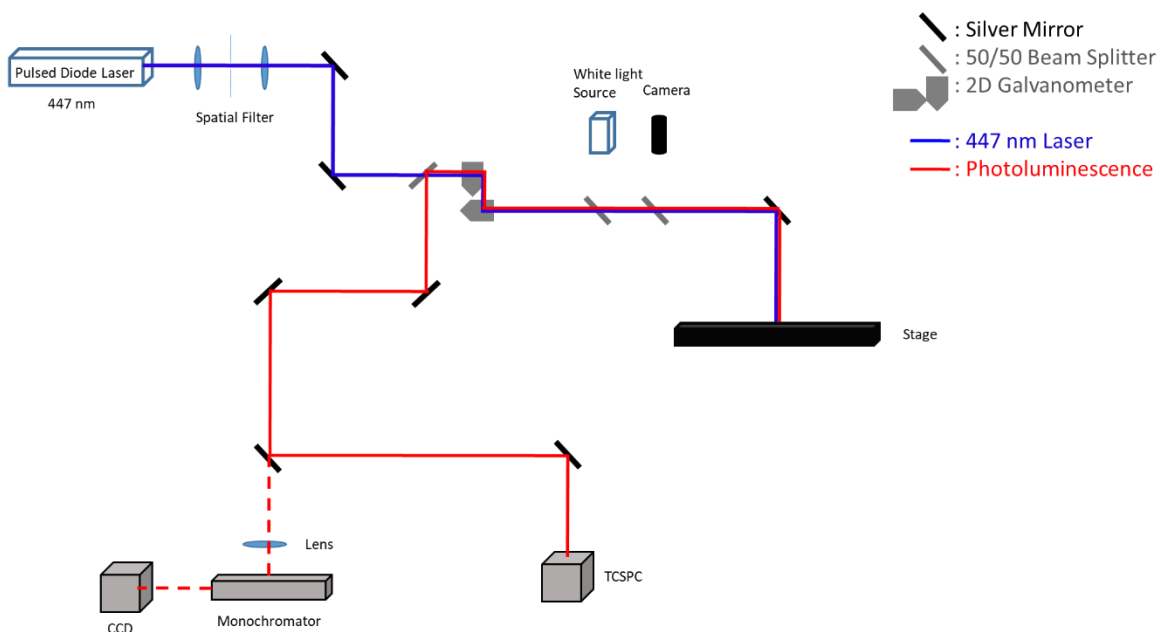


Figure 2.1 Schematic of home-built confocal PL microscope.

### 2.3 Surface Characterization

To characterize the surfaces of any materials needed for study, scanning electron microscopy (SEM) and atomic force microscopy (AFM) may be used. The SEM we used was from Purdue University Birck Nanotechnology Center. The instrument is the FEI Nova 200 NanoLab dual beam SEM/FIB (focused ion beam). SEM provided insight into high definition surface structure with high resolution (<100 nm). For AFM measurements, we used the Purdue Chemistry Department Research Instrumentation Center's Veeco Dimension 3100 AFM.

## 2.4 Transient Absorption Spectroscopy

Transient absorption spectra were measured by a femtosecond pump–probe system with a home-built transient absorption spectrometer. The schematic representation is shown in Figure 2.2. Laser pulses at 1030 nm with 250 fs duration were generated by a 400 kHz amplified Yb:KGW laser system (PHAROS, Light Conversion Ltd.).

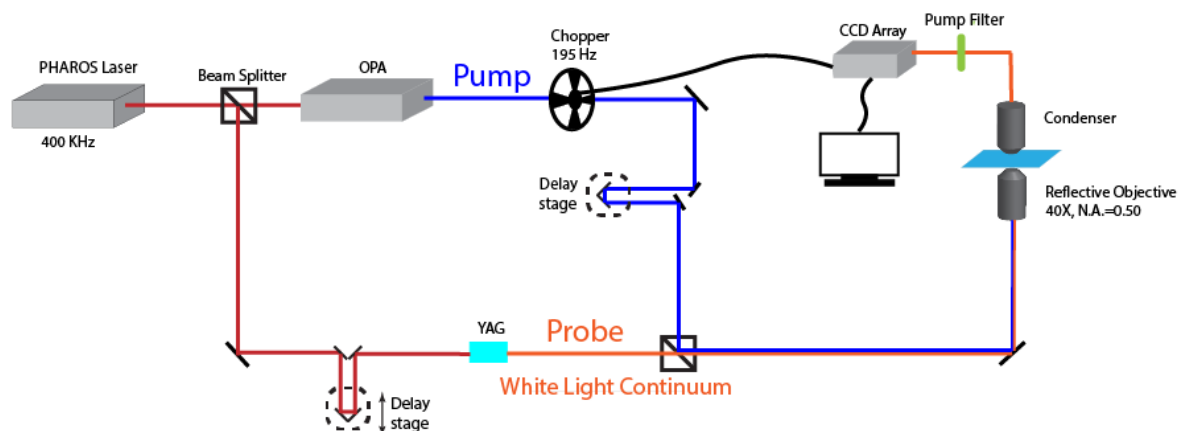


Figure 2.2 Schematic representation of transient absorption spectroscopy setup. OPA: optical parametric amplifier; YAG: Yttrium aluminum garnet; CCD: charge-coupled device.

The probe beam was a white light continuum beam spanning the 450-950 nm spectral region, created by focusing 5% of the 1030 nm fundamental output onto a YAG crystal (4.0 mm thick). The rest of the output pumps an optical parametric amplifier (OPA, TOPAS-Twins, Light Conversion Ltd.) to generate pump pulses with tunable photon energies for the transient absorption experiments. Ensemble measurements for thin films have the pump beam focused down with a plano-convex lens and the probe beam focused down with a concave mirror. Micrometer sized samples need the beams to be colinear and pass through a reflective objective (Thorlabs 40 $\times$ , NA = 0.5). The probe light after the sample is collected by a lens and focused onto a CCD spectrometer (Exemplar LS, B&W Tek). The time delay between the pump and probe beam is adjusted by a

delay stage. The delay stage is a linear stepper motor stage from Newport (ILS100PP) and this allows for transient absorption dynamics scans, by delaying the probe beam relative to the pump beam.

#### 2.4.1 Global Analysis

Global analysis was carried out by first performing singular value decomposition to extract out the minimal number of kinetic component required to describe the system within instrument signal-to-noise ratio. This was followed by using a multiple exponential function with the same number of components to convolve with the instrument response (a Gaussian function with pulse width and chirped at different wavelengths) and a nonlinear least square minimization was performed to extract out the optimized rate constants as well as the decay associated spectra (DAS). Glotaran package was used for the relevant analysis throughout this work.<sup>85</sup>

#### 2.5 Transient Absorption Microscopy

The representative schematic of the home-built TAM instrumentation that has been employed in our work is shown in Figure 2.3. The laser system is a high repetition rate ultrafast amplifier system (Light Conversion Pharos) with repetition rate tunable from 1- 400 KHz. The amplifier pumps two independent optical parametric amplifiers (OPAs, Light Conversion) that provide ~ 200 fs pulses tunable from 315 -2000 nm. The tunability of both the pump and probe wavelengths allows selective excitation and detection of singlet and triplet exciton transitions. For carrier transport measurements, the probe beam is passed through a 2D galvanometer scanning mirror to control the relative position between the pump and probe beams with high precision (path 1 in Figure 2.3). Path 2 in Figure 2.3 depicts the beam path for transient absorption morphology images. By scanning the pump and probe beams together with the 2D galvanometer mirrors, we

can map the transient signal spatially. The pump and the probe beams are combined to be colinear in front the entrance to a home-built inverted optical microscope and then focused onto the sample with a high numerical aperture (NA) oil immersion microscope objective (NA= 1.49). The time delay between the pump and probe beams is controlled by an optical delay stage by extending the beam path of the probe beam relative to the pump. The optical delay stage is capable of scanning pump probe delay up from 6 fs to 8 ns. Pump-induced changes in the probe transmission ( $\Delta T$ ) is measured by modulating the pump beam with an acousto-optic modulator (AOM) and monitoring the output of the avalanche photodiode (APD) with a lock-in amplifier. This TAM instrumentation is highly sensitive, with detectable  $\Delta T/T$  on the order of  $10^{-7}$ . The spot size of the pump and probe beams at the sample is determined by the associated wavelengths and the NA of the microscope objective employed  $\left(\frac{\lambda}{2NA}\right)$  and will be determined experimentally using absorption image of a nanowire that much smaller than the diffraction limit.

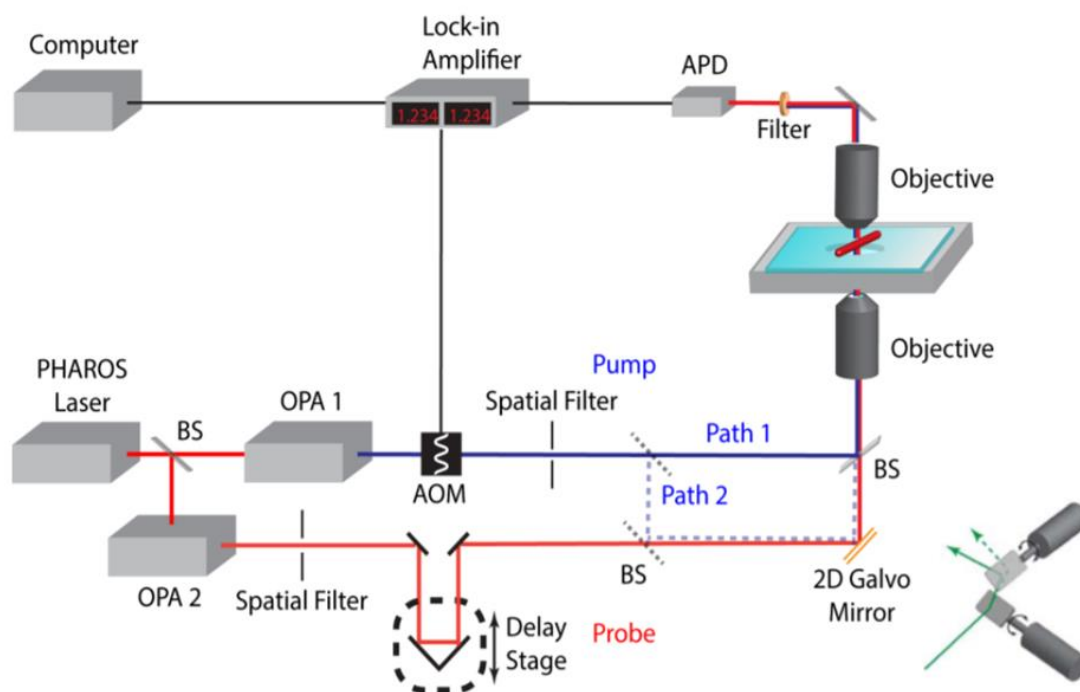


Figure 2.3 Schematic of home-built transient absorption microscopy set up. BS = beam splitter, AOM = acoustic optical modulator, OPA = optical parametric amplifier, APD = avalanche photodiode.

### 2.5.1 Carrier Transport

To quantify transport, carrier population as a function of space and time can be described by a differential equation that includes both the transport out of the initial volume and population decay, which is given by,

$$\frac{\partial n(x,y,t)}{\partial t} = D \left[ \frac{\partial^2 n(x,y,t)}{\partial x^2} + \frac{\partial^2 n(x,y,t)}{\partial y^2} \right] - \frac{n(x,y,t)}{\tau} \quad (2.3)$$

where  $n(x, y, t)$  is the carrier population at time  $t$ ,  $D$  is the diffusion constant, and  $\tau$  is the carrier lifetime. The initial population  $n(x, y, 0)$  follows Gaussian distribution as created by a Gaussian pump beam at position  $(x_0, y_0)$  and is given by:

$$n(x, y, 0) = N \exp \left[ -\frac{(x-x_0)^2}{2\sigma_{x,0}^2} - \frac{(y-y_0)^2}{2\sigma_{y,0}^2} \right] \quad (2.4)$$

The solution to Equation (1) indicates that carrier density at any later delay time ( $t$ ) is also Gaussian and can be described as:

$$n(x, y, t) = N \exp \left[ -\frac{(x-x_0)^2}{2\sigma_{x,t}^2} - \frac{(y-y_0)^2}{2\sigma_{y,t}^2} \right] \quad (2.5)$$

The diffusion constant  $D$  is then given by:

$$D_{x(y)} = \frac{\sigma_{x(y),t}^2 - \sigma_{x(y),0}^2}{2t} \quad (2.6)$$

The transport length,  $L$ , at delay time,  $t$ , is related to the variance of the carrier density profile and the diffusion constant ( $D$ ),

$$L_{x(y)}^2 = \sigma_{x(y),t}^2 - \sigma_{x(y),0}^2 = 2D_{x(y)}t \quad (2.7)$$

### 2.5.2 Spatial Precision Limiting Factors

In the TAM imaging of carrier transport, the precision in determining the carrier propagation distance  $L$  is dictated by the smallest measurable change in the population profiles which is  $\sim 100$  nm. This is not directly determined by the diffraction limit. The measured carrier distribution is convoluted with profiles of pump and probe beams, so that the measured carrier distribution could be written as:

$$\sigma_{(measurement)}^2 = \sigma_{(carrier)}^2 + \sigma_{(pump)}^2 + \sigma_{(probe)}^2 \quad (2.8)$$

The diffusion length of carrier propagation is written as:

$$L^2 = \sigma_{(t)}^2 - \sigma_{(0)}^2 \quad (2.9)$$

Since  $\sigma_{(pump)}^2$  and  $\sigma_{(probe)}^2$  remain the same during pump-probe delay, the diffusion length is only determined by the change of carrier density profiles. Here we performed a sensitivity analysis by differentiating equation 2.9 to obtain the error of measured diffusion length written as:

$$\Delta L = \sqrt{\frac{\sigma_{(t)}^2}{\sigma_{(t)}^2 - \sigma_{(0)}^2} (\Delta\sigma_{(t)}^2)^2 + \frac{\sigma_{(0)}^2}{\sigma_{(t)}^2 - \sigma_{(0)}^2} (\Delta\sigma_{(0)}^2)^2} = \sqrt{\Delta\sigma_{(t)}^2 + \left(\frac{\sigma_{(0)}}{L}\right)^2 (\Delta\sigma_{(0)}^2 - \Delta\sigma_{(t)}^2)} \quad (2.10)$$

From equation 2.10, we can clearly see the error primarily comes from the uncertainty of the Gaussian profiles obtained at different time delays, which is determined by the signal-to-noise ratio of the instrument. A similar discussion on the resolution of such imaging approach can also be found in a prior work by Akselrod et al., where photoluminescence microscopy imaging technique was employed.<sup>21, 86</sup>

### 2.5.3 Noise

There are two main sources of noise contributing to transient absorption imaging: laser fluctuation and electronic noise from the detection system (e.g. detector and lock-in amplifier). Noise due to laser intensity fluctuations can be effectively eliminated by using lock-in detection with kHz modulation where the intensity of the excitation beam (or additional local oscillator) is modulated by an acoustic-optical modulator. Subsequently, a lock-in amplifier referenced to this modulation frequency can sensitively extract the induced signal. The fluctuation of laser intensity (1/f noise) usually occurs at low frequency (< 10 kHz). The pixel dwell time should be significantly longer than the modulation period to allow for reliable demodulation for each pixel. In our experiments, we use a modulation frequency of 100 kHz. The TAM instrumentation described in this dissertation can detect a differential transmission  $\Delta T/T$  of  $10^{-7}$ , which is three orders of magnitude higher sensitivity than conventional TA spectroscopy.<sup>21, 87</sup>

## **CHAPTER 3.     ROLE OF GRAIN BOUNDARIES IN PEROVSKITE THIN FILMS**

### 3.1 Abstract

For optoelectronic devices based on polycrystalline semiconducting thin films, carrier transport across grain boundaries is an important process in defining efficiency. In this work, we employ transient absorption microscopy (TAM) to directly measure carrier transport within and across the boundaries in hybrid organic–inorganic perovskite thin films for solar cell applications with 50 nm spatial precision and 300 fs temporal resolution. By selectively imaging sub-bandgap states, our results show that lateral carrier transport is slowed down by these states at the grain boundaries. However, the long carrier lifetimes allow for efficient transport across the grain boundaries. The carrier diffusion constant is reduced by about a factor of 2 for micron-sized grain samples by the grain boundaries. For grain sizes on the order of  $\sim 200$  nm, carrier transport over multiple grains has been observed within a time window of 5 ns. These observations explain both the shortened photoluminescence lifetimes at the boundaries as well as the seemingly benign nature of the grain boundaries in carrier generation.

### 3.2 Introduction

Carrier transport in semiconductors is a crucial process that defines efficiency for optoelectronic devices, such as solar cells and light emitting diodes. Many of these devices are fabricated from polycrystalline materials; therefore, transport across the grain boundaries is a major challenge in achieving optimal device performance.<sup>88, 89</sup> Semiconducting hybrid organic–inorganic lead halide perovskites, such as  $\text{CH}_3\text{NH}_3\text{PbI}_3$  (MAPbI<sub>3</sub>), have recently attracted significant research interest, motivated largely by the rapid rise in efficiency of solar cells, recently achieving above 22%.<sup>90-96</sup> The high efficiency of perovskite solar cells has been attributed to extraordinarily long carrier lifetimes,<sup>97-102</sup> long-range carrier diffusion,<sup>103-108</sup> and exceptional defect tolerance.<sup>109-111</sup> Since polycrystalline hybrid perovskite thin films employed in the solar cells are commonly grown by low temperature solution processes, the formation of grain boundaries is inevitable.<sup>112</sup> The structural disorders at the boundaries could form defect states and potential barriers, leading to slow carrier transport.<sup>113</sup>

A detrimental mechanism of energy loss that results in a decrease in power conversion efficiency is limited carrier mobility. In polycrystalline perovskite, thin films, the morphology is commonly seen to be grain-like due to highly desired solution processing. These grains can typically range from 0.1  $\mu\text{m}$  all the way up to 10  $\mu\text{m}$ . When the morphology of the material has grain structures, the grain boundaries can serve as a trap site for the carriers. Once trapped, the carriers will likely recombine, thus losing potential carriers that could have been harvested to increase the device performance. A comprehensive understanding of charge carrier dynamics and charge transport in relation to film morphology is required to design optimal devices based on these materials.

The impact of grain boundaries on carrier transport in hybrid perovskites has been indirectly demonstrated by the fact that the carrier diffusion lengths measured from polycrystalline thin films are significantly shorter than those of single crystals (a few  $\mu\text{m}$  vs.  $> 100 \mu\text{m}$ ).<sup>103-108</sup> Recent theoretical studies have suggested that grain boundaries create shallow sub-bandgap states.<sup>113, 114</sup> Experimentally, grain boundaries are difficult to independently control and measure as it could depend on fabrication methods. More recently, scanning probe<sup>115-117</sup> and optical microscopy<sup>17, 118-123</sup> approaches have been employed to map carrier generation and dynamics at the grain boundaries. Despite these recent studies, the role of grain boundaries in hybrid perovskite thin films is currently under debate. Some have shown that the photoluminescence (PL) intensity of grain boundaries are overall weaker, exhibiting faster PL decays.<sup>118</sup> In contrast, others have reported that the PL lifetimes are not shorter compared to grain surfaces or grain interiors, which suggests that grain boundaries do not dominate non-radiative recombination in  $\text{MAPbI}_3$  films.<sup>77, 124, 125</sup> Scanning probe measurements also suggest that for encapsulated thin films with micron-sized grains, grain boundaries are relatively benign to carrier generation and transport.<sup>115, 126</sup> In addition, some studies have suggested that the grain boundaries are not detrimental and could even be beneficial for device performance.<sup>127, 128</sup>

To reconcile these discrepancies regarding the role of grain boundaries in the literature, direct measurements to quantify morphology dependent carrier transport in both spatial and temporal domains are highly desirable. While scanning probe approaches can image conductivity at the grain boundaries, these measurements represent a time-averaged picture and lack the necessary temporal resolution to elucidate the underlying mechanisms. In this work, we utilized transient absorption microscopy (TAM) to directly visualize carrier migration across grain boundaries with 50 nm spatial precision and 300 fs temporal resolution. Carrier diffusion constants

within and across the boundaries are directly measured. Our results show that while carrier diffusion constant is reduced by the grain boundaries due to the sub-bandgap states, the long carrier lifetime allows transport across the grain boundaries leading to overall little detrimental effects in device performance.

### 3.3 Material Preparation

The perovskite thin films were prepared from modified non-stoichiometric precursor.<sup>129</sup> For the large grain film, methylammonium iodide (MAI), lead iodide ( $\text{PbI}_2$ ), and methylammonium chloride (MACl) ( $\text{MAI}/\text{PbI}_2/\text{MACl}=1/1/0.2$ ) were dissolved in N-Methyl-2-pyrrolidone (NMP) and gamma-Butyrolactone (GBL) ( $\text{NMP}/\text{GBL}=7/3$  volume ratio) to form 50 wt% precursor solutions. For the small grain film, 50 wt% stoichiometric precursors ( $\text{MAI}/\text{PbI}_2=1/1$ ) was prepared. Both films were crystalized through an antisolvent extraction method. Cover slip substrate with dispersed precursor was span at 4500 rpm for 25 s, and promptly transferred into abundant diethyl ether (DEE) solution for 1 min to finish the crystallization process. For the large grain film, substrate was further thermally annealed at 150 °C with a petri-dish covered in air for 15 min. For the small grain film, substrate was annealed at 100°C for 10 min.

### 3.4 Material Characterization

The perovskite thin films were characterized by X-ray diffraction using a X-ray diffractometer (Rigaku D/Max 2200) with Cu  $K_{\alpha}$  radiation. The morphologies of the films were examined by field emission scanning electron microscopy (FE- SEM, JEOL JSM- 7000F). The representative XRD patterns for film 1 (red) and film 2 (black) are shown in Figure 3.1.

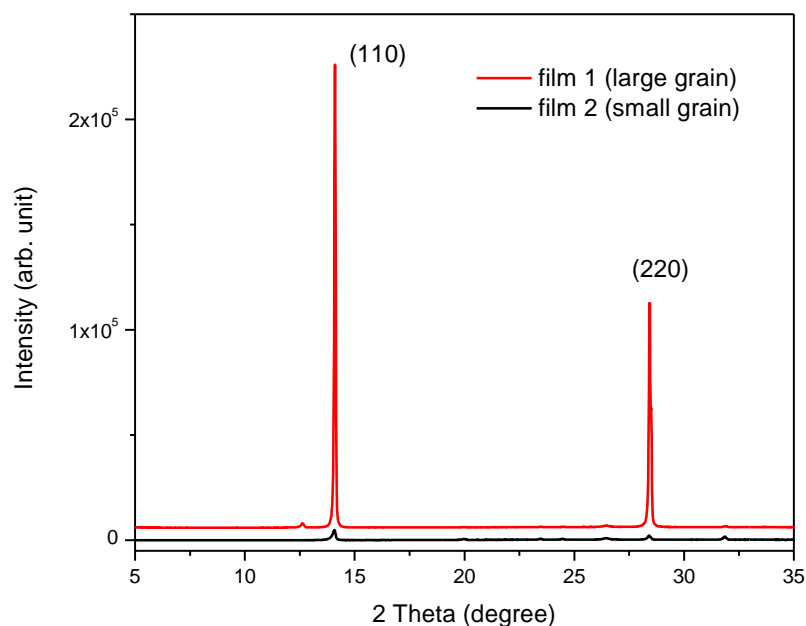


Figure 3.1 XRD patterns for film 1 (red) and film 2 (black).

Photoluminescence microscopy was utilized to give a representation of the grain sizes of film 1 and film 2. PL microscopy images were taken on a commercial fluorescence microscope (Olympus BX-51 Optical Microscope). The images are shown in Figure 3.2 for the large grain sample (Film 1) and the small grain sample (Film 2).

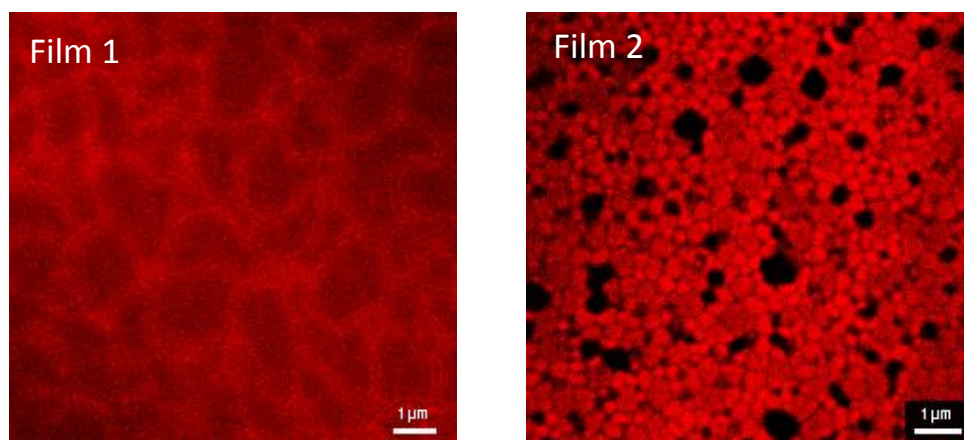


Figure 3.2 Photoluminescent microscopy images for film 1 and film 2 showing average grain sizes of  $>1 \mu\text{m}$  and  $<500 \text{ nm}$  for films 1 and 2, respectively.

### 3.5 Results and Discussion

#### 3.5.1 Band-Edge vs. Sub-Band Gap Transient Absorption Imaging

For the experiments presented here, we investigated polycrystalline  $\text{MAPbI}_3$  thin films with different averaged grain sizes. Film 1 has a larger average grain size ( $>1 \mu\text{m}$ ) than film 2 ( $\sim 200 \text{ nm}$ ), as shown by the scanning electron microscopy (SEM, Figure 3.3 a and b) and the PL microscopy images depicted in Figure 3.2. The x-ray diffraction patterns shown in Figure 3.1, confirms that both films are polycrystalline.<sup>129</sup> The thickness for both films is estimated to be  $\sim 500 \text{ nm}$  using the absorbance at  $650 \text{ nm}$  and an extinction coefficient of  $3 \times 10^6 \text{ m}^{-1}$ .<sup>130</sup> It has been demonstrated that the true grain size is equivalent to the apparent grain size for these thin films using piezoresponse force microscopy.<sup>126</sup> Solar cells made from thin films fabricated using the same device fabrication procedure have demonstrated power conversion efficiencies of about 18 and 15% under standard Air Mass 1.5 illumination for films 1 and 2, respectively.<sup>129</sup> The absorption spectra of the two films are shown in Figure 3.3 c. A low-energy absorption tail is observed for film 2, likely due to scattering from the grain boundaries. The  $\tau_{\text{auc}}$  analysis of the absorption spectra shows that film 1 has a slightly smaller bandgap than film 2 due to larger grain

size (shown in Figure 3.4), which is consistent with a previous report.<sup>131</sup> Film 2 exhibits a shorter PL lifetime of  $38 \pm 1$  ns than that of  $87 \pm 1$  ns for film 1 (Figure 3.3 d), indicating faster carrier recombination, agreeing with smaller grain size.<sup>131</sup>

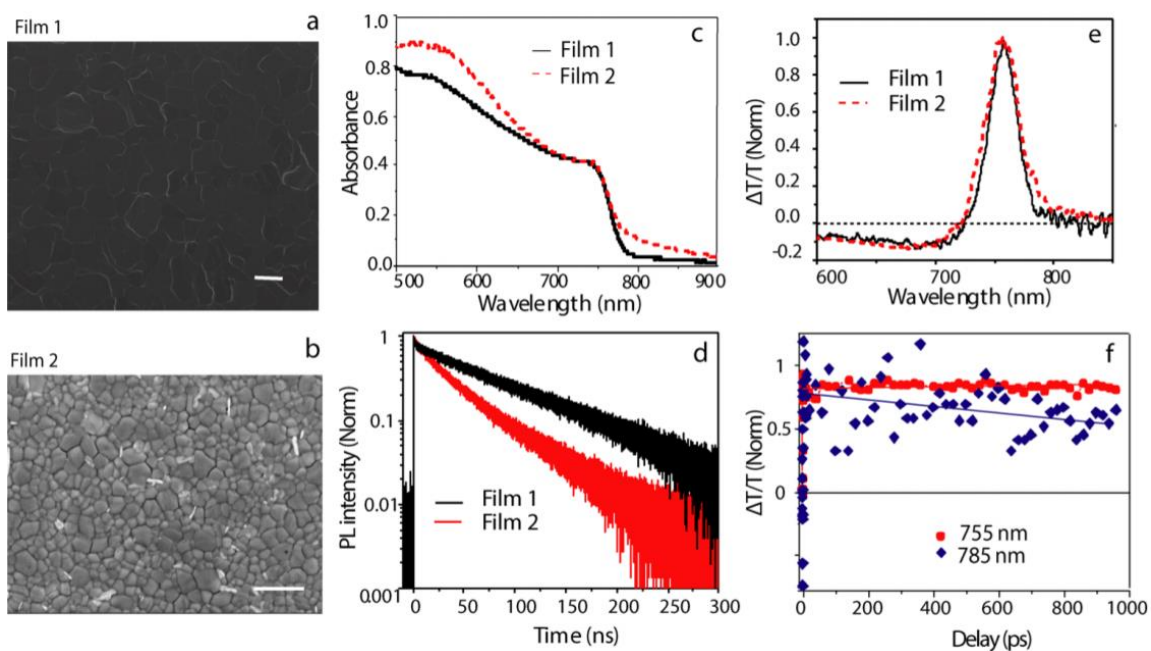


Figure 3.3 SEM images for perovskite thin films with grain sizes  $> 1 \mu\text{m}$  (film 1, a) and  $\sim 200$  nm (film 2, b). Scale bars represent  $1 \mu\text{m}$ . (c) Absorption spectra for film 1 and film 2. (d) PL lifetime measurements for film 1 and film 2. Excitation wavelength  $447 \text{ nm}$ ; fluence  $0.5 \mu\text{J}/\text{cm}^2$ . (e) Ensemble transient absorption spectra at  $10 \text{ ps}$  time delays ( $630 \text{ nm}$  pump) for film 1 and film 2. (f) Carrier dynamics pumped at  $630 \text{ nm}$ , probed at  $755 \text{ nm}$  and probed at  $785 \text{ nm}$  for film 1. The pump fluence is  $1 \mu\text{J}/\text{cm}^2$ .

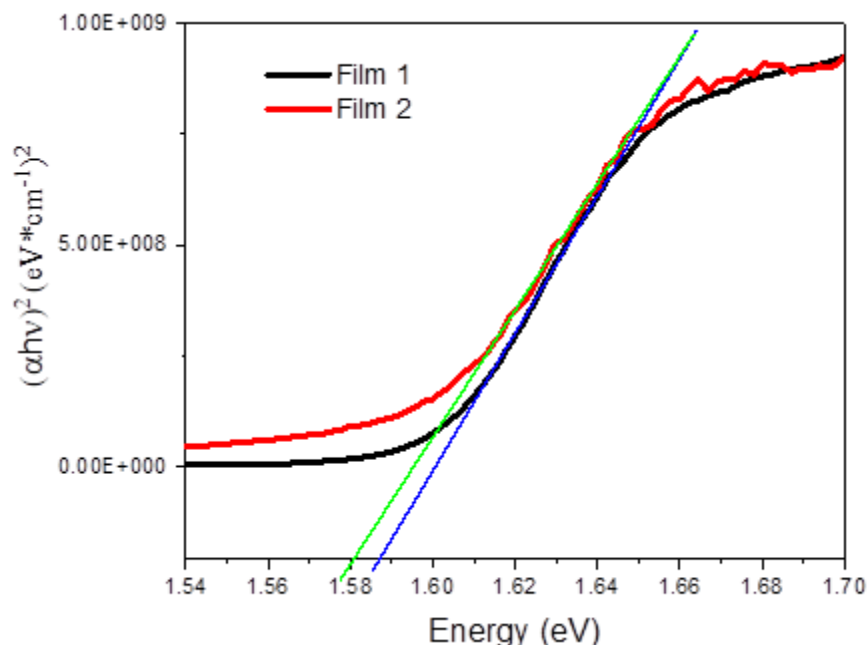


Figure 3.4 Tauc plot for Film 1 (black) and Film 2 (red). Blue and green lines are tangent lines that extrapolate to the energy corresponding to the bandgap. The tauc analysis was done by determining the absorption coefficient ( $\alpha$ ) of the material from the following equation:  $\alpha = \frac{(2.303 \cdot A)}{z}$ , where  $z$  is the thickness of the film (537 nm). Lastly,  $(\alpha * h\nu)^2$  will be the y-axis in the tauc plot, where  $h\nu$  is the photon energy. Film 1 has a band gap of 1.588 eV (781 nm) and Film 2 has a band gap of 1.580 eV (785 nm).

Ensemble transient absorption spectra show a photoinduced bleach band centered at  $\sim 755$  nm corresponding to the bandgap absorption with a small tail below the bandgap (Figure 3.3 e). Film 2 shows a broader photoinduced bleach band and with more significant contribution from below the bandgap. The broader transient absorption feature could be explained by more disorder due to the smaller grain size in film 2, and the sub-bandgap transient absorption can be attributed to defect/ trap states that could be more prevalent at the grain boundaries.<sup>113</sup> Carrier dynamics probed at 785 nm show faster recombination than those probed at 755 nm, consistent with recombination due to defect or trap states (Figure 3.3 f).

To visualize the spatial distribution of the sub-bandgap states as well as to address how they influence charge transport, we perform morphological and carrier transport TAM imaging.

All TAM measurements are performed in transmission mode; therefore, pump-induced change of the probe transmission  $\Delta T$  is integrated over the sample depth direction and reflects the sum of carrier population over the entire film thickness instead of just the surfaces. A schematic of the TAM instrumentation and a detailed description of the set up can be found in Chapter 2.

Carrier density plays an important role in carrier dynamics because higher-order carrier recombination processes can dominate at high carrier density. To ensure that such higher-order processes do not complicate the TAM experiments, we have carried out pump intensity-dependent measurements for film 1 (left) and film 2 (right), shown in Figure 3.5. All the TAM measurements presented here are performed at a pump fluence of  $1 \mu\text{J}/\text{cm}^2$ , well below the threshold for higher-order effects. A laser repetition rate of 400 kHz is employed for TAM imaging. We have measured dynamics at a repetition rate of 200 kHz and compared them to those measured at 400 kHz in Figure 3.6. The dynamics are identical at these two repetition rates, indicating that long-lived trap states and pulse-to-pulse pileup are negligible.

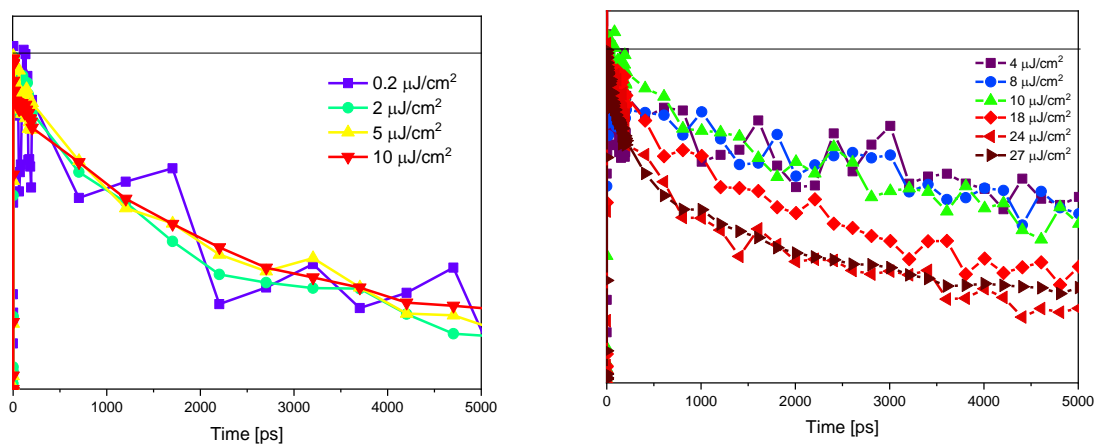


Figure 3.5 Ground state bleach dynamics at various pump fluence for film 1 (left) and film 2 (right). Based upon the power dependence for film 2, any fluence less than  $24 \mu\text{J}/\text{cm}^2$  will be suitable for the measurements. All powers measured for film 1 are acceptable for diffusion measurements.  $1 \mu\text{J}/\text{cm}^2$  was chosen for subsequent measurements.

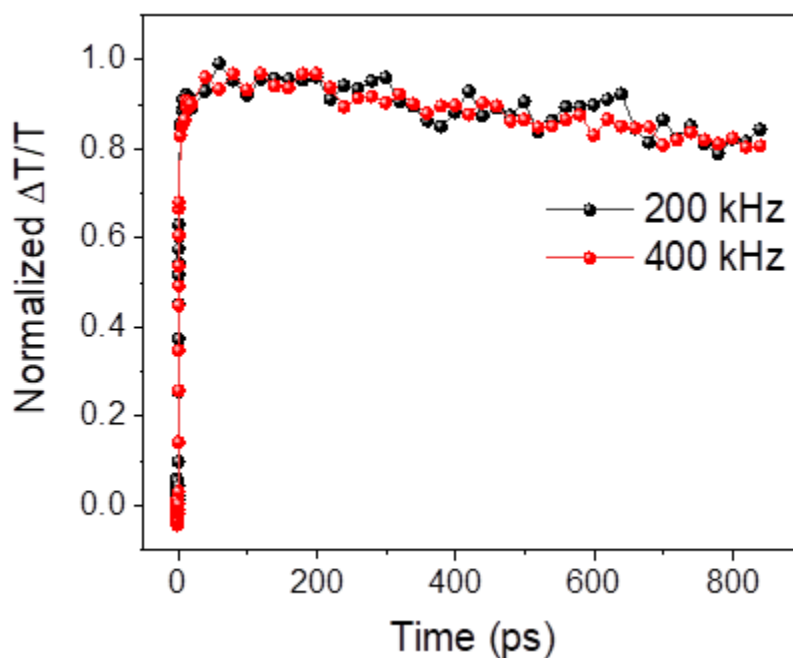


Figure 3.6 Ground state bleach dynamics at different laser repetition rates (200 kHz – black, 400 kHz – red) for small grain sample. The resulting time between pulses are  $2.5 \mu\text{s}$  (red) and  $5.0 \mu\text{s}$  (black). The pump wavelength is 400 nm with a fluence of  $\sim 7 \mu\text{J}/\text{cm}^2$ .

For morphological TAM imaging, the pump and probe beams are always overlapped in space and  $\Delta T$  is plotted as a function of probe position to form an image. The pump wavelength is at 630 nm, while a probe wavelength at 755 nm is employed to image the population of bulk carriers (Figure 3.7). For comparison, a probe wavelength at 785 nm ( $\sim 60$  meV below the bandgap) is utilized to selectively image the population of the sub-bandgap states (Figure 3.7). Based on the discussion above, the transient absorption signal at 785 nm is more likely to be associated with the grain boundaries. Note that photoinduced absorption due to bandgap renormalization of hot carriers could be present when probing at 785 nm at a time delay  $< 10$  ps.<sup>132</sup> To avoid this complication, the morphological TAM images are taken at a 10 ps pump–probe delay. At this time-delay, both probe wavelengths result in a ground-state bleach signal ( $\Delta T > 0$ ) (Figure 3.3 e).

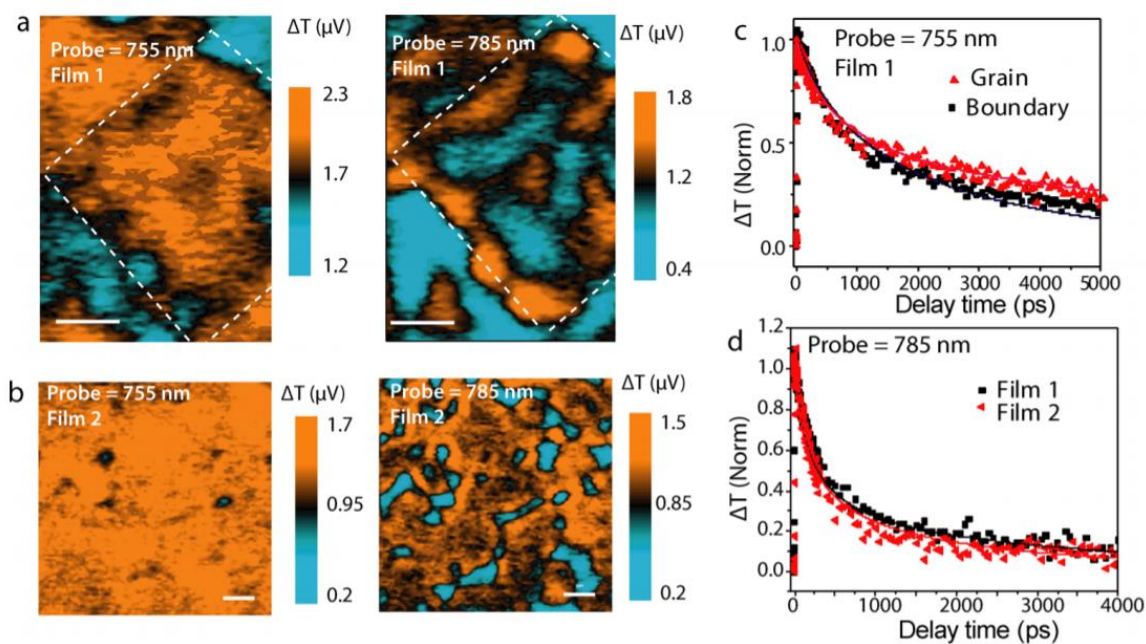


Figure 3.7 Morphological TAM images of film 1 (a) and film 2 (b) taken at a 10 ps time delay between the pump (630 nm) and probe (755 and 785 nm). Scale bars are 1  $\mu\text{m}$ . (c) Carrier dynamics probed at 755 nm within a grain and at the boundary of film 1. Solid lines are fits to equation 3.2. (d) Comparing carrier dynamics probed at 785 nm at the boundary for film 1 and film 2. Solid lines are fits to equation 3.2. The pump fluence is 1  $\mu\text{J}/\text{cm}^2$ . The carrier lifetime at the grain boundaries is determined from the fits to be  $9 \pm 1$  and  $5 \pm 1$  ns for film 1 and film 2, respectively.

The morphological TAM images (Figure 3.7 a for film 1 and Figure 3.7 b for film 2) confirm that the sub-bandgap states are indeed more prominent at the grain boundaries. For a grain in film 1 as outlined in Figure 3.7 a, the bulk carriers imaged at the bandgap by the 755 nm probe show relatively uniform  $\Delta T$  intensity within the grain, while the grain boundaries show slightly lower  $\Delta T$  intensity. Notably, the opposite is observed when the same grain is imaged with a 785 nm probe, with grain boundaries exhibiting significantly higher  $\Delta T$  intensity than the grain interior (Figure 3.7 a), demonstrating that sub-bandgap states are more prevalent at the boundaries. Overall, we observe a slightly shorter carrier lifetime when probing the grain boundaries (Figure 3.7 c) compared to the grain itself when probed at 755 nm. Similar results are observed for film 2 (Figure 3.7 b): the image with the 755 nm probe shows uniform  $\Delta T$  intensity, while the image probed at 785 nm exhibits greater contrast in intensity. Film 2 has more areas showing high-intensity  $\Delta T$  than film 1 when imaging with a 785 nm probe, indicating a higher density of grain boundaries. Film 2 also exhibits slightly faster decay when selectively probing the sub-bandgap state at 785 nm (Figure 3.7 d), likely due to more charge recombination. Note that the dynamics taken by TAM when the pump and probe beams are overlapped reflect both carrier diffusion and recombination and hence generally appear to be faster than the ensemble measurements (Figure 3.3 f). Both carrier diffusion and recombination are considered to fit the data presented in Figure 3.7 c and d using the model described later in this chapter.

### 3.5.2 Direct Visualization of Cross Grain Transport

To directly visualize how carrier transport is impacted by grain boundaries, a second mode of TAM is employed. We first image carrier transport in film 1, whose grain sizes are sufficiently large to differentiate transport within the grains from that across grain boundaries. In the transport imaging mode, the pump beam is held at a fixed position while the probe beam is scanned relative to the pump with a galvanometer scanner, and  $\Delta T$  is plotted as a function of probe position to form an image.<sup>21</sup> The pump wavelength is at 630 nm, while the probe wavelength is either at 755 or 785 nm. The resulting two-dimensional TAM transport images are shown in Figure 3.8 for the same area of film 1 imaged in Figure 3.7 a. The initial population is created by a Gaussian pump beam at position  $(x_0, y_0)$  with a pulse duration of  $\sim 300$  fs.

$$n(x, y, 0) = N \exp \left[ -\frac{(x-x_0)^2}{2\sigma_{x,0}^2} - \frac{(y-x_0)^2}{2\sigma_{y,0}^2} \right] \quad (3.1)$$

We first localize the pump beam within the same grain imaged in Figure 3.7 a. Upon excitation by the Gaussian pump beam, as indicated in Figure 3.8 a, the TAM image is the convolution of the pump and probe beams.

At later delay times, the TAM images reflect carrier diffusion away from the initial excitation volume. Here we focus on the transport beyond 10 ps to avoid the complications from hot carrier transport. Figure 3.8 b and c depicts the TAM images at 6 ns probed at 755 and 785 nm, respectively. If the carrier transport is diffusive, the time and spatially dependent carrier density is given by equation 3.2, where  $n(x, y, t)$  is the carrier population as a function of position and time,  $D$  is the diffusion coefficient, and  $\tau$  is the carrier lifetime.

$$\frac{\partial n(x, y, t)}{\partial t} = D \left[ \frac{\partial^2 n(x, y, t)}{\partial x^2} + \frac{\partial^2 n(x, y, t)}{\partial y^2} \right] - \frac{n(x, y, t)}{\tau} \quad (3.2)$$

We note here that both electrons and holes should contribute more or less equally to the transport due to their similar effective masses.<sup>67, 133</sup> At long delay time, imbalance of electron and

hole population could occur due to the difference in electron–hole recombination dynamics. However, this imbalance should not affect our conclusion significantly because electron and hole diffusion lengths over their lifetimes are comparable in polycrystalline films.<sup>134</sup>

As shown in Figure 3.8 b and c, carrier transport at a 6 ns delay is limited by the grain boundaries. This effect can be more clearly seen when using a probe wavelength of 785 nm that selectively images the sub-bandgap states (Figure 3.8 c), where the outline of the TAM image tracks the grain boundary and higher density of the sub-bandgap states is observed in the direction of slower carrier propagation. These results indicate that grain boundaries slow down carrier transport and they are not entirely benign. It is likely that potential barriers form by excessive PbI<sub>2</sub> insulating layers between grains also contributing to the observation of slowed carrier transport at the boundaries; however, the TAM measurements here do not directly probe these potential barriers.<sup>128, 135</sup>

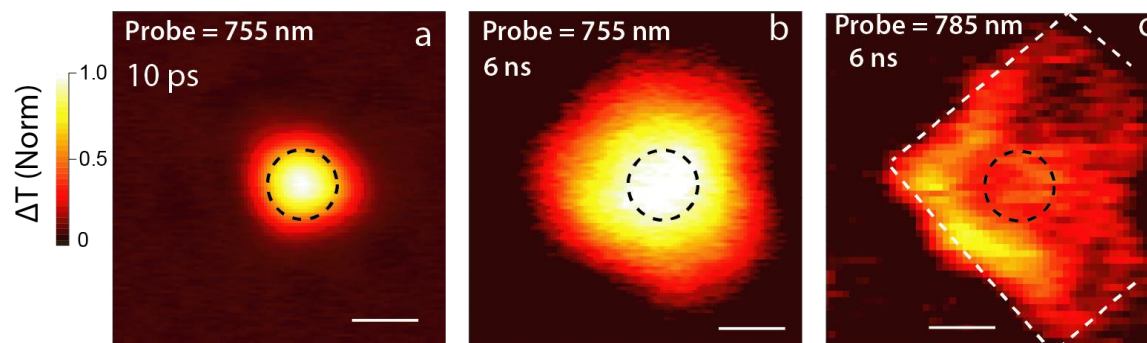


Figure 3.8 Carrier transport confined in a grain. TAM images of the carrier transport at a time delay of 10 ps (a) and 6 ns (b and c). The probe wavelength for a) and b) are 755 nm and 785 nm for c). The profile of the 630 nm pump beam is denoted by the dashed line circle in the center of each image. The pump fluence is 1  $\mu\text{J}/\text{cm}^2$  for all the images. Scale bars represent 1  $\mu\text{m}$ .

To extract quantitative information on the carrier transport across the grain boundaries, we directly measure the diffusion constant within a grain and across grain boundaries in film 1. The morphological TAM (Figure 3.9 a) and the correlated PL image (Figure 3.9 b) of the sample area

investigated shows uniform transient absorption, and the PL intensity indicates a large  $\mu\text{m}$  grain in the center of the image. Figure 3.9 c illustrates the TAM carrier diffusion at 10 ps and 5 ns. These images show that carrier transport across grain boundaries to the left is slower compared to transport to the right that occurs within the grain. Carrier dynamics are measured when the pump and probe beams are spatially separated by 600, 1050, and 1350 nm in both directions (Figure 3.9 d). The transient absorption signal is lower when probing away from the grain due to carriers diffusing into a thinner region.

The carrier dynamics reflect both carriers migrating away from the pump location as well as carrier recombination, as described by equation 3.2. We obtain the carrier diffusion constant for within and across grain boundaries by fitting the carrier dynamics taken at spatial separations of 1050 and 1350 nm between the pump and probe beams to equation 3.2, as shown in Figures 6.9 e and 6.10. A more rapid rise in the dynamics is observed for carrier transport within the grain compared to that across the grain due to larger carrier diffusion constants. The simulated diffusion constant for the transport within the grain is determined to be  $0.20 \pm 0.02 \text{ cm}^2\text{s}^{-1}$ , whereas the diffusion constant for the carrier transport across a grain boundary is  $0.12 \pm 0.02 \text{ cm}^2\text{s}^{-1}$ . The fitting of the dynamics obtained with a pump–probe separation of 1350 nm yields similar diffusion constants (Figure 3.10),  $0.20 \pm 0.05$  and  $0.12 \pm 0.05 \text{ cm}^2\text{s}^{-1}$  for within grain and across boundaries, respectively. The carrier lifetime within the grain for film 1 is found to be  $100 \pm 10 \text{ ns}$ . The diffusion constants are employed to fit the dynamics data presented in Figure 3.7 c and d. The carrier lifetimes at the grain boundaries are determined from the fits to be  $9 \pm 1$  and  $5 \pm 1 \text{ ns}$  for film 1 and film 2, respectively. Note that  $\Delta T$  represents the sum of carrier population over the entire film thickness, and the carrier diffusion constants measured here correspond to the integrated value over the depth direction. These measurements demonstrate that, despite carrier transport

being limited to some extent by the grain boundaries, carriers can still migrate efficiently across boundaries in film 1 with diffusion constants reduced by only a factor of about 2, indicating relatively shallow traps at the boundaries.

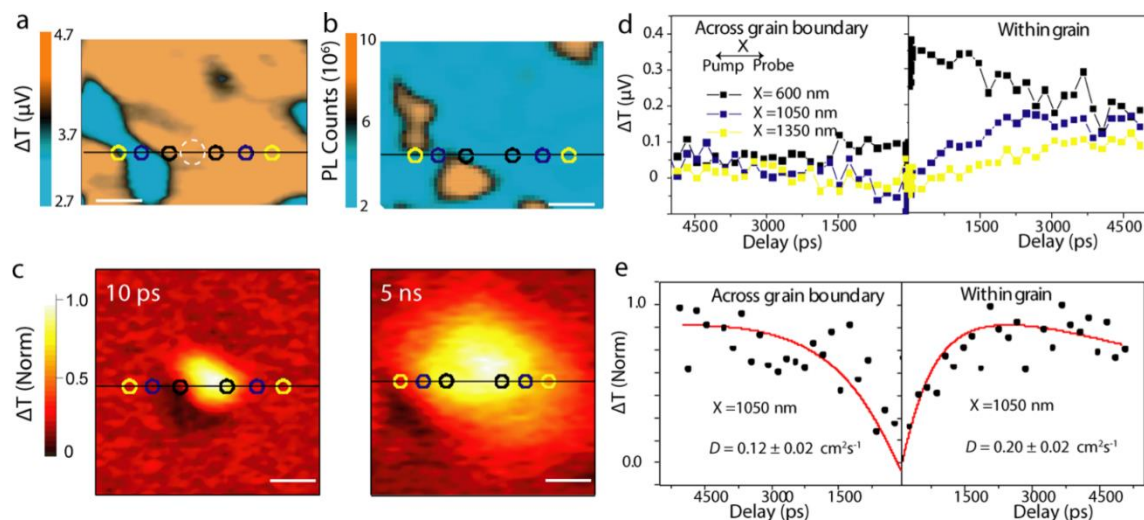


Figure 3.9 Carrier transport across a grain boundary in film 1. (a) Morphological TAM images of a perovskite thin film taken at a 10 ps time delay between the pump (630 nm) and probe (755 nm). The pump location is indicated by the dashed circle. (b) Correlated PL image of the same area as (a). (c) Carrier transport TAM images at 10 ps and 5 ns time delays. The pump wavelength is 630 nm, and the probe wavelength is 755 nm. Scale bars represent 1  $\mu\text{m}$ . (d) The carrier dynamics taken at pump-probe spatial separations of 600 (black), 1050 (blue), and 1350 nm (yellow) across the boundaries and within the grain. These areas are denoted by the corresponding colors in (a), (b) and (c). (e) Kinetic modeling of the carrier dynamics at a pump-probe separation of 1050 nm for transport across and within a grain. The red solid lines are fits to equation 3.2.

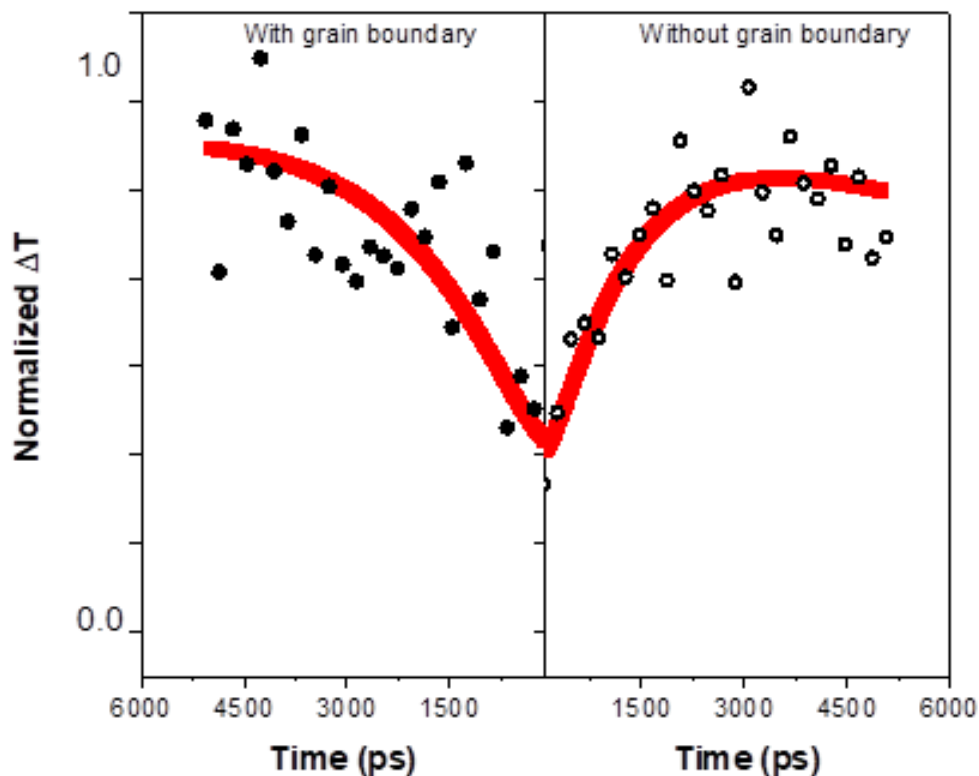


Figure 3.10 Simulation results from fitting the carrier dynamics taken at a pump probe separation of 1350 nm to obtain diffusion constants of  $0.20 \pm 0.05 \text{ cm}^2\text{s}^{-1}$  and  $0.12 \pm 0.05 \text{ cm}^2\text{s}^{-1}$  for within grain and across boundaries, respectively. The red lines are the results of fitting to equation 3.2.

Next, we image carrier transport in film 2 with smaller sized grains and more grain boundaries. The morphological TAM image of the area investigated (Figure 3.11 a) shows multiple grains. Within the experimental time window of 5 ns shown in Figure 3.11, carriers can migrate across multiple grains and over a distance of 100s of nm. Also indicated in Figure 3.11, carrier transport across different boundaries is heterogeneous; transport across certain grain boundaries is more rapid than that across others. As seen in the 2.5 ns delay image (Figure 3.11 c), carriers have arrived at a second grain to the lower right of the pump location. In contrast, carrier transport along the lower left direction is slower, as shown in the 5 ns delay image (Figure 3.11 d). Therefore, the detailed structure of the grain boundaries plays a role. For instance, it is

possible that there is more heterogeneity in grain orientation because grains of film 2 are more randomly oriented. In addition, how the grains are arranged in the depth direction of the film could also play a role, as indicated by previous conductivity atomic force microscopy (AFM) measurements.<sup>135</sup> The TAM results here are consistent with conductivity AFM measurements that reveal heterogeneity in lateral conductivity measurements across the grain boundaries.<sup>135</sup>

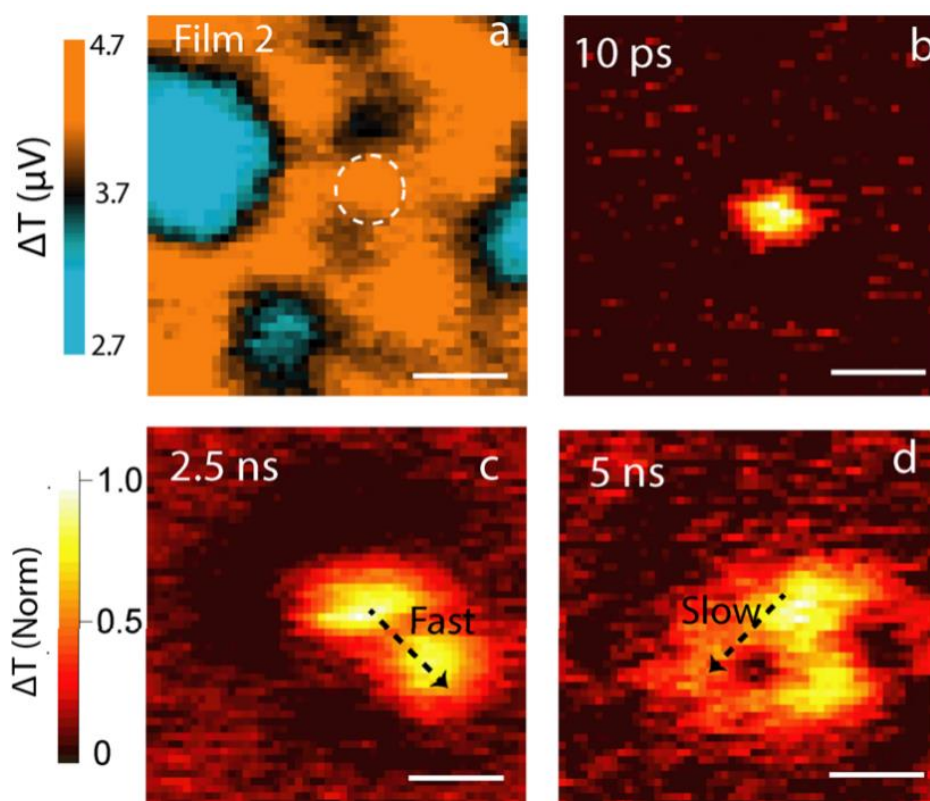


Figure 3.11 Carrier transport across grain boundaries in film 2. (a) Morphological TAM images of the perovskite thin film taken at a 10 ps time delay between the pump (630 nm) and probe (755 nm). The pump location is indicated by the dashed circle. Carrier transport TAM images at 10 ps (b), 2.5 ns (c), and 5 ns (d) time delays. The pump wavelength is 630 nm, and the probe wavelength is 755 nm. Scale bars represent 1  $\mu\text{m}$ .

The TAM results presented here can explain the seemingly contradicting observations of shortened PL lifetimes at the grain boundaries and their benign nature in charge generation in the literature. The sub-bandgap states at the grain boundaries lead to shorter PL lifetimes; however, the long carrier lifetime is still more than sufficient for the carrier to migrate over the boundaries. For the previous scanning probe measurements<sup>115, 126</sup> that are averaged over a long timescale ( $> \mu\text{s}$ ), conductivity and charge generation are not limited by transport across the boundaries, and therefore, the grain boundaries appear to be benign. The fact that grain boundaries only reduce the diffusion constant by a factor of 2 suggests that the sub-bandgap states in hybrid perovskites are relatively shallow, in contrast deep trap states in traditional semiconductors such as polycrystalline CdTe thin films.<sup>136</sup> While the TAM measurements here probe specifically the role of sub-bandgap states, potential barriers could also contribute to the slowed transport at the grain boundaries.

### 3.6 Conclusions

In summary, carrier transport within and across the boundaries in hybrid perovskite thin films has been spatially and temporally imaged utilizing ultrafast microscopy. By selectively imaging the sub-bandgap states, the TAM experiments directly visualize how these states impact carrier transport. While carrier transport across the boundaries is to some extent limited by the grain boundaries, carrier diffusion constants are only reduced by about a factor of 2 when the grain sizes are  $>1 \mu\text{m}$ . For a film with grain sizes on the order of 200 nm, carrier transport across multiple grain boundaries has been observed within a time window of 5 ns. These results reconcile the discrepancy regarding the role of grain boundaries in carrier dynamics and transport in the literature.

## CHAPTER 4. LONG RANGE HOT CARRIER TRANSPORT IN HYBRID ORGANIC-INORGANIC PEROVSKITES

### 4.1 Abstract

The Shockley-Queisser limit for solar cell efficiency can be overcome if hot carriers can be harvested before they thermalize. Recently, carrier cooling times up to 100 picoseconds were observed in hybrid perovskites, but it is unclear whether these long-lived hot carriers can migrate long distance for efficient collection. Here, we report direct visualization of hot-carrier migration in methylammonium lead iodide ( $\text{CH}_3\text{NH}_3\text{PbI}_3$ ) thin films by ultrafast transient absorption microscopy. This work demonstrates three distinct transport regimes. (i) Quasiballistic transport, (ii) nonequilibrium transport, and (iii) diffusive transport. Quasiballistic transport was observed to correlate with excess kinetic energy, resulting in up to 230 nanometers of transport distance that could overcome grain boundaries. The nonequilibrium transport persisted over tens of picoseconds and ~600 nanometers before reaching the diffusive transport limit. These results suggest potential applications of hot-carrier devices based on hybrid perovskites to ultimately overcome the Shockley-Queisser limit.

### 4.2 Introduction

Hot (nonequilibrium) carrier thermalization is one of the major sources for efficiency loss in solar cells.<sup>137</sup> The term “hot carriers” refers to electrons (or holes) that have gained an extensive amount of kinetic energy from an external source, such as absorption of high energy photons. In the case of semiconductors for photovoltaic applications, the active layer material can absorb photons of higher energy than the bandgap, which leads to photogenerated carriers having excess kinetic energy and being promoted to higher levels within their respective bands.<sup>138</sup> An illustrative

representation of hot carrier population within the band structure is shown by Figure 4.1. Typically, this excess energy gets dissipated as heat and leads to huge efficiency loss. Such loss can be reverted if the hot carriers can be harvested before they equilibrate with the lattice, and the ultimate thermodynamic limit on conversion efficiency can be increased from the Shockley-Queisser limit of 33% to about 66%.<sup>137, 139</sup>

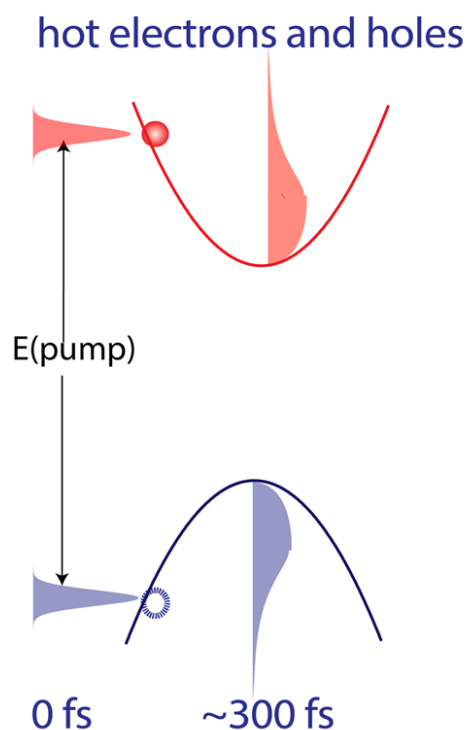


Figure 4.1 Illustration of hot carriers within the band structure.

The main challenge for harvesting hot carriers is the relatively short distance they travel before losing their excess energy to the lattice, typically on the picosecond time scale.<sup>138, 140-144</sup> Hybrid organic-inorganic metal halide perovskites, such as  $\text{MAPbI}_3$ , have emerged to be a class of highly efficient solar cell materials with remarkable charge transport properties, achieving efficiency above 20%.<sup>12, 52, 90, 134, 145</sup>

Recently, ultrafast spectroscopic measurements have revealed surprisingly long-lived hot carriers on the order of 100 ps in these hybrid perovskites.<sup>146-150</sup> The remarkably long hot-carrier lifetime in the hybrid perovskites, about two to three orders of magnitude longer than in conventional semiconductors, raises the question of whether hot carriers can be harvested to overcome the Shockley-Queisser limit. However, the current understanding on hot-carrier transport in hybrid perovskites is limited, despite efforts that have been devoted to studying carrier cooling dynamics.<sup>76, 146-152</sup> In particular, the crucial parameter of hot-carrier transport length must be comparable to the thickness necessary for photon absorbance. To correctly evaluate the potential of hot-carrier perovskite solar cells, measurements to provide quantitative results on the length scales of hot carrier transport in relation to carrier cooling time scales are necessary. Combining microscopy techniques with ultrafast optical pumping can be an effective solution for achieving simultaneous temporal and spatial resolutions of carrier dynamics.<sup>22, 153-155</sup> In this work, we report on a direct visualization of hot-carrier transport in  $\text{CH}_3\text{NH}_3\text{PbI}_3$  thin films using ultrafast transient absorption microscopy (TAM) with 50 nm spatial precision and 300 fs temporal resolution. These experiments revealed three distinct transport regimes, specifically, quasiballistic transport for the initially generated hot carriers, nonequilibrium transport for the protected long-lived hot carriers, and diffusive transport for the cooled (equilibrium) carriers.

#### 4.3 Material Preparation

The perovskite thin film was prepared from a non-stoichiometric precursor as reported previously.<sup>156</sup> Briefly, methylammonium iodide (MAI) and lead iodide ( $\text{PbI}_2$ ) (MAI/ $\text{PbI}_2$ =1.2/1) was dissolved in N-Methyl-2-pyrrolidone (NMP) and gamma-Butyrolactone (GBL) (NMP/GBL=7/3 volume ratio) to form 50 wt% precursor solution.  $\text{SiO}_2$  substrate with dispersed precursor was spun at 4500 rpm for 25 s, and promptly transferred into abundant diethyl ether

(DEE) solution for crystallization. After 1 min of bathing in DEE, the substrate was thermally annealed at 150°C with a petri-dish covered in air for 15 min. Figure 4.2 shows a scanning electron microscopy (SEM) image of the sample under investigation.<sup>132</sup> Solar cell efficiencies of ~18% have been achieved by using films fabricated with the same procedure.<sup>156</sup> The absorption and photoluminescence spectra of the thin film investigated are shown in Figure 4.3.

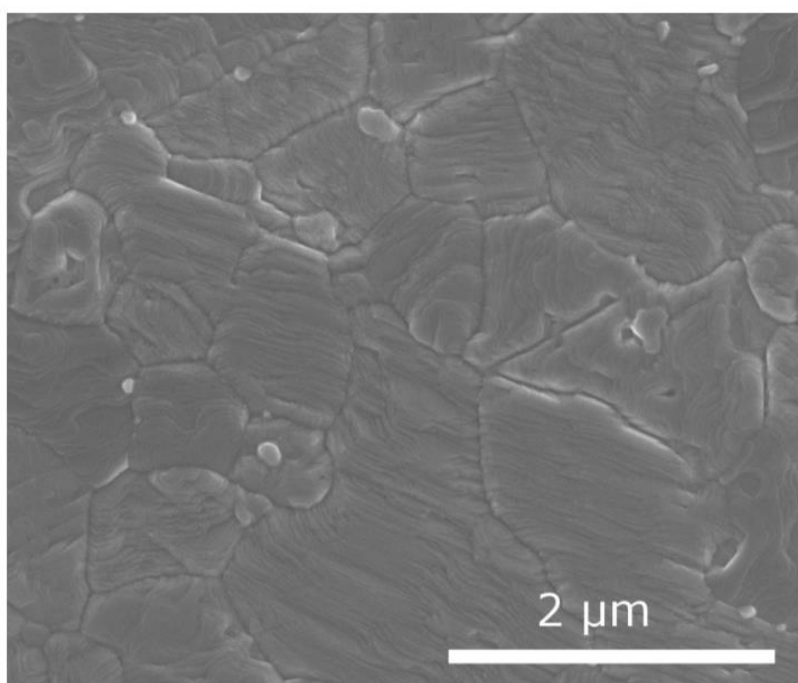


Figure 4.2 Scanning electron microscopy (SEM) image of the  $\text{CH}_3\text{NH}_3\text{PbI}_3$  thin film used in this work.

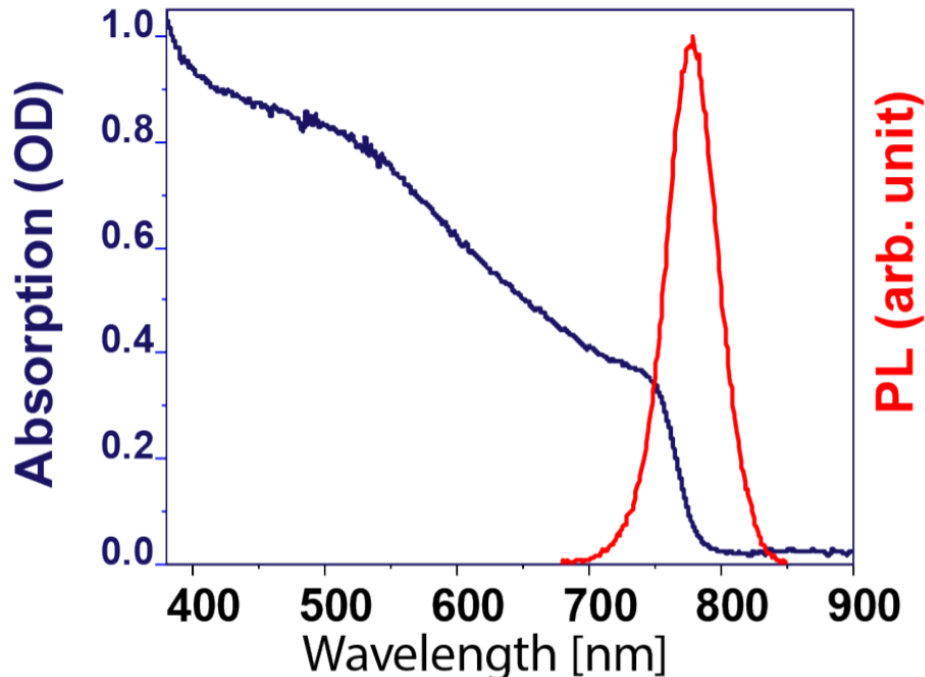


Figure 4.3 Absorption and Photoluminescence spectra of the MAPbI<sub>3</sub> investigated in this work.

#### 4.4 Results and Discussion

##### 4.4.1 Determination of Hot Carrier Spectral Signature

To establish spectroscopic signatures for hot carriers, we carried out ensemble transient absorption measurements. Figure 4.4 depicts the method for determination of hot carrier spectral signature. Based on this schematic, we can see that the higher pump photon energies (red > yellow > green > blue > black) should correspond to a more “hot” carrier (i.e. excited higher into the conduction band; having excess kinetic energy). Immediately after photoexcitation, a photoinduced absorption (PIA, negative change of transmission  $\Delta T/T$ ) band centered at 1.58 eV was observed whose amplitude ( $|\Delta T/T|$ ) increased as the pump photon energy increased (shown in Figure 4.5A). Global analysis (Figure 4.5B) indicates that this PIA band is associated with a broadened ground-state bleach (GSB, positive  $\Delta T/T$ ) band with a high-energy tail consistent with a Fermi-Dirac distribution at high carrier temperatures. The PIA band resulted from the shifting

of the band-gap energy,  $\Delta E_g$ , which was a combination of band-gap renormalization effect (narrowing the band gap by  $\Delta E_{BGN}$ ) and Burstein-Moss effect (or band-filling, widening the band gap by  $\Delta E_{BM}$ ), as described by  $\Delta E_g = \Delta E_{BM} - \Delta E_{BGN}$ .<sup>157</sup> Since  $\Delta E_{BM}$  would not take effect until the hot carriers relax to the band edge, the red-shifted PIA band at 1.58 eV at 0 ps was due to  $\Delta E_{BGN}$  predominantly. The amplitude of the PIA band increased as the pump photon energy increased (seen in Figure 4.5A), which could be explained by the decreased occupation of the states near the band edge leading to a decreased  $\Delta E_{BM}$ .

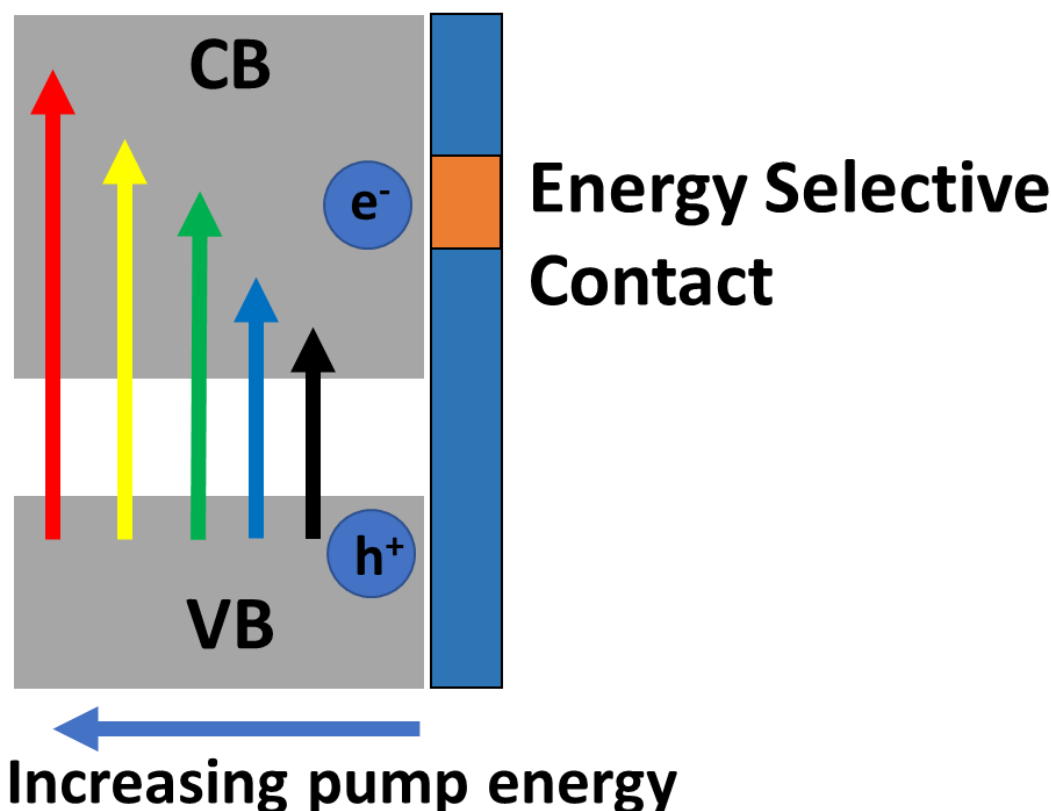


Figure 4.4 Illustration depicting increasing pump photon energy to generate hot carriers. Energy selective contact is included to show the potential for extraction of hot charge carriers.

Once the carriers have cooled down and  $\Delta E_{BM}$  settled in, the PIA band at 1.58 eV decayed and a blue-shifted PIA band was observed. This is easily seen with the transient absorption spectra

at various time delays in Figure 4.6. Based on these observations, we assigned the PIA band at 1.58 eV to hot carriers, in agreement with previous reports.<sup>158, 159</sup> Additionally,  $\Delta T/T$  of the PIA band had a different dependence on carrier density,  $n$ , than that of the GSB band, when probed at 1.58 eV (Figure 4.5C).  $\Delta T/T$  of the GSB band scaled linearly with  $n$ , whereas  $\Delta T/T$  of the PIA band was proportional to  $n^{1/2}$ . Since  $\Delta T/T$  of the PIA band scaled linearly with  $\Delta E_{\text{BGN}}$  as empirically shown in reference 111, this observation indicated that  $\Delta E_{\text{BGN}}$  is proportional to  $n^{1/2}$ . A dependence of  $n^{1/3}$  for  $\Delta E_{\text{BGN}}$ , is generally expected when carriers are weakly interacting, but an  $n^{1/2}$  term must be included when carrier-carrier interactions become more important.<sup>157, 160</sup> For instance, the  $n^{1/2}$  dependence becomes dominant at  $n > 10^{17} \text{ cm}^{-3}$  for GaAs.<sup>160</sup> The  $n^{1/2}$  dependence observed here implies that carrier-carrier interactions are not negligible for MAPbI<sub>3</sub>.

The PIA band decayed with a  $\sim 400$  fs time constant when excited at 3.14 eV (Figure 4.5B), which has been assigned to the emission of the longitudinal optical phonons.<sup>76, 146, 161</sup> The lifetime for the PIA band shortened to  $\sim 280$  fs when the pump photon energy was reduced to 1.97 eV, as seen in Figure 4.7. The decay of the PIA band was accompanied by the growth of the GSB band at the band edge (Figure 4.5D). Also shown in Figure 4.5D is a second and slower cooling process with a time constant of  $\sim 78$  ps. This much slower cooling phase has been ascribed to the protection of the energetic carriers by the formation of large polarons<sup>147, 148</sup>, hot phonon effects<sup>146</sup> (when carrier densities are larger than  $10^{18} \text{ cm}^{-3}$ ), and optical-acoustic phonon scattering<sup>149</sup>. After the confirmation of the spectral signature of hot carriers, we can spectrally observe the probe wavelength needed for the transport measurements to be 1.58 eV (785 nm).

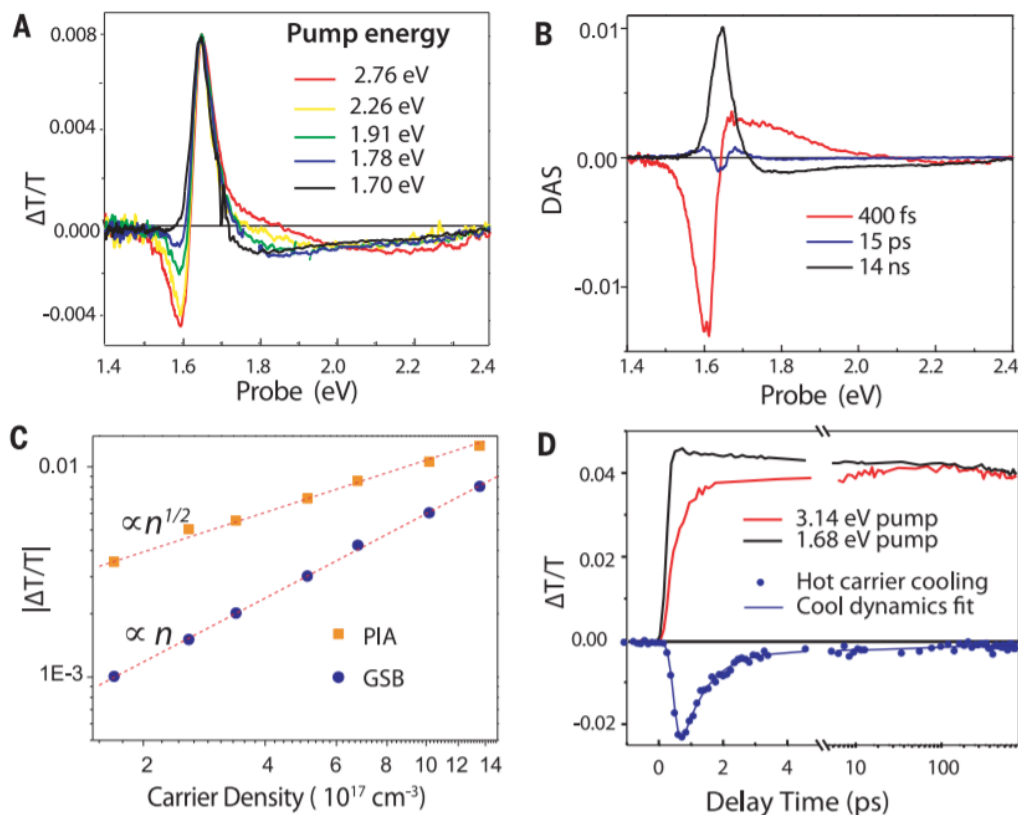


Figure 4.5 (A) Ensemble transient absorption spectra taken at 200 fs delay with different pump photon energies and change of transmission  $\Delta T/T$  was plotted. The pump fluences were calibrated to the same carrier density of  $10^{17} \text{ cm}^{-3}$ . (B) Decay-associated spectra (DAS) for a pump photon energy of 3.14 eV obtained by performing global analysis on the transient spectra. (C) Carrier density dependence of  $\Delta T/T$  of the PIA band (taken at maximum value) and that of the GSB band (4 ps time delay) for a pump photon energy of 3.14 eV and a probe energy of 1.58 eV. (D) Hot-carrier cooling dynamics obtained by subtracting the carrier relaxation kinetics driven by 3.14 eV photon excitation from those induced by 1.68 eV excitation plotted along with a biexponential fit.

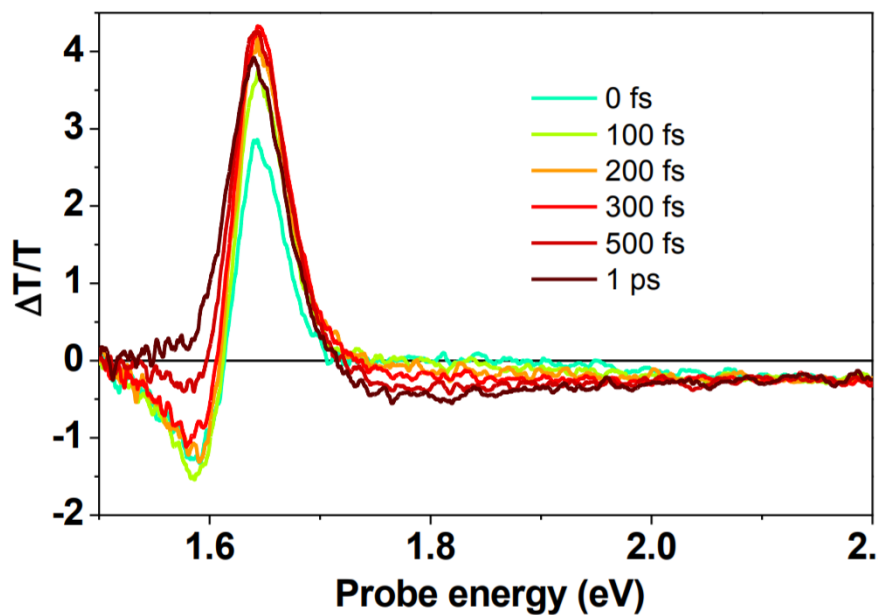


Figure 4.6 Ensemble transient absorption spectra taken at different pump-probe delays with a pump photon energy of 3.14 eV and change of transmission  $\Delta T/T$  was plotted to observe the growth of broad blue shifted PIA, as hot carriers decay.

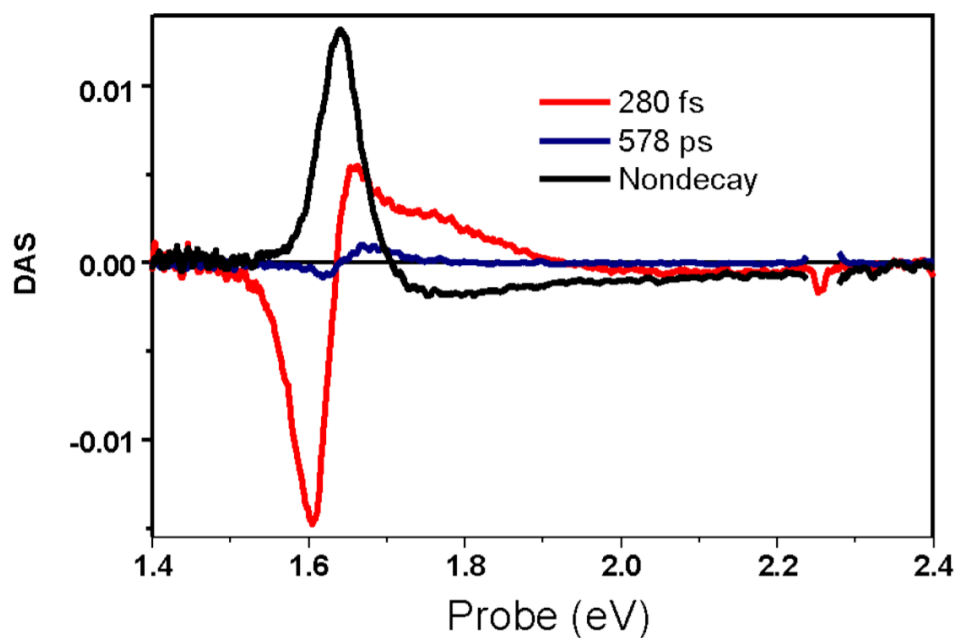


Figure 4.7 Decay associated spectra (DAS) for pump photon energy of 1.97 eV through performing global analysis on the transient spectra.

#### 4.4.2 Direct Visualization of Hot Carrier Transport

We imaged hot-carrier transport initiated by two different pump photon energies: 3.14 eV and 1.97 eV, which are 1.49 eV and 0.32 eV above the bandgap, respectively. The probe photon energy was 1.58 eV, to selectively probe the hot carriers. The pump beam was held at a fixed position while the probe beam was scanned relative to the pump with a pair of galvanometer scanners to form an image (Figure 2.3 – path 1).<sup>21, 22, 132</sup> The precision in determining carrier propagation distance was dictated by the smallest measurable change in the excited state population profiles and not directly by the diffraction limit.<sup>86</sup> This limit is  $\sim 50$  nm for the current experimental conditions, as discussed in Chapter 2 (Section 2.5.2). The pump fluence for both measurements was  $\sim 2 \mu\text{J}/\text{cm}^2$ , which corresponds to a carrier density for these measurements was  $\sim 4 \times 10^{17} \text{ cm}^{-3}$ , where Auger recombination and hot phonon effect were negligible based on the results shown in Figure 4.8. Here, we can see no change in carrier dynamics when pumping different carrier densities, which indicates there is negligible contribution from annihilation, hot photon effect, and Auger recombination.<sup>21, 148</sup>

The initial population was created by a Gaussian pump beam at position  $(x_0, y_0)$ , with a pulse duration of  $\sim 300$  fs. We defined an instrument response function  $(\text{IRF}) = (\sigma^2(\text{pump}) + \sigma^2(\text{probe}))^{1/2}$  that described the response of a pump-probe microscope to a point object, where  $\sigma^2(\text{pump})$  and  $\sigma^2(\text{probe})$  were the variance of the Gaussian pump and probe beams. The IRF was determined to be  $260 \pm 5$  nm (Figure 4.9C) by measuring a tetracene single crystal under similar experimental conditions at 0 ps because exciton transport within the pulse width for tetracene is negligible.<sup>22</sup>

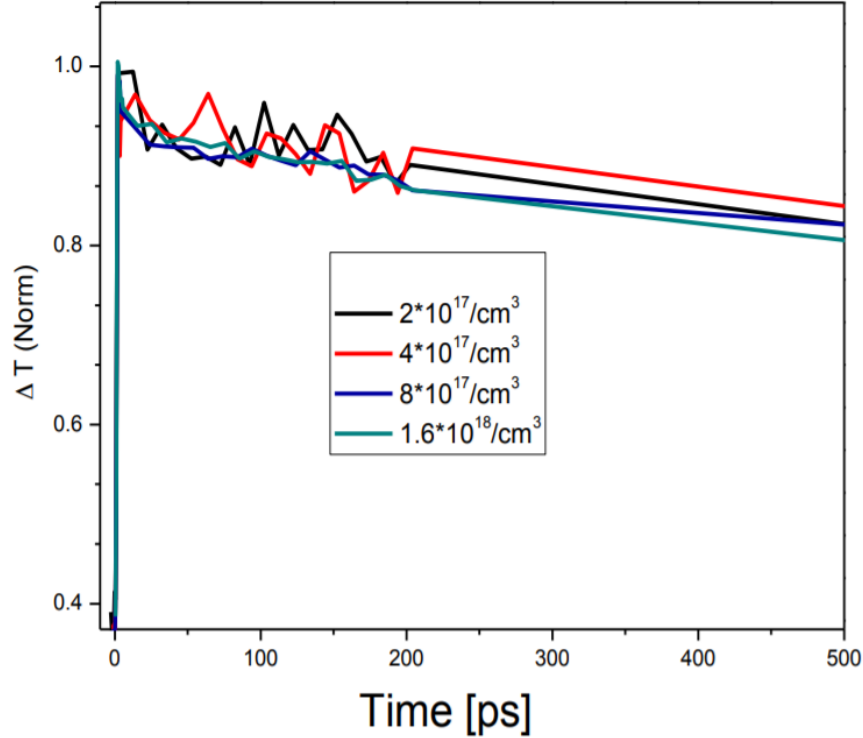


Figure 4.8 Carrier density dependent dynamics when pump and probe beams are overlapped in the center. Pump = 3.14 eV, probe = 1.65 eV.

At 0-ps time delay, the carrier distribution should be equal to the convolution of the probe and probe beams if no transport occurs within the pulse width. Only a negative  $\Delta T$  (PIA) was observed at a 0 ps time delay, which is indicative of the initially created carriers being out of equilibrium for both pump photon energies. Since the  $\Delta T_{\text{PIA}}$  is proportional to  $n^{1/2}$ , the carrier distribution can be obtained by  $n(x, y, 0) \propto [T_{\text{PIA}}(x, y, 0)]^2$ . For 3.14 eV photon excitation, the 0 ps image showed morphology dependent structures that are not easily described by a Gaussian function (Figure 4.9A). To average out the morphological effects, we interpolated  $[T_{\text{PIA}}(x, y, 0)]^2$  onto a polar coordinate, summed over all angles, and plotted it as a function of radial distance (Figure 4.9C). The carrier distribution at 0 ps was fit by a Gaussian function with a variance,  $\sigma_0^2$ , of  $350 \pm 10$  nm, which is much larger than that of the IRF (Figure 4.9C). Thus, hot carrier transport

must have occurred within the pulse duration. The transport distance within the pulse width was calculated as  $(\sigma_0^2 - \text{IRF}^2)^{1/2} = 230 \pm 16$  nm. In contrast, when the pump photon energy was reduced to 1.97 eV (near band edge excitation), negligible carrier transport within the pulse width was observed (Figure 4.9B) and the initial hot carrier population distribution was comparable to the IRF (seen by Figure 4.10).

The excess energy dependent carrier transport distance within the pulse width indicated that ballistic carrier transport played a role. Compared to diffusive transport, which is known as a “random walk” due to scattering, ballistic transport is highly directional, having a specific trajectory and traveling systematically. When promoting carriers from the valance band to the conduction band, the excess energy above the band gap manifested as kinetic energy and distributed among the electrons and holes inversely proportional to their respective effective masses,  $m_e^*$  and  $m_h^*$ ,<sup>139</sup> which for MAPbI<sub>3</sub> both have a value of  $\sim 0.2m_0$ , the free electron mass.<sup>67,</sup>

<sup>162</sup> The ballistic velocity of the carriers,  $v_{max}$ , is given by  $K_{e(h)} = \frac{1}{2} m_{e(h)}^* v_{max}^2$ , leading to a value of  $1.6 \times 10^6$  and  $0.7 \times 10^6$   $\text{ms}^{-1}$  for 3.14 eV and 1.97 pump photon energies, respectively. For 3.14 eV excitation, the expansion of the width of the TAM image within the pulse width gave a velocity of  $230 \text{ nm}/300 \text{ fs} = 0.8 \times 10^6$   $\text{ms}^{-1}$ , on the same order as  $v_{max}$ , indicating that the carrier motion was quasiballistic. Our time resolution was unable to resolve ballistic transport directly. Intriguingly, very little quasiballistic transport was observed for 1.97 eV excitation, which was probably limited by grain boundaries. There could be additional potential barriers at interfaces or “dynamic” barriers created by the fluctuating energy landscape that could also require excess kinetic energy to overcome.<sup>100</sup> The larger initial kinetic energies of the hot carriers created by 3.14 eV pump allowed more carriers to overcome grain boundaries, as shown in the 0 ps image in Figure 4.9A.

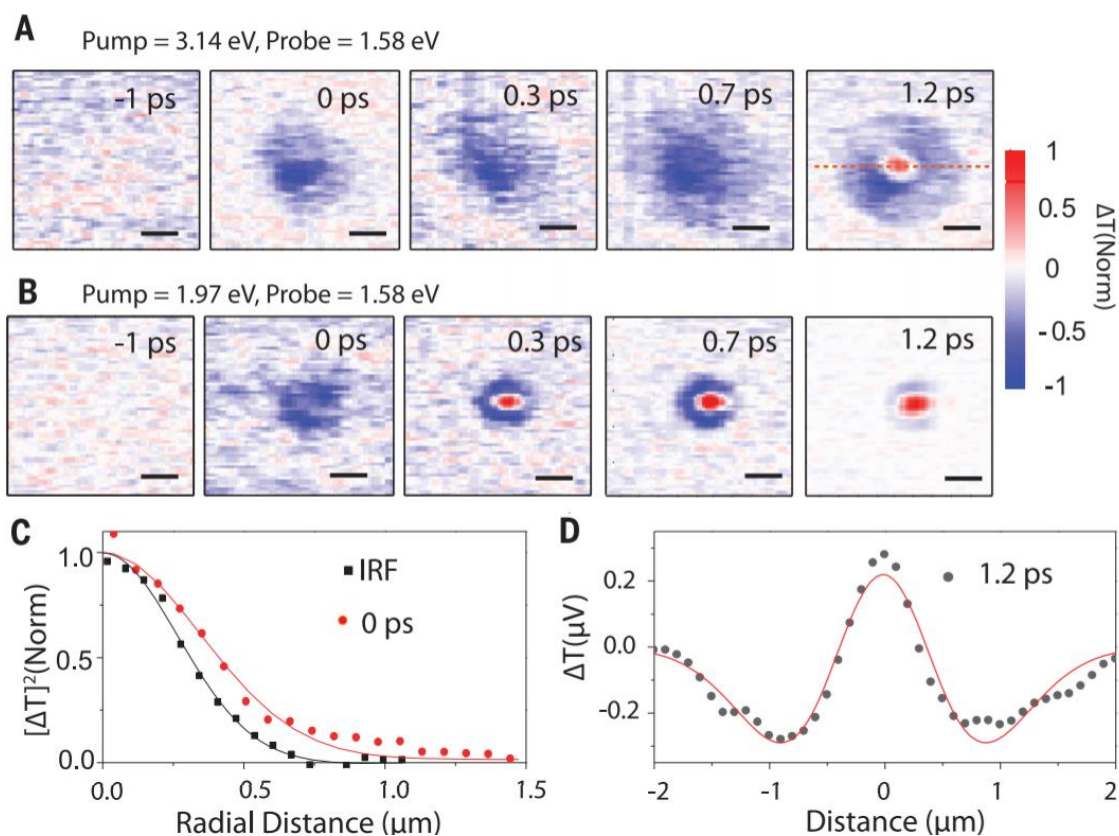


Figure 4.9 TAM images probing at 1.58 eV with two pump photon energies— (A) 3.14 eV and (B) 1.97 eV— at different pump-probe delay times, as labeled. Scale bars, 1  $\mu\text{m}$ . (C) Hot-carrier distribution at 0-ps delay for 3.14 eV excitation over a radial distance obtained by averaging all angles compared to the IRF, as defined in the text. Solid lines are Gaussian fits. (D) One-dimensional TAM image profile at 1.2 ps for 3.14 eV pump excitation. The red solid line is fit as described in the text. The red dashed line in (A) indicates where the 1D distribution was obtained in (D).

Carrier cooling was also visualized by TAM, manifested as the negative  $\Delta T$  signal (PIA) turning into the positive  $\Delta T$  signal (GSB). The GSB signal appeared sooner for the 1.97 eV pump (after 300 fs) than for the 3.14 eV pump (after 1 ps), consistent with less excess energy to lose to the phonons. The GSB signal presented initially only in the center of TAM images, which can be explained by the PIA and the GSB  $\Delta T$  having opposite signs and different carrier density dependence, i.e.  $\Delta T_{PIA}(x, y, t) \propto -n(x, y, t)^{\frac{1}{2}}$  and  $\Delta T_{GSB}(x, y, t) \propto n(x, y, t)$ . The TAM profiles were then fitted using two-dimensional (2D) Gaussian functions for  $n(x, y, t)$ , with variances of  $\sigma_{x,t}^2$  and  $\sigma_{y,t}^2$ . This was performed as the sum of the two types of signals,  $\Delta T_{GSB}(x, t) + \Delta T_{PIA}(x, t) = An(x, t) - Bn(x, t)^{\frac{1}{2}}$ , where parameters A and B are the relative weight of the cooled and hot carriers, respectively.  $n(x, y, t)$  is approximated by a 2D Gaussian function:

$$N \exp\left[-\frac{(x-x_0)^2}{2\sigma_{x,t}^2} - \frac{(y-y_0)^2}{2\sigma_{y,t}^2}\right].$$

Fitting along one dimension for 1.2 ps pump-probe delay is shown in Figure 4.9D, and data for 100 ps time delay is shown in Figure 4.11. Since the carrier transport was isotropic, i.e.,  $\sigma_{x,t}^2 \approx \sigma_{y,t}^2$ , we reduced the problem to one dimension and defined  $\sigma_t^2 = \frac{\sigma_{x,t}^2 + \sigma_{y,t}^2}{2}$  to average out morphological effects and plotted it as a function of pump-probe delay time, shown in Figure 4.12A and B. Carriers continued to move more rapidly for 3.14 eV excitation than 1.97 eV excitation on the 10s of picosecond time scale, as the second and slower phase of carrier cooling set in,<sup>147-149</sup> this is seen in Figure 4.12B and C. For 1.97 eV pump,  $\sigma_t^2$  grew linearly as a function of delay time for  $> 1$  ps, which is indicative of diffusive transport as described by  $\sigma_t^2 - \sigma_0^2 = 2D$  ( $D$  is the diffusion coefficient,  $0.7 \pm 0.1 \text{ cm}^2\text{s}^{-1}$ ).<sup>86</sup> This large diffusion coefficient is consistent with the high crystallinity of our sample.<sup>163</sup> Diffusive transport indicated that thermal equilibrium with the lattice was reached. However, for the 3.14 eV excitation, diffusive transport was not observed until after 30 ps, and hot carriers migrated  $\sim 600$  nm before reaching thermal

equilibrium with the lattice. The diffusion coefficient was identical for 3.14 eV and 1.97 eV excitation after 100 ps. Recently, Li et al. estimated almost an order of magnitude shorter hot-carrier transport distance of 16 to 90 nm for films of MAPbBr<sub>3</sub> nanoparticles,<sup>150</sup> even though hot-carrier cooling times were two orders of magnitude slower in these nanoparticles than in bulk films. Thus, our results suggest that slow carrier cooling alone does not necessary lead to long-range transport, and morphology is also a critical factor.

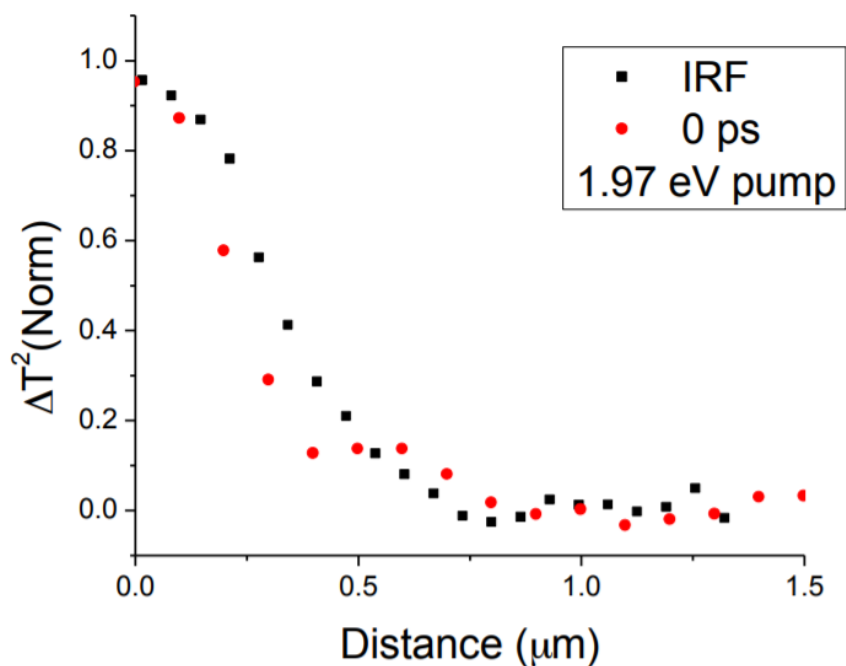


Figure 4.10 One-dimensional carrier distribution at 0 ps delay for 1.97 eV pump excitation compared to an instrument response function  $(\text{IRF}) = (\sigma^2(\text{pump}) + \sigma^2(\text{probe}))^{1/2}$

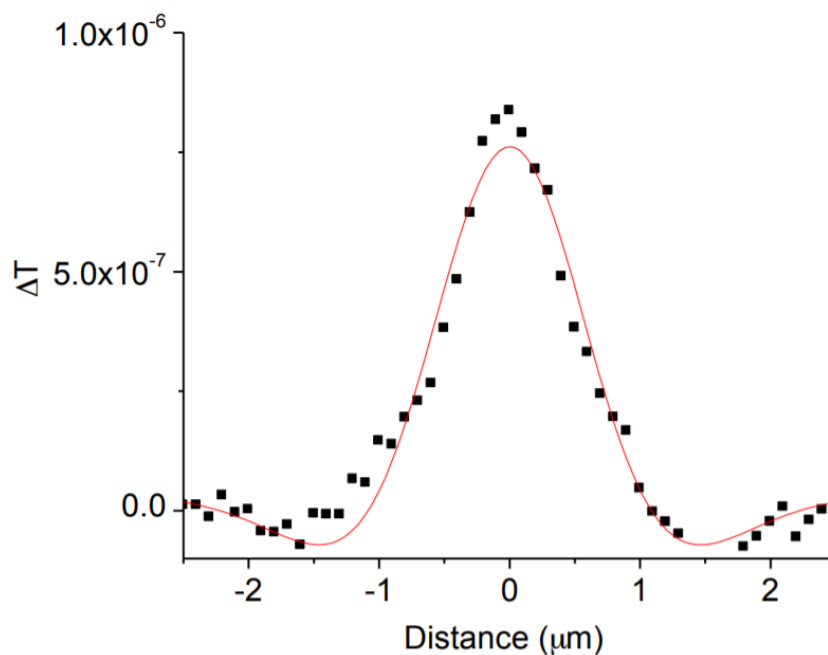


Figure 4.11 One-dimensional carrier distribution at 100 ps delay for 3.14 eV pump excitation. The TAM signal was fitted as the sum of the two types of signals:  $\Delta T_{GSB}(x, t) + \Delta T_{PIA}(x, t)$

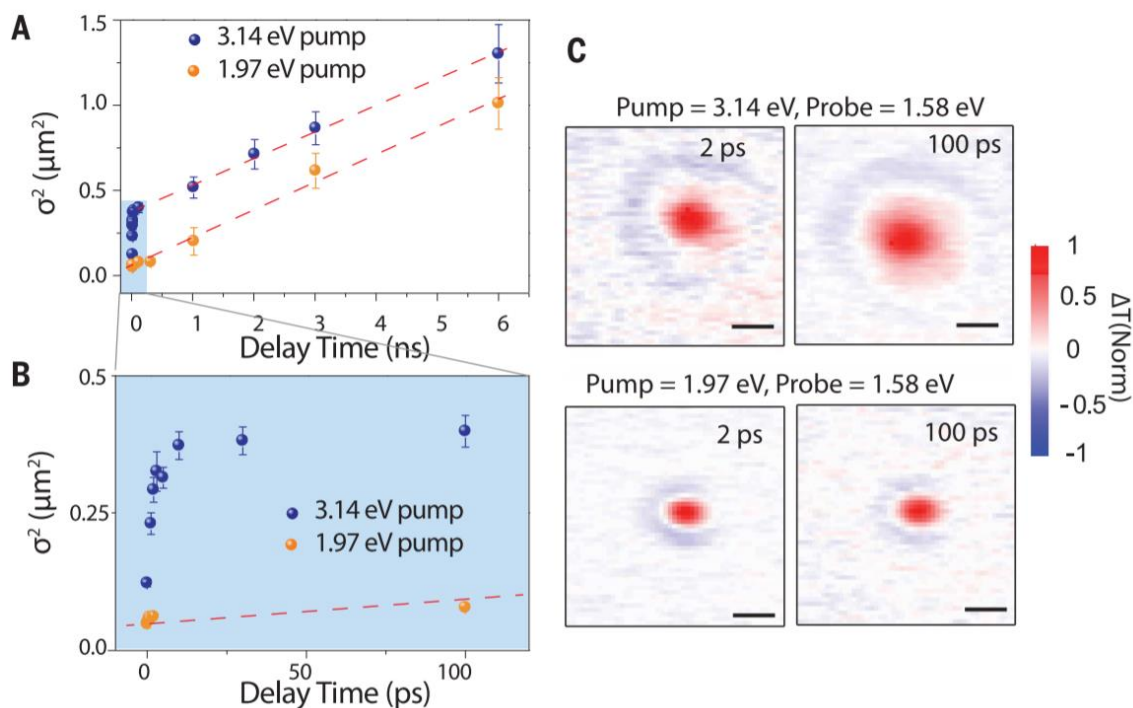


Figure 4.12 Nonequilibrium to diffusive transport transition. (A)  $\sigma_t^2$  plotted as a function of pump-probe delay time up to 6 ns for 1.97 eV and 3.14 eV pump photon energies. Linear fits are shown in dashed red lines to indicate diffusive transport with  $L^2 = \sigma_t^2 - \sigma_0^2 = 2Dt$ . (B) Zoomed in view of (A) for the time scale up to 100 ps. (C) TAM images at 2 ps and 100 ps for 3.14 eV and 1.97 eV pump photon energies. Scale bar: 1  $\mu\text{m}$ .

We calculated the effective diffusion constant as  $D(t) = \frac{\Delta\sigma_t^2(t)}{2\Delta t}$  for the 3.14 eV excitation.  $D(t)$  decreased from an initial value of  $450 \pm 10 \text{ cm}^2\text{s}^{-1}$  at 1 ps to the equilibrium value of  $0.7 \pm 0.1 \text{ cm}^2\text{s}^{-1}$  and could be fitted to a biexponential decay function with decay constants of  $3 \pm 1 \text{ ps}$  and  $20 \pm 5 \text{ ps}$ , respectively (Figure 4.13A). The time constants for the decay agreed overall with carrier cooling time. The fast decay-time constant (3 ps) was slower than that determined from the ensemble transient absorption measurements (400 fs), which can be understood as that the ensemble measurements integrating over a large area underestimated the cooling time because the PIA and GSB signals canceled each other out. Time dependent carrier transport behavior was also observed directly in the corresponding carrier dynamics when probing away from the pump beam center with a 3.14-eV pump (Figure 4.13B). The rapid growth of hot carrier population (negative  $\Delta T$  signal) when probing 1  $\mu\text{m}$  and 1.5  $\mu\text{m}$  away from the pump center, persisted up to  $\sim 3 \text{ ps}$ , which is in good agreement with the initial fast transport. Then growth slowed down on the 10s of picosecond time scale. Additionally, the fast growth was absent when probing 2  $\mu\text{m}$  away because the initial fast transport did not reach that distance.

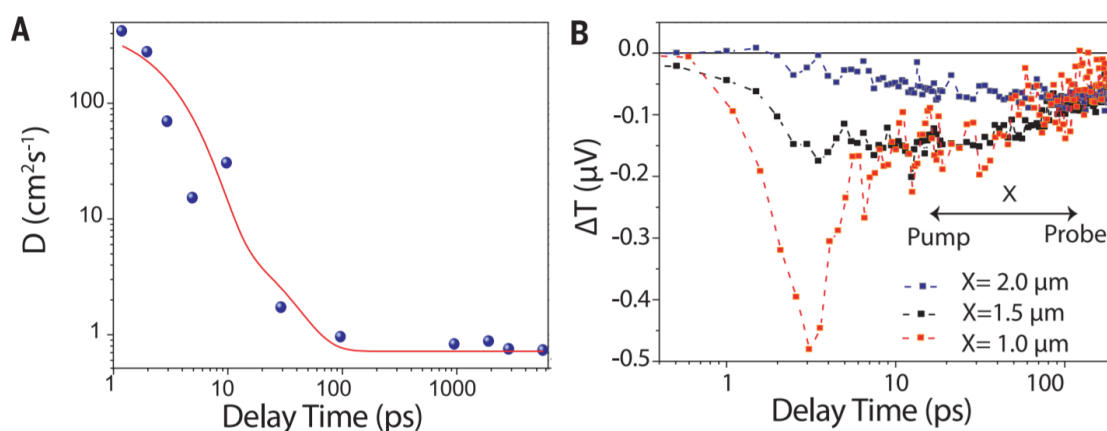


Figure 4.13 (A) Effective diffusion constant,  $D(t)$ , calculated as a function of delay time for 3.14-eV photon excitation. The red solid line is the fit to a biexponential decay function. (B) Kinetics probed at pump-probe distances as labeled for pump photon energy of 3.14 eV.

To understand the factors contributing to the extraordinary long-range hot-carrier transport, we compared MAPbI<sub>3</sub> to other conventional inorganic semiconductors. MAPbI<sub>3</sub> has comparable electron effective mass as Si,<sup>164, 165</sup> and the ballistic velocity on the order of  $10^6 \text{ ms}^{-1}$  is also consistent with recent calculation for Si.<sup>142</sup> The quasiballistic transport length of  $\sim 230 \text{ nm}$  in 300 fs for MAPbI<sub>3</sub>, however, is much longer than that of  $\sim 85 \text{ nm}$  for GaAs,<sup>166</sup>  $\sim 20 \text{ nm}$  for Si,<sup>142</sup> and  $\sim 14 \text{ nm}$  for GaN<sup>167</sup> and can be explained by slower momentum relaxation in MAPbI<sub>3</sub> than in conventional semiconductors,  $\sim 100 \text{ fs}$  as predicted by first principle calculations for hot carriers with excess energy of 1 eV.<sup>161</sup> In comparison, relaxation times of 10 to 20 fs were found for hot carriers with excess energy  $> 0.3 \text{ eV}$  for Si.<sup>142</sup>

The nonequilibrium transport behavior of carriers in MAPbI<sub>3</sub>, over 10s of picoseconds, also deviates from conventional semiconductors such as Si and GaAs, for which equilibrium with the lattice is achieved in a few picoseconds.<sup>141, 168</sup> Interestingly, nonequilibrium carrier transport on the picosecond time scale was not observed when pump photon energy is reduced to 1.97 eV. An energetic E\* state with an energy of  $\sim 0.3 \text{ eV}$  above the band edge has been observed to form at  $\sim 1 \text{ ps}$  by two-photon photon emission spectroscopy and is also confirmed by density-of-state calculation.<sup>147, 148</sup> This E\* state might not be created by 1.97 eV (0.32 eV above band edge) photon excitation because of insufficient excess energy. Based on these observations, we attributed the nonequilibrium transport over 10s of picoseconds to hot carriers associated with the energetic E\* state. The E\* state is accompanied by the formation of large polarons occurring on the  $\sim 1 \text{ ps}$  time scale.<sup>147</sup> The long-lived and non-diffusive transport observed is also consistent with the large polaron picture, because the slow decay constant for the diffusion constant agrees well with the slow cooling of hot polarons by acoustic phonon scattering.<sup>148</sup> These polarons are “heavier” than

the bare carriers with non-parabolic dispersion,<sup>100</sup> which could explain a lower diffusion coefficient on the 10s of picosecond time scale.

#### 4.5 Conclusions

To conclude this project, carrier motion visualized by ultrafast microscopy reveals that hot carrier transport in MAPbI<sub>3</sub> is extremely long-range. For carriers with 1.49 eV excess energy, a quasi-ballistic transport length of ~ 280 nm is achieved within 300 fs, which is attributed to slow momentum relaxation processes. This distance exceeds the layer thickness requirement of ~ 200 nm for photon absorbance in solar cells, therefore, hot carries could, in principle, be harvested with minimal thermal loss. Furthermore, we also observe non-equilibrium carrier transport on the tens of ps timescale. Overall hot carriers with 1.5 eV excess energy migrate over a distance of ~ 600 nm before reaching thermal equilibrium with the lattice. Such long-range hot carrier transport is most likely not limited to MAPbI<sub>3</sub> because many hybrid organic-inorganic metal halide perovskites share similar carrier relaxation characteristics. Both the slow hot carrier process and the long-range motion makes hybrid perovskites extremely favorable materials for hot carrier devices.

## **CHAPTER 5. ACCELERATION OF CARRIER TRANSPORT VIA A HOT PHONON BOTTLENECK IN HYBRID LEAD HALIDE PEROVSKITES**

### 5.1 Abstract

Slow cooling of hot carriers resulting from phonon bottleneck has been observed in hybrid organic-inorganic lead halide perovskites, pointing toward the potential to overcome the Shockley-Queisser limit. Open questions remain on whether the high optical phonon density from the bottleneck impedes the transport of these hot carriers. Here we present a direct visualization of hot carrier transport in the phonon bottleneck regime in both single crystalline and polycrystalline lead halide perovskites utilizing ultrafast transient absorption microscopy. Remarkably, hot carrier diffusion does not suffer from but rather is enhanced by the presence of a phonon bottleneck, the exact opposite from what is observed in conventional semiconductors such as GaAs. These results showcase the unique aspects of hot carrier transport in hybrid perovskites and suggest even larger potential for hot carrier devices than previously envisioned.

### 5.2 Introduction

#### 5.2.1 Hot Phonon Bottleneck

In semiconductor materials, absorption of optical photons having higher energy than the bandgap, results in the generation of “hot” energetic carriers. A more detailed description of their generation and characteristics can be found in Chapter 3, Section 3.2. The decay (equilibrium restoration) of hot carriers occurs via thermalization with the lattice by the emission of optical phonons. Phonons, easily thought of as lattice vibrations are the pathway for hot carriers to reach an energetic equilibrium by dissipating heat and energy to the surrounding lattice structure. Optical phonons are higher energy lattice vibrations that consist of out of phase atomic oscillations

within the crystal structure. For example, if one atom moves to the right, the neighboring atom moves to the left. The optical phonons decay into acoustic phonons which are a lower energy lattice vibration in which all movements are coherent (i.e. all atoms moving in a synchronous manner). Hot electrons emit optical phonons on an ultrafast time scale, which has been reported to be between 30 fs<sup>146</sup> and 100 fs<sup>169</sup>. At high pump fluence, there exists high carrier densities, in which all the energetic carriers are emitting phonons on an ultrafast timescale. This leads to a bottleneck effect since the optical phonons that are emitted, cannot decay faster than they are being generated and the excess hot phonon population increases phonon reabsorption. The emission of optical phonons builds up a hot phonon population that can transfer energy back to the electron system. This reduces the net thermalization rate or phonon emission rate (i.e. hot carriers cannot emit optical phonon, thus remains hot for an extended period). This is analogous to thinking about an object trying to cool down in a hot water bath – when the temperature of the bath (surroundings) is hot, then the object will cool down slower compared to a cold bath (cold surroundings). For high carrier concentration, the hot carrier lifetime is increased from ~ 30 fs to 30 - 100 ps.<sup>146</sup> This is advantageous because we have shown in the previous chapter that hot carrier transport is long-range and promising for a hot carrier solar cell. The main flaw to this dream is that hot carriers live for such a short amount of time, and we know that the diffusion length is dependent on carrier lifetime and diffusion coefficient (recall Eq. 1). This is where the hot phonon bottleneck can be used to ultimately extend the hot carrier lifetime.

The defect tolerance of lead halide perovskites translates into long-range carrier transport and slow non-radiative recombination thus achieving high device efficiencies. A unique property of the lead halide perovskites is the extremely slow hot carrier cooling, attributed to suppressed optical phonon scattering by the formation of large polarons.<sup>169, 170</sup> A hot phonon bottleneck

further extends carrier cooling timescales up to hundreds of picoseconds due to the ultralow thermal conductivities of hybrid perovskites.<sup>146, 150, 158, 171-173</sup> Such slow carrier cooling resulted from phonon bottleneck, orders of magnitude slower than conventional semiconductors such as GaAs, suggests the potential of harvesting hot carriers in hybrid perovskites to overcome the Shockley-Queisser limit.<sup>171, 174</sup>

One negative consequence of phonon bottleneck in conventional semiconductors is the decreased carrier mobility as the optical phonon population increases.<sup>175-182</sup> For hot carrier solar cell applications, a fundamental material parameter is how far the hot carriers can travel in the active photovoltaic layer before cooling to thermal equilibrium. Therefore, while phonon bottleneck can prolong carrier-cooling time, the reduced carrier mobility might prevent these carriers from migrating over sufficiently long distance. The understanding of hot carrier transport in the regime of phonon bottleneck remains elusive because it is highly complex involving both relatively short-lived non-equilibrium electron and phonon population. Experimentally, direct measurements are challenging due to the requirement of simultaneously high temporal and spatial resolutions. There have been recent developments in coupling ultrafast spectroscopy with microscopy approaches to achieve the necessary resolutions in imaging nonequilibrium carrier transport.<sup>21, 183-185</sup> We have demonstrated ultrafast transient absorption microscopy (TAM) to directly visualize hot carrier migration with a time resolution of  $\sim 300$  fs and a spatial precision of  $\sim 50$  nm. However, in the initial report,<sup>132</sup> we have only investigated hot carrier transport in low carrier density regime in absence of phonon bottleneck. In this chapter, we focus on the transport of hot carriers as the result of a phonon bottleneck on the timescale of 100s of picoseconds in both model single crystal nanoplates and device relevant polycrystalline lead halide perovskite thin films. Surprisingly, hot carrier transport is enhanced by phonon bottleneck, opposite from what is

known in conventional semiconductors, which we attribute to the suppression of optical phonon scattering. Furthermore, the excess kinetic energy allows these hot carriers to overcome grain boundaries, which is beneficial for device applications.

### 5.3 Material Preparation

#### 5.3.1 Alkali Metal-Doped Thin Film Perovskites

RbCsMAFA thin film: Glass coverslips (0.17 mm thick) were thoroughly cleaned by rubbing the surface of the glass with a wipe and acetone. The substrates were then cleaned for 20 min by UV ozone. The mixed-cation lead mixed-halide perovskite solution was prepared from a precursor solution made of FAI (1 M, Dyenamo),  $\text{PbI}_2$  (1.1 M, TCI), MABr (0.2 M, Dyenamo) and  $\text{PbBr}_2$  (0.22 M, TCI) in a 9:1 (v:v) mixture of anhydrous DMF:DMSO (Sigma Aldrich). A 1.5 M stock solution of CsI (Sigma Aldrich) in DMSO was then added to above solution in 5:95 volume ratio. Similarly, a 1.5 M stock solution of RbI (Sigma Aldrich) in DMF was added to above solution in 5:95 volume ratio. The perovskite solution was deposited through a two-step spin coating program (10 s at 1000 rpm and 20 sec at 6000 rpm) with dripping of chlorobenzene as anti-solvent during the second step, 15 s before finishing the second step. The perovskite layers were annealed at 100°C for 45 min. To achieve similar thermal gradient during the heating step to that of a solar cell prepared on thick FTO glass.

#### 5.3.2 Single Crystal $\text{MAPbI}_3$ Nanoplates

Surface-functionalized single-crystal  $\text{MAPbI}_3$  nanoplates were synthesized by immersing a piece of  $\text{PbAc}_2$  coated glass slide in a mixed solution of MAI and phenethyl ammonium iodide (PEAI) in isopropanol (IPA) at room temperature. The  $\text{PbAc}_2$  thin film was prepared by drop casting 100 mg/mL  $\text{PbAc}_2 \cdot 3\text{H}_2\text{O}$  aqueous solution on a glass slide. The coated substrate was then

annealed at 50 °C in an oven before it was dipped into 1 mL precursor solution in a reaction vial. The precursor solution was made by mixing solutions of PEAI (40 mg/mL) and MAI (40 mg/mL) in IPA with a volume ratio of 0.35/0.65. After some reaction time of ~ 3 days, the glass slide was taken out, and subsequently washed in isopropanol and dried under N<sub>2</sub> flow. To carry out TA and TAM measurements, single-crystal nanoplates are transferred from the growth substrate to a glass coverslip by a dry contact process.

## 5.4 Results and Discussion

### 5.4.1 Observation and Impact of Low-Threshold Hot Phonon Bottleneck

In this study, we investigate two types of samples. One type is single-crystal MAPbI<sub>3</sub> nanoplates, which represents a well-studied model system. The surface of these nanoplates has been functionalized to minimize surface recombination.<sup>186</sup> The other type of sample is a device relevant mixed-cation and mixed-halide lead perovskite with the formula Rb<sub>0.05</sub>(Cs<sub>0.05</sub>((MAPbBr<sub>3</sub>)<sub>0.17</sub>(FAPbI<sub>3</sub>)<sub>0.87</sub>)<sub>0.95</sub>)<sub>0.95</sub> (RbCsMAFA). This compound exhibits a cubic structure<sup>187</sup> and has been demonstrated to be resilient to high temperatures while maintaining power conversion efficiencies over 20%.<sup>47, 188, 189</sup> This temperature stability is promising for future fabrications of hot carrier solar cells. The polycrystalline thin films of RbCsMAFA had a thickness of 400-450 nm and are deposited on glass coverslips (0.17 mm thick) for all the optical measurements described below. An SEM cross sectional image of the sample is shown in Figure 5.1. The bandgap for RbCsMAFA is at 1.65 eV which is easily seen from the absorption and emission spectra (Figure 5.2). This bandgap is comparable to that of well-studied MAPbI<sub>3</sub> (recall Figure 1.4).

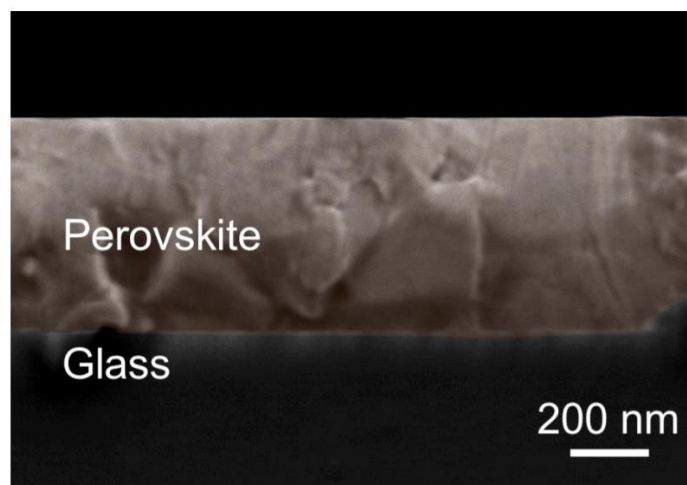


Figure 5.1 A representative scanning electron microscopy image of a RbCsMAFA perovskite thin film deposited on glass substrates used in the optical measurements.

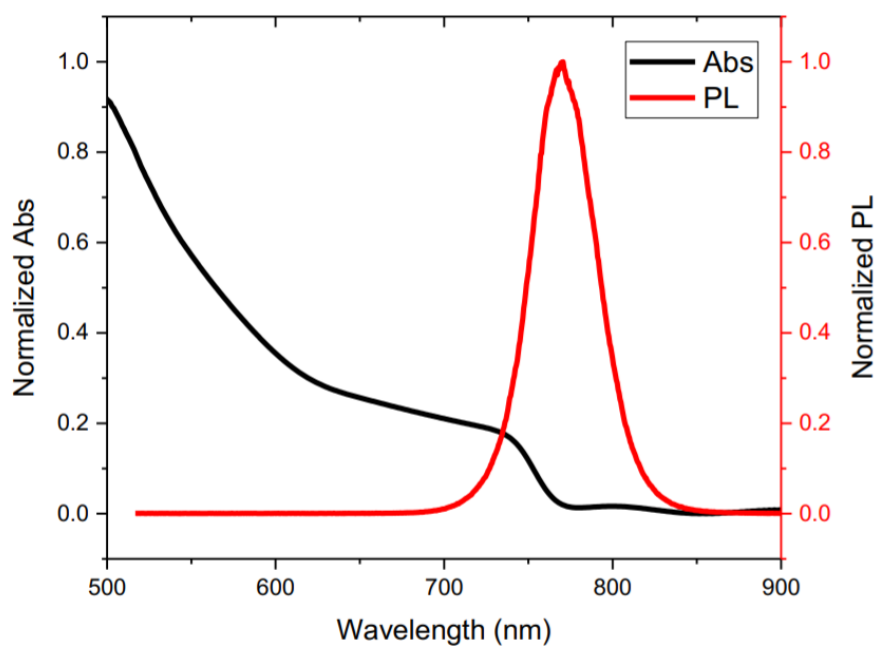


Figure 5.2 Normalized absorption spectrum (black) and photoluminescence spectrum (red) of a RbCsMAFA perovskite thin film.

We first characterize the dynamics of carrier cooling using broadband transient absorption (TA) spectroscopy. At room temperature, photoexcitation leads to the generation of free carriers instead of excitons in hybrid lead halide perovskites due to a high dielectric constant and strong Coulomb screening.<sup>67</sup> Figures 4.3, 4.4, and 4.5 show the excitation energy and carrier density dependent transient absorption spectra and dynamics. Upon photoexcitation, a ground state bleach band (GSB, positive signal in  $\Delta T/T$ , where  $\Delta T$  is pump induced change in probe transmission and  $T$  is the probe transmission) centered around the bandgap at 1.65 eV is observed due to band-filling effect.<sup>151</sup> At high carrier densities and a pump photon energy of 3.10 eV, a high-energy tail of the GSB band is observed up to 100 ps, indicating that carriers remain with excess energy at this timescale (Figure 5.3 (a) and Figure 5.6 (a)). An effective carrier temperature,  $T_c$ , can be used to describe the quasi-equilibrium distribution of carriers established by carrier and phonon scatterings.<sup>190</sup> We obtain  $T_c$  by fitting the high energy tail of (energies  $> E_f$ ) the GSB signal with Maxwell–Boltzmann distribution<sup>191</sup> as given by,  $\frac{\Delta T}{T}(\hbar\omega) = A_0(\hbar\omega)\exp\left(-\frac{\hbar\omega}{k_B T_c}\right)$ , where  $\hbar\omega$  is the probe energy,  $A_0$  is the linear absorbance, and  $k_B$  is the Boltzmann constant.<sup>146, 158</sup>

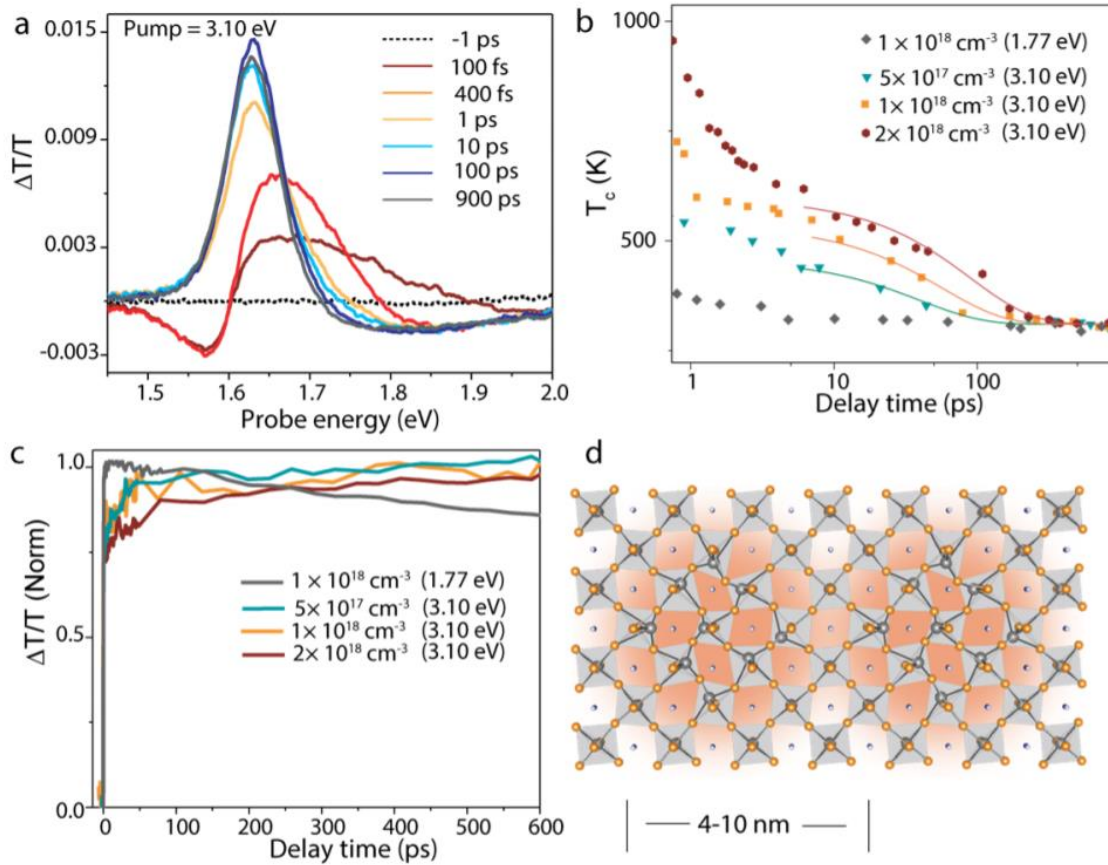


Figure 5.3 (a) TA spectra taken at various delay times with pump photon energy of 3.10 eV at an injected carrier density  $N_0$  of  $1 \times 10^{18} \text{ cm}^{-3}$  in the RbCsMAFA thin film. (b) Symbols are time-dependent carrier temperatures at different pump photon energies and carrier densities as extracted by fitting the high-energy tail of the GSB signal in the RbCsMAFA thin film as described in the text. Solid lines are fitting to  $\tau_c = \tau_0 \left(1 + \frac{\rho}{\rho_c}\right)$  as described in the text. (c) The carrier dynamics probed at the bandgap of 1.65 eV in the RbCsMAFA thin film. (d) Schematic drawing of large polaron formation and overlap of two large polarons.

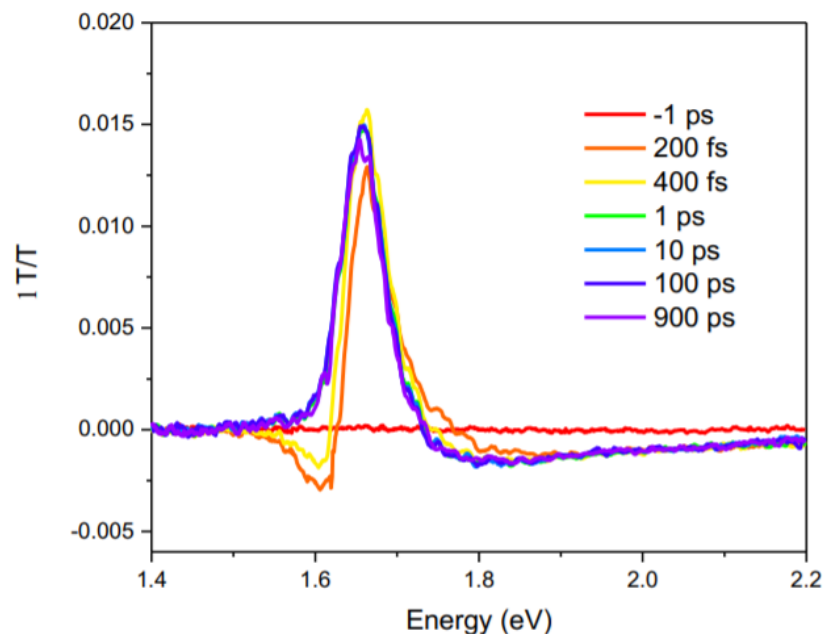


Figure 5.4 TA spectra taken at various delay time with pump photon energy of 2.25 eV and a carrier density of  $10^{18} \text{ cm}^{-3}$  of a RbCsMAFA perovskite thin film.

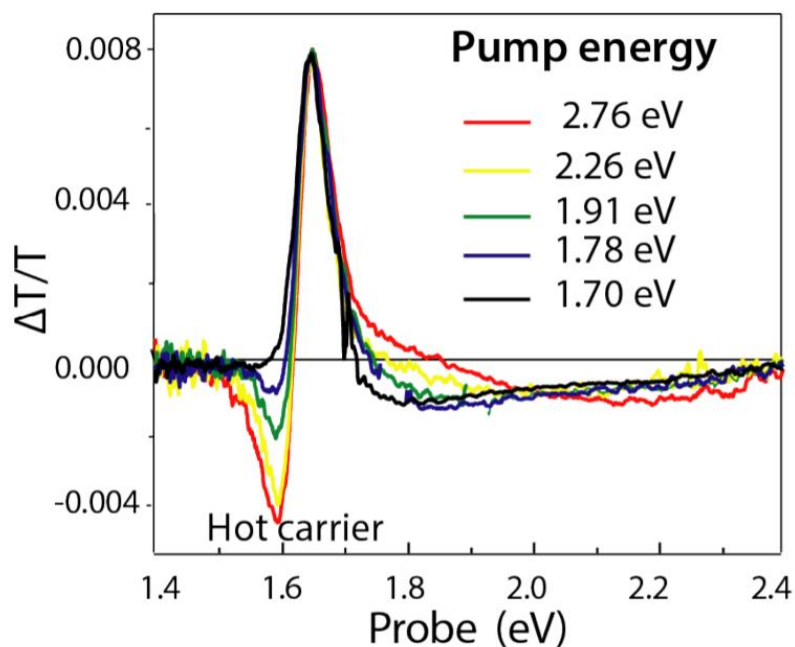


Figure 5.5 Transient absorption spectra of a RbCsMAFA perovskite thin film taken at 200 fs delay with different pump photon energies and change of transmission  $\Delta T/T$  was plotted. The pump fluences were calibrated to the same carrier density of  $10^{18} \text{ cm}^{-3}$ .

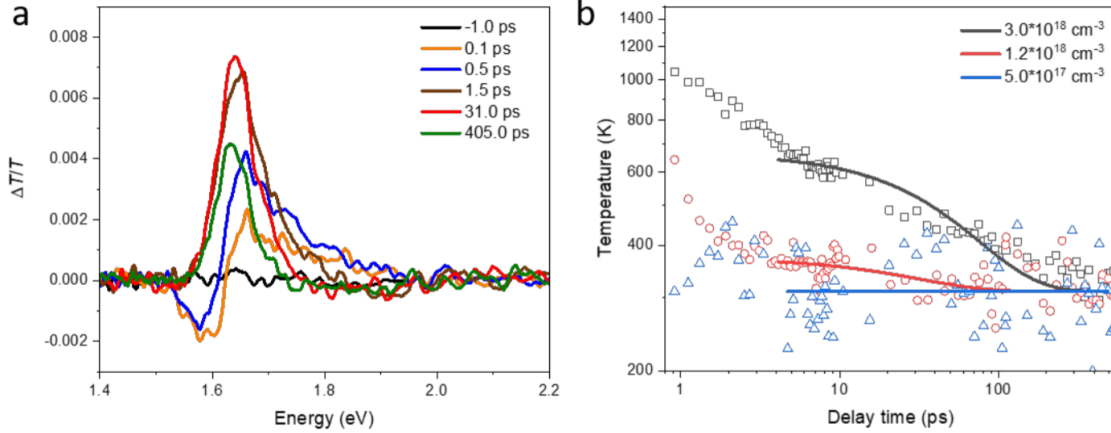


Figure 5.6 (a) TA spectra taken at various delay times with pump photon energy of 3.10 eV at an injected carrier density  $N_0$  of  $1.2 \times 10^{18} \text{ cm}^{-3}$  in the MAPbI<sub>3</sub> single crystal. (b) Symbols are time-dependent carrier temperatures of the MAPbI<sub>3</sub> single crystal at different carrier densities as extracted by fitting the high-energy tail of the GSB signal. Solid lines are fitting to  $\tau_c =$

$$\tau_0 \left( 1 + \frac{\rho}{\rho_c} \right)$$

We plot  $T_c$  as a function of pump-probe delay at different carrier densities in Figure 5.3 (b) for the RbCsMAFA thin film and in Figure 5.6 (b) for the MAPbI<sub>3</sub> single-crystal nanoplate. Overall, a similar behavior of two steps of the carrier cooling is observed for these two samples. The initial cooling step shows a similar lifetime (0.2 – 0.4 ps) under various pump fluences, which are dominated by the polar optical phonon scattering via the Fröhlich mechanism of the bare carriers.<sup>190</sup> The formation of polarons driven by optical phonon scattering has been estimated to occur also on the sub-picosecond timescale.<sup>192, 193</sup> A polaron is a quasiparticle consisting of an electron and the lattice polarization induced in its vicinity (schematically represented in Figure 5.3 (d)), which is responsible for transport in many polar and ionic solids.<sup>194</sup>

A second carrier cooling process (up to 100s of ps) that becomes slower as carrier density increases is observed with a pump photon energy of 3.10 eV (Figure 5.3 (b)), which is consistent with previous reports.<sup>146, 171</sup> The rise-time in the carrier dynamics probed at the bandgap reflecting the time for the carriers to relax from the high-energy states to the band edge (Figure 5.3 (c)) also becomes slower as carrier density increases. The slow cooling process is absent when the pump

photon energy is reduced to 1.77 eV and the carriers reach thermal equilibrium with the lattice in a few ps (Figure 5.3 (b) and (c)). The slower cooling as the carrier density and the excess energy increase can be explained by hot-phonon bottleneck.<sup>146, 150, 158, 172</sup> A phonon bottleneck occurs when the emission of optical phonons builds up a non-equilibrium (hot) phonon population that can transfer energy back to the electron system. The Pb–I–Pb angular distortions optical mode in MAPbI<sub>3</sub> are coupled strongly to the electrons and yet interact weakly with the rest of the phonon bath, which could be the origin for the phonon bottleneck.<sup>172, 195</sup>

The phonon bottleneck threshold of  $N_0 \sim 3 \times 10^{17} \text{ cm}^{-3}$  is observed for the RbCsMAFA thin film and a threshold is  $\sim 10^{18} \text{ cm}^{-3}$  for the MAPbI<sub>3</sub> single-crystal nanoplate. These thresholds are overall consistent with the carrier density at which the large polarons (radii 2-5 nm) are overlapping in space,<sup>169, 196</sup> as schematically shown in Figure 5.3 (d). At high carrier density, the polaron states overlap and cooling slows down because the adjacent polarons share cooling channels.<sup>169</sup> We fit the hot carrier cooling time,  $\tau_c$ , at different carrier densities with a phenomenological model of  $\tau_c = \tau_0 \left(1 + \frac{\rho}{\rho_c}\right)$  where,  $\tau_0$  is the polaron cooling time at the low carrier density limit and in absence of phonon bottleneck,  $\rho$  is carrier density, and  $\rho_c$  is the critical carrier density above which polarons should overlap with each other. A  $\tau_0$  value of  $\sim 24$  ps and  $\sim 14$  ps is obtained for the RbCsMAFA thin film and the MAPbI<sub>3</sub> single crystal, respectively, from the global fitting of data shown in Figure 5.3 (b) and Figure 5.6 (b). The slower cooling in the RbCsMAFA thin film compared to the MAPbI<sub>3</sub> single crystal is likely due to its lower thermal conductivity. Auger heating has also been proposed to contribute to the slow carrier cooling.<sup>173</sup> However, the Auger heating mechanism should also lead to an overall loss of carrier population. From the carrier density-dependent carrier recombination dynamics shown in Figure 5.3 (c), there is no loss of carrier population is observed for different carrier densities when excited at 3.10 eV.

Therefore, we conclude that a hot phonon bottleneck is the dominant mechanism for the slow carrier cooling observed here.

#### 5.4.2 Enhancement of Carrier Transport

To experimentally observe enhancement of carrier transport in the regime of a hot phonon bottleneck, we employ TAM to directly image equilibrium and non-equilibrium carrier transport. The morphology of the sample is homogenous on the length scale of hundreds of nanometers, as demonstrated by the morphological (scanning pump and probe together) TAM image in Figure 5.7. To image carrier transport, the pump beam is held at a fixed position while the probe beam is scanned relative to the pump with a Galvanometer scanner and  $\Delta T$  is plotted as function of probe position to form an image (full details in Chapter 2, Section 2.5). The probe beam photon energy is at 1.65 eV to probe carriers at the bandgap.

The initial population,  $n(x, y, 0) = N \exp\left[-\frac{(x-x_0)^2}{2\sigma(0)_x^2} - \frac{(y-y_0)^2}{2\sigma(0)_y^2}\right]$ , is created by a Gaussian pump beam at position  $(x_0, y_0)$  with a pulse duration of  $\sim 300$  fs,. At later delay times, the TAM images reflect carrier diffusion away from the initial excitation volume. If the carrier transport is diffusive, the time and spatial dependent carrier density is given by,  $\frac{\partial n(x,y,t)}{\partial t} = D \left[ \frac{\partial^2 n(x,y,t)}{\partial x^2} + \frac{\partial^2 n(x,y,t)}{\partial y^2} \right] - \frac{n(x,y,t)}{\tau}$ , where  $n(x, y, t)$  is the carrier population as a function of position and time,  $D$  is the diffusion coefficient assuming isotropic diffusion,  $\tau$  is the carrier lifetime. We note here that both electrons and holes should contribute more or less, equally to the transport due to their similar effective masses.<sup>67, 169</sup> The population follows a Gaussian distribution at any later delay time  $t$  as given by,  $n(x, y, t) = N \exp\left[-\frac{(x-x_0)^2}{2\sigma(t)_x^2} - \frac{(y-y_0)^2}{2\sigma(t)_y^2}\right]$ .

The resulting 2D TAM images are shown in Figure 5.8 (a) for a pump photon energy of 3.10 eV at  $N_0 \sim 3 \times 10^{17} \text{ cm}^{-3}$  for the RbCsMAFA thin film. The TAM profiles shown in Figure 5.8 (a) are fit by two-dimensional Gaussian functions with variances of  $\sigma_{t,x}^2$  and  $\sigma_{t,y}^2$ , where the  $\sigma_{t,x}^2$  and  $\sigma_{t,y}^2$  are the time-dependent variance of the Gaussian profiles along  $x$  and  $y$  axis at delay time  $t$ . The Gaussian fit along one direction is shown in Figure 5.8 (b). Since the carrier transport is isotropic, we reduced the problem to 1D and defined  $\sigma_t^2 = \frac{\sigma_{t,x}^2 + \sigma_{t,y}^2}{2}$ .<sup>132</sup> The diffusion constant  $D$  is then given by,  $D = \frac{\sigma_{t_2}^2 - \sigma_{t_1}^2}{2(t_2 - t_1)}$ .

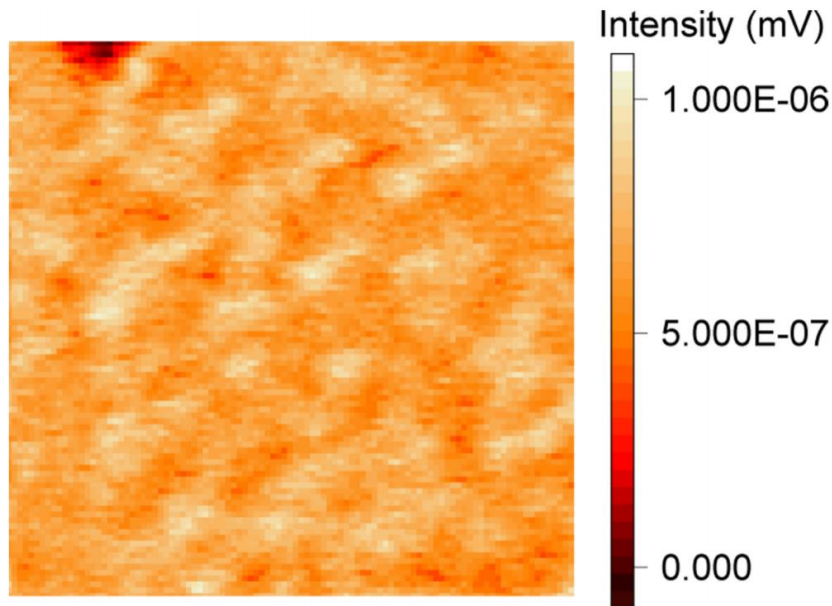


Figure 5.7 Morphological transient absorption microscopy (TAM) image of a RbCsMAFA thin film taken at 0 ps time delay with a pump photon energy of 3.10 eV and a probe photon energy of 1.65 eV. In this mode of TAM imaging, the pump and probe beams are always spatially overlapped and scan simultaneously. The intensity presents the TA signal at each position.

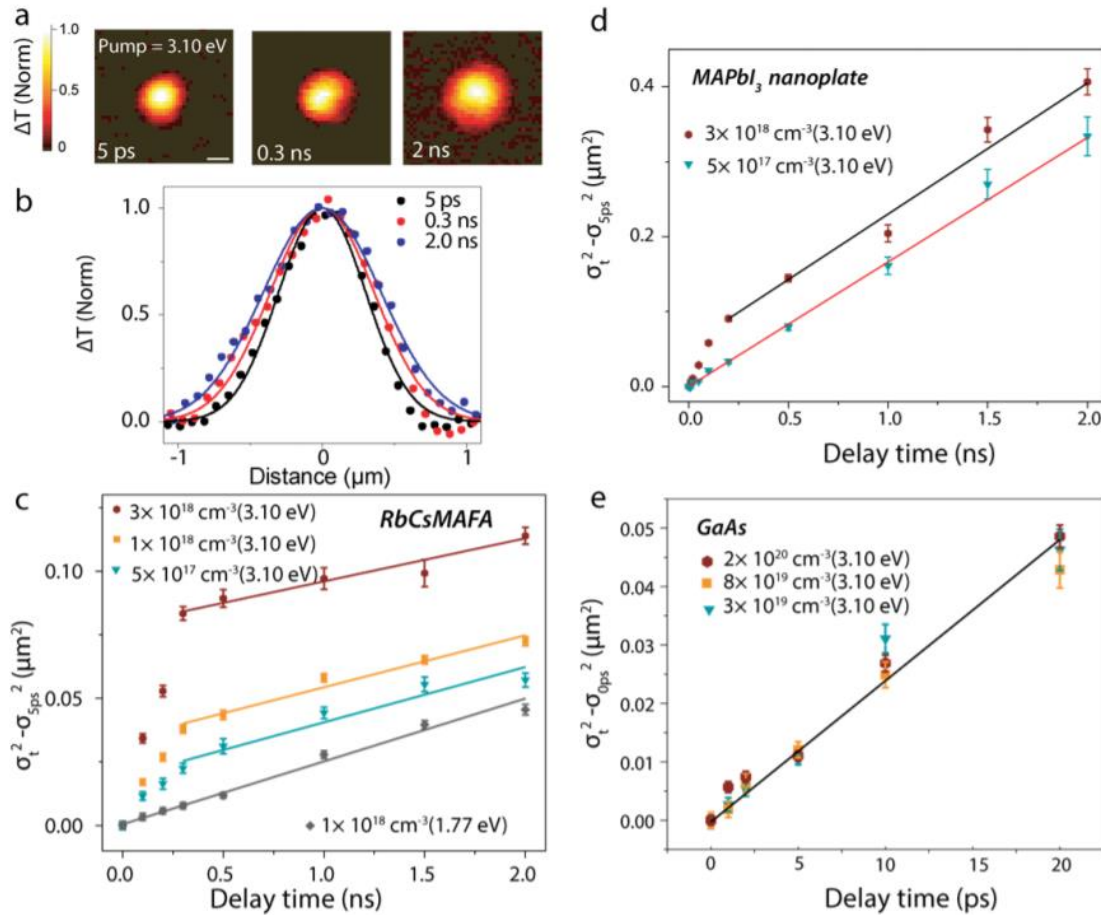


Figure 5.8 (a) The TAM images of the carrier transport at various delay times. Probe energy = 1.65 eV, pump energy = 3.10 eV,  $N_0 = 1 \times 10^{18} \text{ cm}^{-3}$ . Color scale represents the intensity of pump-induced differential transmission ( $\Delta T$ ) of the probe and every image has been normalized by peak value. Scale bar: 500 nm. (b) Cross-sections of the TAM images shown in (a) fitted with Gaussian functions, with the maximum  $\Delta T$  signal normalized. (c)  $\sigma_t^2 - \sigma_{5ps}^2$  plotted as a function of pump-probe delay time of RbCsMAFA at different initial carrier densities and pump energies. Probe energy = 1.65 eV. Solid lines are the linear fits described in the text. (d)  $\sigma_t^2 - \sigma_{5ps}^2$  plotted as a function of pump-probe delay time of a MAPbI<sub>3</sub> single-crystal nanoplate at different initial carrier densities. Probe energy = 1.65 eV. Solid lines are the linear fits described in the text. (e)  $\sigma_t^2 - \sigma_{0ps}^2$  plotted as a function of pump-probe delay time of a GaAs single crystal at different injected carrier densities. Probe energy = 1.45 eV. Solid line is the linear fits described in the text.

Hot carrier transport on the sub-ps timescale in hybrid perovskites is dominated by quasi-ballistic transport of hot bare band carriers as demonstrated in the previous chapter. Here we focus on the transport beyond 5 ps, and particularly on the timescale of 100s of ps, when phonon bottleneck leads to  $T_c$  above the lattice temperature. It is important to rule out higher order effects such as carrier-carrier annihilation in the transport measurements. We have carried out pump intensity dependent dynamics and transport measurements, which is shown in Figure 5.9 (a) and (b) for the RbCsMAFA thin film and MAPbI<sub>3</sub> single crystal, respectively. The carrier dynamics do not change significantly for  $N_0$  ranging from  $5 \times 10^{17} \text{ cm}^{-3}$  to  $3 \times 10^{18} \text{ cm}^{-3}$ , which suggests that annihilation effects are negligible consistent with the results shown in Figure 5.3 (c).

We investigate the effect of a phonon bottleneck on hot carrier transport on the hundreds of picoseconds timescale for the RbCsMAFA thin film and the MAPbI<sub>3</sub> single-crystal nanoplate (Figure 5.8 (c) and (d)). We also image carrier transport in a bulk single crystalline GaAs (100) sample under influence of phonon bottleneck as a comparison, and the results are shown in Figure 5.8 (e). Figure 5.8 (c) and (d) plot  $\sigma_t^2 - \sigma_{5ps}^2$  as a function of the pump-probe delay time at different carrier densities for the RbCsMAFA thin film and the MAPbI<sub>3</sub> single-crystal nanoplate, respectively. As a control, transport of the thermally equilibrated carriers is imaged with a 1.77 eV pump, showing  $\sigma_t^2 - \sigma_{5ps}^2$  increasing linearly as a function of the delay with an equilibrium  $D$  of  $0.12 \pm 0.02 \text{ cm}^2\text{s}^{-1}$  for the RbCsMAFA thin film (Figure 5.8 (c)). When excited with a 3.10 eV pump, equilibrium transport is reached on the ns timescale with a similar  $D$  value of  $\sim 0.1 \text{ cm}^2\text{s}^{-1}$ . The equilibrium diffusion constant for the MAPbI<sub>3</sub> single-crystal nanoplate is  $\sim 0.9 \text{ cm}^2\text{s}^{-1}$ . Equilibrium diffusion constants on the ns timescale are independent of  $N_0$ , consistent with previous a report.<sup>197</sup> More rapid nonequilibrium carrier transport is observed during 5-200 ps when hot phonon bottleneck is present and the carrier temperature is above the lattice temperature for both

the RbCsMAFA thin film and the MAPbI<sub>3</sub> single-crystal nanoplate (Figure 5.8 (c) and (d)). In direct contrast to the results from hybrid perovskites, carrier diffusivity is not enhanced by hot phonon bottleneck in GaAs (Figure 5.8 (e)), despite hot phonon effects have been observed at carrier densities  $>10^{19} \text{ cm}^{-3}$  with carrier cooling time slowing down from sub-picosecond to a few ps.<sup>146, 175</sup> Carrier transport in GaAs does not show time or carrier density dependence for  $N_0$  ranging from  $3 \times 10^{19} \text{ cm}^{-3}$  to  $2 \times 10^{20} \text{ cm}^{-3}$ .

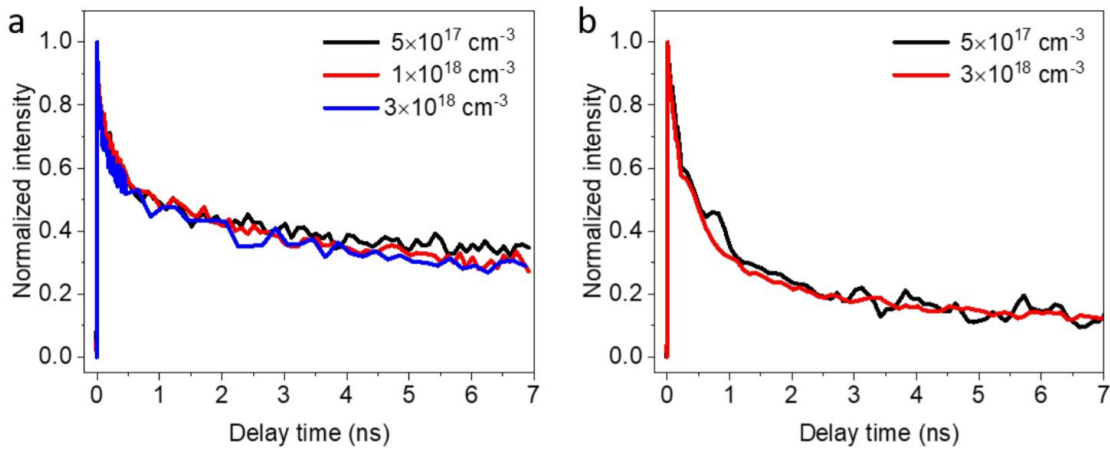


Figure 5.9 Carrier dynamics at different injected carrier densities when pump and probe beams are overlapped in space. (a) RbCsMAFA thin film. (b) MAPbI<sub>3</sub> single crystal. The similar kinetics with  $N_0$  from  $5 \times 10^{17} \text{ cm}^{-3}$  to  $3 \times 10^{18} \text{ cm}^{-3}$  suggest that annihilation effects are negligible for the carrier density range for the RbCsMAFA thin film and the MAPbI<sub>3</sub> single crystal.

The nonequilibrium carrier transport behavior in hybrid perovskites can be clearly seen in Figure 5.10, where the effective diffusion constant is calculated as,  $D = \frac{\sigma_{t_2}^2 - \sigma_{t_1}^2}{2(t_2 - t_1)}$ , for the 3.10 eV excitation. Above the phonon bottleneck threshold,  $D(t)$  increases as  $N_0$  increases during 5-200 ps. For the RbCsMAFA thin film, the diffusion coefficient at 5 ps is  $\sim 1.7 \text{ cm}^2\text{s}^{-1}$  at a  $N_0$  of  $3 \times 10^{18} \text{ cm}^{-3}$  compared to that of  $\sim 0.8 \text{ cm}^2\text{s}^{-1}$  at a  $N_0$  of  $1 \times 10^{18} \text{ cm}^{-3}$  (Figure 5.10 (a)). For the MAPbI<sub>3</sub> single-crystal nanoplate, the diffusion coefficient at 5 ps is  $\sim 3 \text{ cm}^2\text{s}^{-1}$  at a  $N_0$  of  $3 \times 10^{18} \text{ cm}^{-3}$  is

obtained, a factor of 3 larger than the equilibrium  $D$  (Figure 5.10 (b)). When  $N_0$  falls below the phonon bottleneck threshold of  $10^{18} \text{ cm}^{-3}$ , no enhancement in transport is observed for the  $\text{MAPbI}_3$  single-crystal nanoplate over the 100s of ps timescale (Figure 5.8 (d) and Figure 5.10 (b)). Interestingly, while the equilibrium diffusion constant for that of the  $\text{RbCsMAFA}$  thin film is an order of magnitude lower than that of the  $\text{MAPbI}_3$  nanoplate, which is likely due to grain boundaries.<sup>198</sup> The nonequilibrium diffusion coefficient (at 5ps) is on the same order for the two samples, suggesting the excessive kinetic energy of the hot carriers can overcome grain boundaries. The fact that a similar effect is observed in these two different samples demonstrates that the enhanced hot carrier transport is likely a universal phenomenon and not sample dependent.

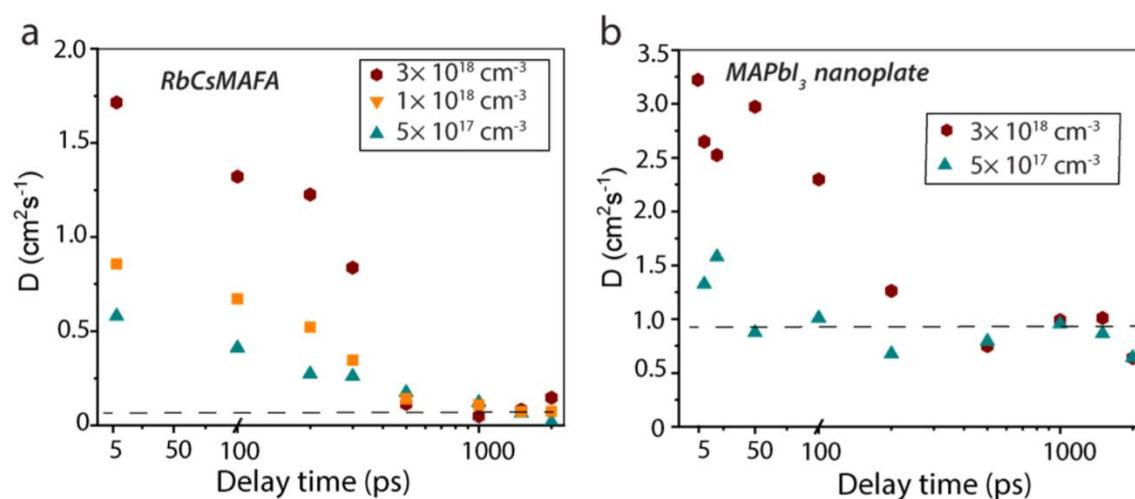


Figure 5.10 The effective diffusion constant for the 3.10 eV excitation for the  $\text{RbCsMAFA}$  thin film (a) and the  $\text{MAPbI}_3$  single crystal (b). The dashed lines denote the equilibrium diffusion constant.

### 5.4.3 Monte Carlo Modeling for Hot Carrier Transport

To understand the accelerated transport in the phonon bottleneck regime, we fit our data using a phenomenological Monte Carlo method that incorporates simultaneous hot carrier cooling and transport. We create hot carriers at 5 ps with their temperature,  $T_c$ , given in the experimental carrier cooling curves (Figure 5.3 (b) and Figure 5.6 (b)) and the spatial probability density distribution is set to be Gaussian. The velocity of the carriers at any given carrier temperature is given by  $\sqrt{\frac{3k_b T_c}{m^*}}$ , where  $m^*$  is the effective mass. The travel direction of the hot carriers is randomized at each step by scattering events<sup>185, 199</sup> as schematically shown in Figure 5.11 (a). The scattering sources include phonons, defects, and impurities. The duration between two collisions is known as momentum relaxation time,  $\tau_s$ .

We fit the data from the MAPbI<sub>3</sub> single crystal nanoplate to avoid the complications from the grain boundaries. The simulated carrier density maps at different delay times are shown in Figure 5.11 (b). The experimental and simulated  $\sigma_t^2 - \sigma_{5ps}^2$  are plotted in Figure 5.11 (c) for the MAPbI<sub>3</sub> single crystal nanoplate at two different carrier densities. We obtain  $\frac{\tau_s}{m^*}$  as a function of temperature by simultaneously fitting the experimental results at the two different carrier densities and plot it in Figure 5.11 (d).  $\frac{\tau_s}{m^*}$  increases from  $\sim 15$  fs/ $m_0$  at 310 K to  $\sim 45$  fs/ $m_0$  at 650 K for the nanoplate, where  $m_0$  is the free electron mass. In other words, Figure 5.11 (d) suggests that the accelerated transport of hot carriers in the hybrid perovskites is the result of not only the larger  $v$  at higher  $T_c$ , but also the longer  $\tau_s$  between the scattering events (assuming  $m^*$  does not change as function of temperature). The mean free path, which is equal to the product of  $v$  and  $\tau_s$ , is also enhanced. These results suggest enhanced hot carrier mobility in the phonon bottleneck regime, as the mobility is given by  $\mu = \frac{e \tau_s}{m^*}$ . We note that recent THz measurements suggest reduced

photoconductivity of hot carriers.<sup>193</sup> However, the THz experiments measuring how carries accelerated by an applied field that is likely insensitive to the hot carrier transport measured here because the hot carriers are already with high velocity and less likely be accelerated due to velocity saturation.<sup>140</sup>

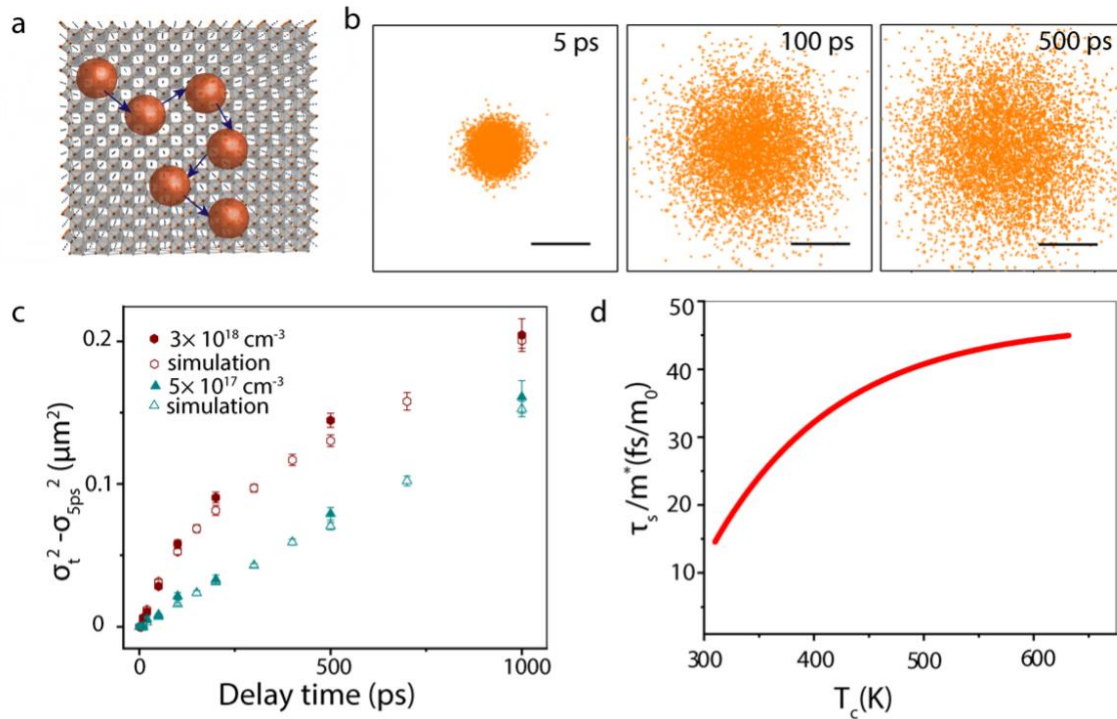


Figure 5.11 (a) Schematic showing the scattering process (b) Simulated 2D maps of 5000 carriers at time delay of 5 ps (left), 100 ps (middle), 500 ps (right). The scale bar is  $0.5 \mu\text{m}$ . (c) Time evolution of the simulated (open) and experimental (solid) spatial profile with  $N_0$  of  $3 \times 10^{18} \text{ cm}^{-3}$  and  $5 \times 10^{17} \text{ cm}^{-3}$  respectively. (d)  $\frac{\tau_s}{m^*}$  as a function of temperature extracted from the simulations shown in (c).

The result shown in Figure 5.11 (d) is striking because it goes against the well-established knowledge in conventional semiconductors, where  $\tau_s$  decreases as the density of optical phonons increases leading to saturation of carrier mobility.<sup>175, 176</sup> One possible explanation for the seemingly puzzling behavior of longer  $\tau_s$  at higher temperature is the reduced optical phonon scattering of large polarons at high temperature.<sup>200</sup> Instead of bare band carriers, large polarons are the dominant species on timescales longer than 1 ps in lead halide perovskites.<sup>169, 196</sup> Since the polaron size,  $L$  (4-10 nm), is much larger than the lattice constant, optical phonons serve as a static scattering centers whose active range is given by the size of the polarons.<sup>200</sup> The scattering probability from the optical phonons  $\left(\frac{1}{\tau_{op}}\right)$  decreases exponentially when the wave vector of the polaron,  $\frac{p}{\hbar}$  ( $p$  is the momentum), exceeds  $(1/L)$ ,  $\frac{1}{\tau_{op}} \propto e^{-\left(\frac{2\pi|p|}{\hbar L}\right)}$ .<sup>200</sup> Also, the scattering frequency is proportional to the population of optical phonons,  $\frac{1}{\tau_{op}} \propto \frac{1}{\frac{\hbar\omega}{e^{k_B T}-1}}$ , where  $\omega$  is the optical phonon frequency.<sup>200</sup> Therefore, the temperature dependence of  $\tau_s$  and the mobility of hot carriers is a competition between (1) the optical phonon population that increases with rising temperature and (2) the frequency of optical phonon scattering that falls with increasing temperature. At high temperature, the increase of the wave vector of the polaron,  $\frac{p}{\hbar}$ , outweighs the optical phonon population growth, leading to  $\tau_{op} \propto e^{\left(\frac{\pi^2 T}{T_0}\right)}$  ( $T \gg T_0$ , where  $T_0$  is the temperature at which a large polaron's deBroglie wavelength  $\left(\frac{\hbar}{p}\right)$  equals its length  $L$ ).<sup>200</sup>

By fitting the temperature dependent  $\tau_s$  (assuming  $m^*$  is temperature independent) in Figure 5.11 (d) with a function of  $\frac{1}{\tau_s} = \frac{1}{\tau_{op} \cdot e^{\left(\frac{\pi^2 T}{T_0}\right)}} + \frac{1}{\tau_{s0}}$ , where  $\tau_{s0}$  represents the time of all temperature-independent scattering processes, and  $T_0$  is estimated to be  $\sim 450$  K. This value is

about a factor of 6 larger than the value determined from  $L$  of (4-10) nm and  $m^* = 0.5 m_0$ .<sup>133</sup> Such discrepancy might result from the non-classical large polarons formation in hybrid perovskites due to the anharmonic and dynamically disordered atomic motions.<sup>201, 202</sup> It is also possible that a high carrier density could destabilize the polaron formation, leading to a decreased  $m^*$ , which could be true as carrier density increases. However, because the same  $\frac{\tau_s}{m^*}$  curve fits the results from both  $N_0 = 3 \times 10^{18} \text{ cm}^{-3}$  and  $N_0 = 5 \times 10^{17} \text{ cm}^{-3}$  well, indicating that  $m^*$  does not change significantly in the carrier density range for our measurements.

Another possible mechanism for the electron mobility to be enhanced is through so-called hot phonon drag. Hot phonon drag occurs when there is an underpopulation of phonons with negative wavevector and an overpopulation of phonons with positive wavevector. This asymmetry of optical phonon occupation in the momentum space can lead to the gain of directed momentum leading to the enhancement of the carrier velocity.<sup>203</sup> Despite enhanced electron mobility by hot phonon drag being predicted theoretically for GaAs/AlAs quantum wires at high temperature,<sup>203</sup> this effect has not been verified experimentally.

The enhanced hot carrier transport by phonon bottleneck in the champion solar cell RbCsMAFA polycrystalline thin films suggests potential for practical applications. For feasible hot carrier solar cells, lowering phonon bottleneck threshold close to the one sun equivalent illumination ( $N_0 \sim 10^{16} \text{ cm}^{-3}$ ) is desirable. One very attractive property of hybrid lead halide perovskites is that the hot phonon effect can be potentially modulated by adjusting both the metal halide framework and the intercalated A site cation.<sup>165, 204</sup> Recent theoretical calculations predict that the A site cation can be tuned to slow down electron-phonon scattering as well as to modulate optical-acoustic phonon scattering.<sup>205</sup> The fact that the RbCsMAFA thin film has a lower

phonon bottleneck threshold than the MAPbI<sub>3</sub> single crystal nanoplate suggest that structural tuning of mixed ion halide perovskites can potentially lower the phonon bottleneck threshold.

## 5.5 Conclusions

We have directly visualized hot carrier transport under the influence of a hot phonon bottleneck in lead halide perovskites by ultrafast pump-probe microscopy with ~ 300 fs temporal resolution and ~ 50 nm spatial precision. In striking contrast to conventional semiconductors, hot carrier transport is not impeded by the increased optical phonon density resulting from the bottleneck created by optical phonons, which we attribute to the reduced scattering frequency in the high temperature regime of large polarons. The accelerated hot carrier transport is universal in lead halide perovskites, observed in both prototypical single crystals and device relevant polycrystalline thin films. These results add crucial details to the phonon bottleneck effect in hybrid perovskites, suggesting hybrid perovskites are even more attractive for hot carrier photovoltaic applications than previously thought. The potential for adding a solar concentrator on a perovskite thin film solar cell can increase the power density and ultimately create a phonon bottleneck, which was shown in this work to accelerate carrier transport on longer time scales than the initially photogenerated hot carriers.

## CHAPTER 6. COLLABORATIVE WORK ON ALLOYED PEROVSKITE THIN FILMS AND HYBRID QUANTUM WELL PEROVSKITES

### 6.1 Homogenization of Carrier Dynamics in Alloyed Perovskite Thin Films

#### 6.1.1 Abstract

Perovskite solar cells have shown remarkable efficiencies beyond 21%, through organic and inorganic cation alloying. However, the role the inorganic cations plays is not well-understood. By using transient absorption microscopy, we show that alkali metals  $\text{Rb}^+$  and  $\text{Cs}^+$  are responsible for inducing a more homogenous halide ( $\text{I}^-$  and  $\text{Br}^-$ ) distribution, despite the partial incorporation into the perovskite lattice. This translates to improved electronic dynamics, including lifetimes above 3  $\mu\text{s}$  and homogenous carrier dynamics, as well as improved photovoltaic device performance. We find that Cs cations tend to distribute homogeneously across the perovskite film, while Rb and K cations tend to phase segregate at precursor concentrations as low as 1%. These precipitates have a counter-productive effect on the solar cell, acting as recombination centers in the device, which are easily detectable via transient absorption microscopy. Remarkably, the high concentration of Rb and Cs agglomerations do not affect the open-circuit voltage, average lifetimes and photoluminescence distribution, which is a further indication of the perovskite's notorious defect tolerance.

#### 6.1.2 Introduction

##### 6.1.2.1 Incorporation of Alkali Metal Cations

Emerging solar cell technologies based on thin films and simple deposition methods show promise in reducing production cost and producing high-quality semiconductors for photovoltaic applications.<sup>206, 207</sup> Lead halide perovskite solar cells have emerged as an exciting candidate. In

just a few years, PSCs have achieved power conversion efficiencies similar to established cadmium telluride (CdTe) solar cells, achieving 22.7% in 2017.<sup>208</sup> Perovskites have an  $ABX_3$  formula that is typically comprised of a monovalent cation in the A site. Thus far, we have covered studies primarily involving methylammonium ( $CH_3NH_3^+$ ) as the A site cation. However, this work will incorporate alkali metals cations (rubidium, cesium and potassium) into the A site of the crystal structure. Additionally, an organic molecule like methylammonium (MA) has been used in perovskite fabrication, known as formamidinium (FA).<sup>42, 51, 209-211</sup> The highest reported efficiencies have been achieved with perovskites with mixed MA and FA located in the A-site cations, and Br and I X-site anions.<sup>93, 212, 213</sup> More recently, Cs has been used as the A-site cation to explore more complex compositions, including Cs and MA, Cs and FA, and Cs, MA, and FA – all mixed together.<sup>93, 209, 210, 214-216</sup> Similarly, Rb has been added into a multication perovskite, showing improved efficiency<sup>188, 217</sup> and long-term device stability at elevated temperatures of 85°C.<sup>217</sup> Rb has been suggested to increase charge carrier lifetime and mobility of the perovskite films, which help explain the improved device performance.<sup>218</sup> More recently, K was also used to improve the stabilized PCE of PSCs. These monovalent alkali metals have shown great promise to improve efficiency and stability of PSCs.

Despite these impressive and promising results, the mechanisms that form the basis for improved electronic properties, performance, and stability, upon addition of alkali metals, are not well-understood. Previous studies have hinted at the suppression of low-dimensional wide-bandgap polymorphs, which may act as recombination-active sites.<sup>215, 217, 218</sup> The structural, elemental, and electronic properties of these multi-A-site cation compounds, as well as solar cell performance metrics, have been investigated by bulk techniques<sup>210, 214, 215, 217, 219</sup> averaged over large areas (0.2 to 1 cm<sup>2</sup>), limiting our understanding of these complex material systems. A major flaw in this

approach is that minority-phase formation and elemental agglomeration at the nanoscale is often overlooked. Therefore, there is a need to use spatially-resolved techniques that allow us to image elemental distribution and its impact on electronic properties, and device performance.

In this work, we employ mapping techniques with nanoscale resolution to elucidate the elemental distribution of the alkali metals and their relationship to electronic properties and device performance. We use synchrotron-based X-ray fluorescence imaging to identify elemental distribution in multi ion perovskites. This will allow for high resolution determination of elemental aggregation which has been shown to act as recombination sites.<sup>215, 217, 218</sup> We find that in films where alkali metals are added, the halide distribution becomes homogeneous. Transient absorption spectroscopy mapping shows that perovskite films without alkali-metal iodides (and with segregated halides) suffer from more heterogeneity in the charge carrier dynamics than the those with CsI and/or RbI. By spatially mapping the pump-probe signal as a function of time, we can easily identify areas of charge carrier recombination, as well as identify whether the material is homogenous or heterogenous with respect to charge carrier recombination. At the same time, rubidium and potassium are shown to segregate into large clusters. As the alkali metal additives exceed 1%, we observe second-phase alkali-metal-rich aggregates, which induce charge-carrier recombination at Rb-rich clusters. Charge collection is hindered by these aggregates, and the formation of these alkali-rich nanoprecipitates should therefore be avoided. Our findings are crucial to the understanding of the mechanisms that make these mixed-cation perovskite materials the most efficient for solar cell applications and give insights as to how the photovoltaic community should continue to improve these materials.

### 6.1.3 Material Preparation

The patterned-F-doped SnO<sub>2</sub> (FTO, Pilkington, TEC8) substrates were cleaned by sonicating sequentially in 2% Hellmanex detergent in water, ethyl alcohol and acetone. A dense electron selective layer of TiO<sub>2</sub> (bl-TiO<sub>2</sub>, ~50 nm in thickness) was deposited onto a cleaned substrate by spray pyrolysis, using a 20 mM titanium diisopropoxide bis(acetylacetonate) solution (Aldrich) at 450°C. A mesoporous TiO<sub>2</sub> (meso-TiO<sub>2</sub>, Dyesol particle size: about 30 nm, crystalline phase: anatase) film was spin-coated onto the bl-TiO<sub>2</sub>/FTO substrate using a diluted TiO<sub>2</sub> paste (5:3 paste:ethanol), followed by calcining at 500°C for 1 h in air to remove organic components.

The perovskite films were deposited from a precursor solution containing FAI (1 M, Dyesol), PbI<sub>2</sub> (1.1 M, TCI Chemicals), MABr (0.2 M, Dyesol) and PbBr<sub>2</sub> (0.22 M, TCI Chemicals) in anhydrous DMF:DMSO 9:1 (v:v, Acros). The alkali-metal iodides were added as CsI, RbI, and KI, in molar ratios of the alkali-metal to lead, ranging from 1% to 10%, as these are widely reported concentrations in the literature. The perovskite solution was spin-coated in a two-step program; first at 1000 for 10 s and then at 6000 rpm for 30 s. During the second step, 200 µL of chlorobenzene were poured on the spinning substrate 15 s prior the end of the program. The substrates were then annealed at 100 °C for 1 h in a nitrogen filled glove box.

The spiro-OMeTAD (Merck) solution (70 mM in chlorobenzene) was spun at 4000 rpm for 20 s. The spiro-OMeTAD was doped at a molar ratio of 0.5, 0.03 and 3.3 with bis(trifluoromethylsulfonyl)imide lithium salt (Li-TFSI, Sigma Aldrich), tris(2-(1H-pyrazol-1-yl)-4-tert-butylpyridine)-cobalt(III) tris(bis(trifluoromethylsulfonyl)imide) (FK209, Dyenamo) and 4-tert-Butylpyridine (TBP, Sigma Aldrich), respectively. Finally, a 100 nm Au top electrode was deposited by thermal evaporation. The active area of this electrode was fixed at 0.16 cm.<sup>220</sup>

## 6.1.4 Material Characterization

### 6.1.4.1 Transient Absorption Microscopy

The transient absorption images and dynamics were acquired by a home-built, femtosecond transient absorption spectroscopy setup, which is described in depth in Chapter 2. To construct the images that accentuate recombination sites, we plot the difference between transient bleach signal at time zero (0 ns time delay,  $\Delta T_0$ ) and the transient bleach signal after a 5 ns time delay ( $\Delta T_5$ ). This method compares the signal arising from the initially generated carriers at time zero to the intensity of the signal at a longer time delay between pump and probe. Intuitively, the difference between time zero signal and later signal should be normalized to the initially generated signal, given by:  $\frac{\Delta T_0 - \Delta T_5}{\Delta T_0}$ , which would result in depiction of areas that serve as recombination sites.

## 6.1.5 Results and Discussion

### 6.1.5.1 Interplay Between Halide Distribution and Homogenization of Carrier Dynamics

We investigated the effects of alkali metal addition to the pervasive  $(\text{MAPbBr}_3)_{0.17}(\text{FAPbI}_3)_{0.83}$  perovskite.<sup>93, 212</sup> CsI, RbI, and KI were added to the perovskite solution, at different molar percentages ranging from 1 to 5%. Perovskite thin films were prepared with the combinations X-I/Br, where X is the alkali metal added, and I/Br refers to the  $(\text{MAPbBr}_3)_{0.17}(\text{FAPbI}_3)_{0.83}$ , in solution, similar to the composition previously studied by Saliba *et al.*<sup>217</sup> The most studied perovskites in this work contain 5% CsI, 5% RbI, 5% CsI and 5% RbI, and 5% KI, which are referred to as Cs-I/Br, Rb-I/Br, CsRb-I/Br, and K-I/Br. Solar cells were made with these perovskites in a glass/fluorine-doped tin oxide (FTO)/compact  $\text{TiO}_2$ /mesoporous  $\text{TiO}_2$ /perovskite/spiro-OMeTAD/Au architecture. A schematic of the device cross-section is presented in Figure 6.1.1 A. A transmission electron microscopy (TEM) cross-sectional image is

presented for a device with I/Br (Figure 6.1.1 B) perovskite. Regardless of composition, the perovskite layers are all around 500 nm thick, as expected.<sup>217</sup>

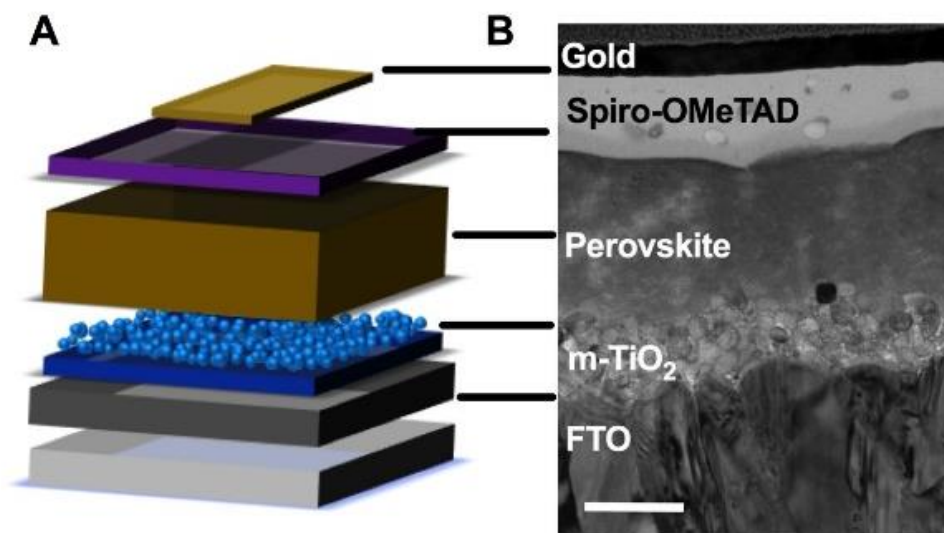


Figure 6.1.1 (A) Schematic of the perovskite solar cells studied, accompanied by (B) the cross-sectional TEM for CsRb-I/Br device.

The device power conversion efficiency was measured for a variety of alkali metal doped perovskites and compared to the ratio of precursors used, as shown in Figure 6.1.2. The precursor ratios are defined as over-stoichiometric, stoichiometric, and under-stoichiometric, which correspond to a PbX<sub>2</sub>:AX of 1.1:1.0, 1.0:1.0, and 0.9:1.0, respectively. From Figure 6.1.2, we can clearly see that an over-stoichiometric precursor for the RbCs-I/Br leads to the highest device performance, measuring in as high as 19%. Overall, with an over-stoichiometric precursor ratio, the addition of Cs and Rb cations corresponds to higher device performance with poor performance when the smaller K cation is added. These results are consistent with the PL lifetimes observed in Figure 6.1.3, where we see a slow decay as Rb and Cs are added to the perovskite and the slowest decay once Rb and Cs are added. The under-stoichiometric samples behave totally different. The poorly performing devices can be the result of a low fill factor which directly translates to a low

power conversion efficiency. This has been ascribed to the formation of a thick organic layer at the surface of the perovskite crystal which inhibits charge transfer from the perovskite to the charge selective contacts.<sup>128</sup>

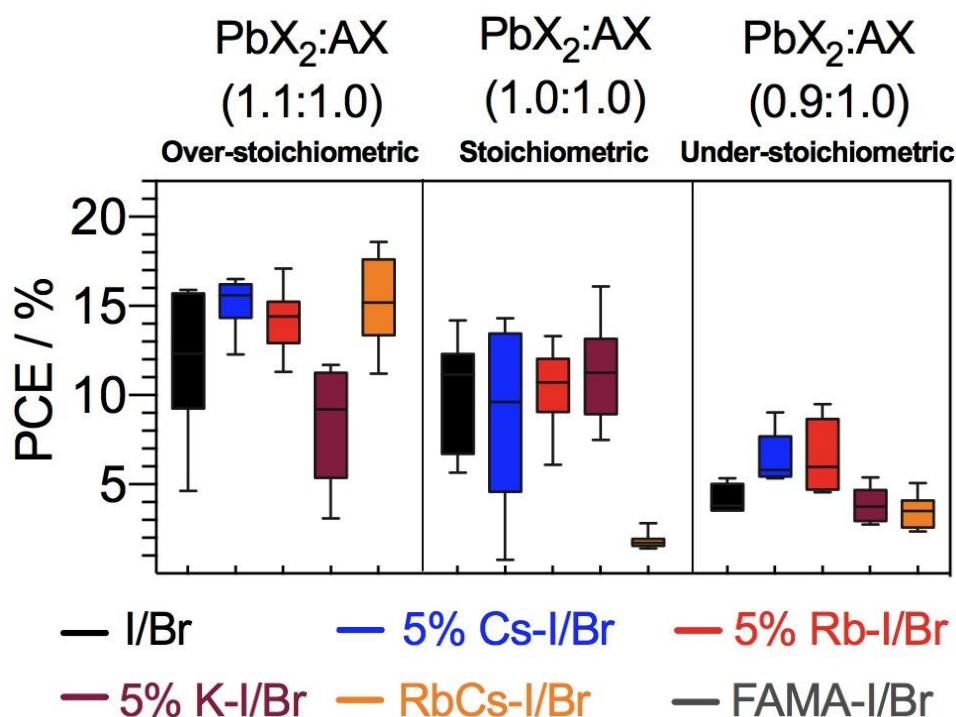


Figure 6.1.2 Device power conversion efficiency for various alkali metal perovskites at different stoichiometric ratios of PbX<sub>2</sub>:AX.

The halide distribution in mixed halide systems has been shown to be of great importance for optoelectronic properties and perovskite device performance.<sup>46, 221, 222</sup> Hoke et al. show that in mixed halide (I and Br) perovskites with high Br content, the thin films exhibit multiple emission peaks, suggesting segregation of the halides.<sup>46</sup> This prompted the investigation of how the halide distribution influences carrier dynamics, which will ultimately be related to the device performance. Interestingly, there is limited benefits to added Rb and Cs individually, whereas the incorporation of Rb and Cs together has been shown to improve device efficiency<sup>47</sup> and this material exhibits a low-threshold hot phonon bottleneck which was covered in Chapter 4.

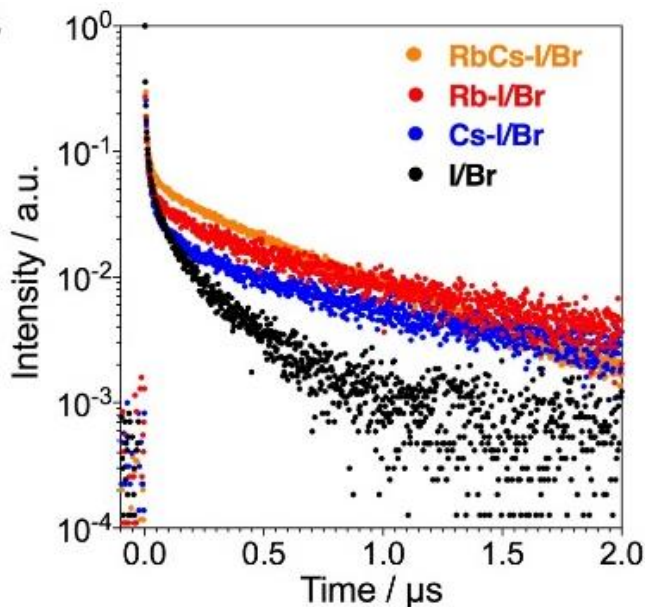


Figure 6.1.3 Time-resolved photoluminescence decay for various alkali metal doped perovskite compositions

To investigate the spatial distribution of ions of these complex mixed perovskite thin films, we can look at images from a synchrotron-based X-ray fluorescence (XRF), shown in Figure 6.1.4. Upon addition of RbI and/or CsI, we observe a homogenization in the distribution of Br. The XRF maps reveal the variation of bromine distribution across samples. The I/Br perovskite, which contains no alkali metal ions, shows clusters of Br that span several microns in size (Figure 6.1.4 A), which corresponds to a heterogeneous carrier dynamic distribution, as seen in Figure 6.1.4 E. Upon addition of Rb and Cs ions, the Br distribution becomes exceptionally homogeneous for the RbCs-I/Br sample (Figure 6.1.4 D), compared to the limited homogenization observed with Cs or Rb alone (Figure 6.1.4 B and C, respectively). To understand the effects of halide segregation on the short time scale carrier recombination dynamics of the perovskite films, we mapped spatial-dependent dynamics by probing the ground state bleach signal at the bandgap, where the relative change in TA signal  $\left(\frac{\Delta T_0 - \Delta T_5}{\Delta T_0}\right)$  is plotted. The TAM images of the samples in which Cs and/or Rb are added show a uniform distribution of transient intensity. The TA intensity maps will accentuate

recombination sites. Thus, it is clear to see how recombination sites, which are associated with halide aggregation, are limited once alkali metals are added to the perovskite (Figure 6.1.4 F, G, and H). This is in agreement with the results from the XRF images in Figure 6.1.4 A-D.

The darker regions in the TA intensity maps represent a larger relative change and hence a faster carrier recombination in the very short-time scale up to 6 ns. Importantly, the contrast in the TAM images reflects the spatial heterogeneity in carrier recombination dynamics. The different areas of halide aggregation may alter the carrier dynamics of the materials. In comparison, carrier dynamics in samples containing alkali-metal iodides are shown to be much more spatially homogeneous. This confirms that the halide aggregation in I/Br samples can be dispersed upon the addition of alkali metals, resulting in a more homogeneous halide distribution and uniform carrier dynamics. The faster decay upon addition of alkali-metal iodides may be due to increased disorder in the crystal structure, which in turn has been shown to change the transient absorption dynamics of perovskites.<sup>223</sup>

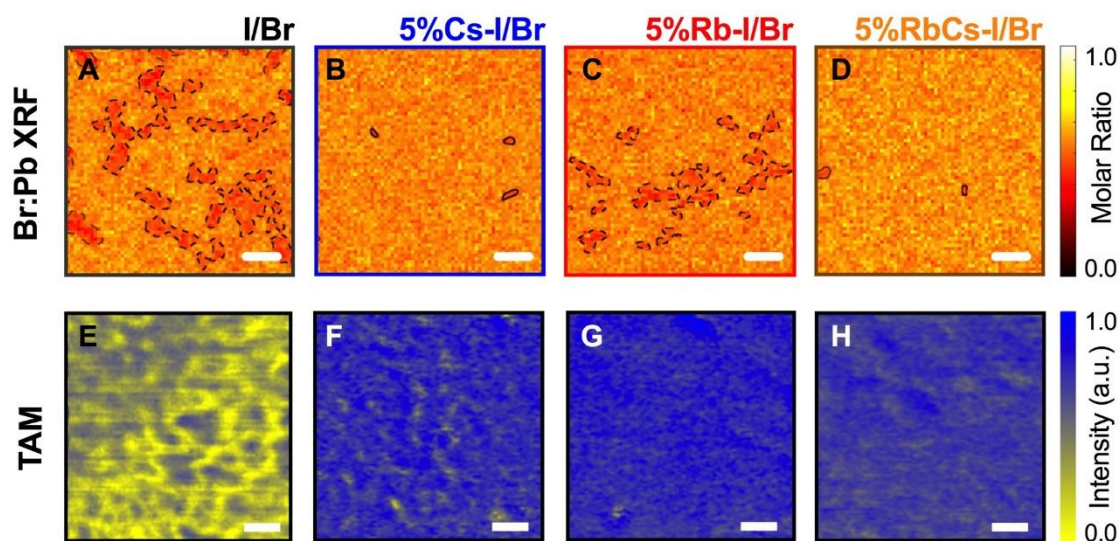


Figure 6.1.4 (A-D) halide distribution by X-ray fluorescence imaging, indicating homogenous distribution of Br upon alkali metal incorporation. Br-poor areas have been marked. (E-H) Transient absorption microscopy images of the relative change in TA signal  $[\Delta T(0 \text{ ps}) - \Delta T(5 \text{ ns})] / \Delta T(0 \text{ ps})$ , mapped as function of sample location. The pump wavelength is at 700 nm with a pump fluence of  $10 \mu\text{J}/\text{cm}^{-2}$ . All scale bars are  $1 \mu\text{m}$ .

To further exemplify the impact the addition of alkali metals has on carrier dynamics, an imaginary line can be drawn across the TAM images that are shown in Figure 6.1.4 and the distribution of the relative change in TA signal can be plotted (Figure 6.1.5). Here, we can clearly see that the overall spread/distribution of the relative change in TA signal is large for the sample that does not contain alkali metals (I/Br). This corresponds to a heterogenous distribution in carrier dynamics, which is alleviated when Rb/Cs is added to the perovskite. The variations in signal of the TA maps is also seen from Figure 6.1.6, where we selected points from the maps of Figure 6.1.4 E to H and plot the carrier dynamics from the respective points. The I/Br sample shows a large range of TA dynamics ranging from short- to long-lived decays, whereas samples with added CsI and/or RbI show much narrower distribution, as expected from the maps in Figure 6.1.4 E to H. TA distributions provide evidence of reduced elemental and electronic heterogeneity in samples with alkali-metal ion incorporation.

Solar cell results shown in Figure 6.1.2 for all these compositions shows that fill factor is the parameter most affected by the incorporation of alkali cations. It is possible that local Br segregation can slow charge carrier extraction. This could happen due to different bandgaps forming locally and preventing charge extraction due to misaligned bands,<sup>224, 225</sup> and/or due to different mobilities for the different compositions.<sup>81</sup> Br-rich perovskite devices have been shown to exhibit multiple bandgaps and low performance metrics.<sup>222</sup>

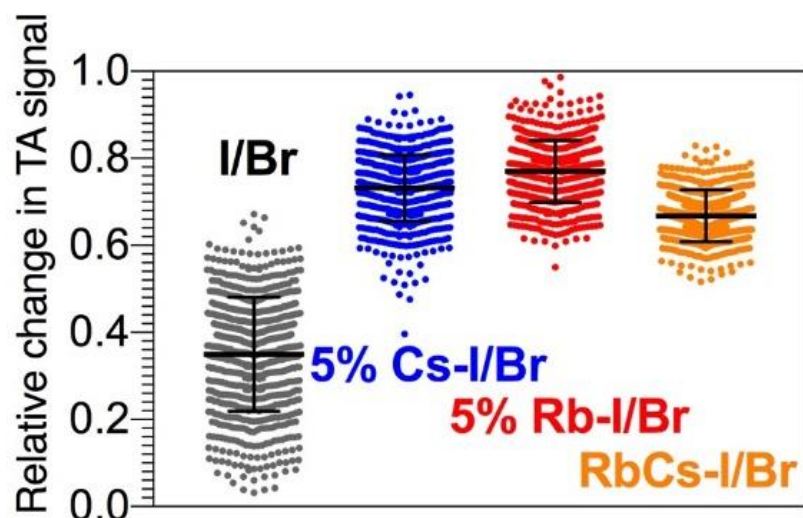


Figure 6.1.5 The relative change of TA signal in samples with different alkali ion additions. Distribution is taken from a line of data points off of the maps shown in Figure 6.1.4 E-H.

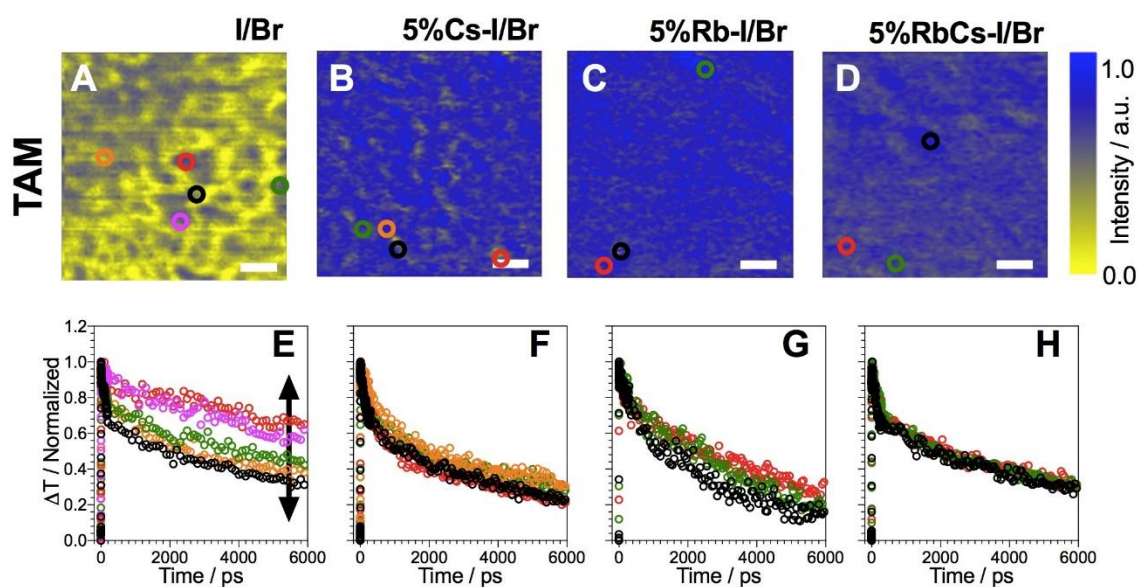


Figure 6.1.6 Charge carrier dynamics as measured by TAM. (A-D), the relative change in TA signal  $[\Delta T(0 \text{ ps}) - \Delta T(5 \text{ ns})] / \Delta T(0 \text{ ps})$  is mapped as function of sample location. The pump wavelength is at 700 nm with a pump fluence of  $10 \mu\text{J}/\text{cm}^2$ . The corresponding time resolved traces below each TAM panel show carrier dynamics taken at positions as indicated. The perovskites studied are: MAFA (A, E), 5% CsMAFA (B, F), 5% RbMAFA (C, G) and 5% Cs 5% RbMAFA (D, H). Scale bars:  $1 \mu\text{m}$ .

### 6.1.6 Conclusion

The halide homogenization observed in the first part of this chapter coincides with long-lived charge carrier dynamics, spatially homogenous carrier dynamics visualized by ultrafast microscopy, as well as improved photovoltaic device performance. We find that Rb and K phase-segregate in highly concentrated clusters. We see that the alkali metals are homogenizing the halide distributions, but at higher concentrations, they form recombination-active sites. This work helps elucidate the limitations of adding these alkali-metal halides as we aim to fundamentally resolve the homogenization of carrier dynamics and ultimately provide insight that will translate to high current collection and fill factors due to homogenized halides. These insights into the interplay between composition, microstructure, and macroscopic properties pave the way to improved performance in this rapidly growing family of lead-halide materials for solar cell applications.

## 6.2 Hybrid Perovskite Quantum Wells

### 6.2.1 Abstract

Two-dimensional (2D) semiconductor superlattices (or quantum wells), which are usually fabricated through metal-organic chemical vapor deposition or molecular beam epitaxy, are key building blocks in modern optoelectronics.<sup>226-228</sup> The ability to simultaneously realize defect-free growth and to individually fine-tune the chemical composition, layer thickness, and band structure of each layer is essential for achieving desired device performance. Here, we investigated the charge transfer and energy transfer mechanisms associated with these hybrid quantum wells. A molecular approach was taken to synthesize these high-quality organic-inorganic hybrid perovskite quantum wells with tunable structures and band alignments. The energy transfer and charge transfer between adjacent organic and inorganic layers are extremely fast and efficient, as

revealed by ultrafast spectroscopy characterizations. Moreover, the 2D hybrid perovskite superlattices are surprisingly stable, thanks to the protection of bulky hydrophobic organic groups. The molecularly engineered 2D semiconductors are on a par with III-V quantum wells and are promising for next-generation electronics, optoelectronics, and photonics.

## 6.2.2 Introduction

### 6.2.2.1 Two-Dimensional Perovskites

Recently, two-dimensional (2D) layered halide perovskites have attracted considerable attention.<sup>36, 229-235</sup> 2D perovskite structures can be understood as atomically thin slabs cut from the 3D parent structures along different crystal directions are sandwiched by two layers of large organic cations.<sup>236, 237</sup> The dimensionality of the hybrid perovskite structures can be tailored by inserting organic cations with long carbon chain lengths, forming atomically thin 2D quantum wells with layers separated by organic chains and held together by van der Waals forces (schematically shown in Figure 6.2.1)<sup>238</sup>. 2D perovskites resemble slabs that are cut out from the 3D parent structure, which are also known as Ruddlesden-Popper (RP) phase. The 2D perovskite has the general chemical formula of  $(R)_2(A)_{n-1}B_nX_{3n+1}$ , where R is a large cation such as an organic ligand, A is a regular/small cation such as methylammonium, B is the divalent cation ( $Pb^{2+}$  or  $Sn^{2+}$ ), and X is a halide.

The variable n is an integer, which is indicative of the number of metal halide octahedral layers between the two R cation layers. When n is infinitely thick, the structure becomes a 3D halide perovskite ( $ABX_3$ ), as mentioned throughout this work. When  $n = 1, 2, 3$ , etc., the structure resembles an idealized quantum well with only a few atomic layers of the octahedral cage,  $[BX_6]^{4-}$ , separated by long R cations. Many of the repeating units can stack together through van der Waals

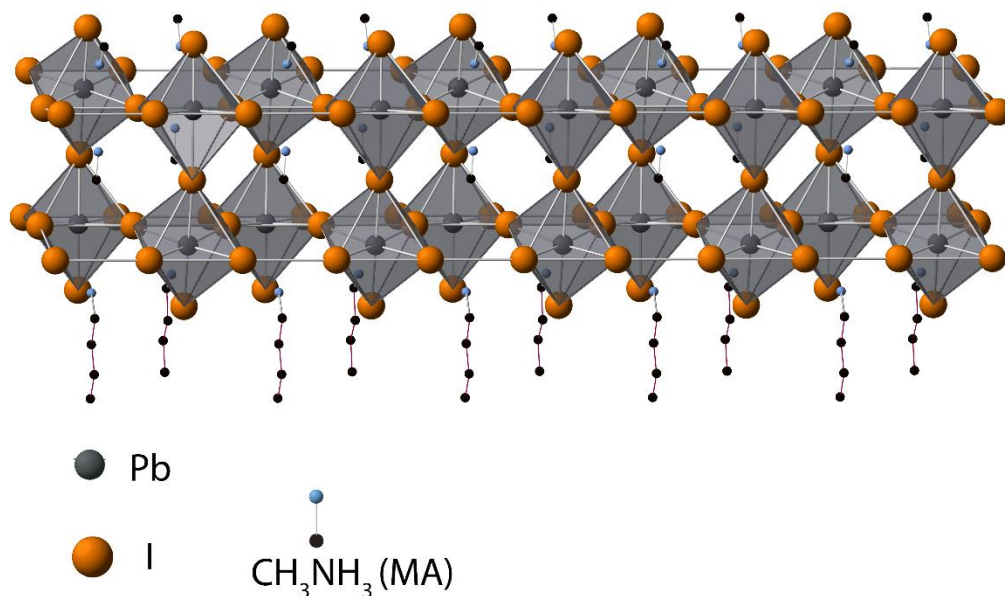


Figure 6.2.1 Schematic illustration of a two-dimensional hybrid halide perovskite

interactions to form bulk crystals, which can later be mechanically exfoliated into thin sheets (monolayer to few layers thick).

While there is a large number of reports regarding 2D perovskites that incorporate insulating aliphatic ammonium cations, only a few efforts have attempted to incorporate electronically active organic moieties.<sup>35, 239-249</sup> For example, thin films containing simple aromatic oligothiophene, pyrene, di-acetylene, and carbazole units were prepared using a spin-coating method.<sup>239, 241-243, 245</sup> Unfortunately, in most reports only polycrystalline thin films with low crystallinity can be obtained. Mitzi et al. successfully grew several quaterthiophene-perovskite hybrid crystals<sup>240</sup> and Wudl et al. grew a quasi-perovskite crystal containing tetrathiafulvalene<sup>247</sup> but their detailed band alignments and charge carrier dynamics are not fully elucidated.<sup>240</sup> Importantly, it was found that incorporating large conjugated organic groups into the inorganic matrix to make high quality superlattices is challenging. To date, a fundamental understanding

about how molecular structures influence the overall morphology and properties of hybrid perovskites and the range of organic cations that can be incorporated into the lattice is limited.

Incident light absorption in a semiconductor material leads to the generation of the previously mentioned electron-hole pairs, known as excitons. These Coulombically bound photogenerated particles exist in two main classifications: Frenkel excitons and Wannier-Mott excitons. Frenkel excitons are a tightly bound electron-hole pair, with binding energies on the order of 0.1-0.5 eV and these are primarily found in organic materials due to their small dielectric constants.<sup>250, 251</sup> Inorganic semiconductors (large dielectric constant) exhibit Wannier-Mott excitons, which are more loosely bound (hundreds of meV) due to the electric field screening reducing the Coulombic interaction between the electron and hole.<sup>252</sup> This work will primarily focus on a hybrid organic and inorganic material in which exhibits unique exciton properties such as a very low binding energy. Such low exciton binding energies lead to the existence of free carriers in the material after optical excitation, which is highly desirable since the energetic barrier for charge separation is minimal. This allows for a less convoluted conversion process where the photogenerated charge carrier transport properties are of importance to this work.

### 6.2.3 Material Preparation

To prepare thin films of 2D perovskites, bare Si/SiO<sub>2</sub> wafers or glass slides were used as the substrate for spin coating the 2D perovskite thin film. Substrates were cleaned by ultrasonication in isopropanol, acetone, water, and isopropanol again for 5 min; then dried using nitrogen gas. The substrates were treated with UV-Ozone for 10 min then transferred into a glove box for further use. As-synthesized 4T-HI (53.0 mg, 100 μmol) and PbI<sub>2</sub> (23.0 mg, 50 μmol) were dissolved in 0.25 mL of anhydrous DMF under 70 °C. The DMF solution (0.2 M) was let cool to room temperature for spin coating. (4T)<sub>2</sub>PbI<sub>4</sub> thin films were prepared by spin coating the DMF

solution at 2000 rpm for 60 s, followed by thermal annealing at 200 °C on a hot plate for 10 min in nitrogen. All other ligands based 2D perovskite thin films were prepared using a similar procedure. (BA)<sub>2</sub>PbI<sub>4</sub> thin films were annealed at 100 °C, (2T)<sub>2</sub>PbI<sub>4</sub> thin films at 120 °C, (4TCN)<sub>2</sub>PbI<sub>4</sub> thin films at 180 °C. For (BT)<sub>2</sub>FAPb<sub>2</sub>I<sub>7</sub> and (BT)<sub>2</sub>FA<sub>2</sub>Pb<sub>3</sub>I<sub>10</sub> thin films, the optimized annealing temperature is 150 °C. Addition of 5% CsI was required for preparation of thin films from (BT)<sub>2</sub>FA<sub>2</sub>Pb<sub>3</sub>I<sub>10</sub> DMF solution. (2T)<sub>2</sub>PbI<sub>4</sub> forms the desired perovskite phase immediately after solvent drying. For all other thin films an extra thermal annealing step is required to generate the perovskite phase. This difference may be due to the relative size and bulkiness of the ligands and the intermolecular interactions of these conjugated ligands, therefore requiring more reorganization energy to initiate the crystallization process.

To grow nanocrystals of the 2D perovskites, all solution preparations and thin film growth experiments were carried out inside a nitrogen-filled glove box with oxygen and water levels less than 1 ppm. As-synthesized 4T-HI (10.6 mg, 20 μmol) and PbI<sub>2</sub> (4.6 mg, 10 μmol) were dissolved in 1 mL of anhydrous dimethyl formamide (DMF) and 1 mL of anhydrous chlorobenzene (CB) inside a 4 mL vial. The solution was then diluted 60 times with an acetonitrile/chlorobenzene (1:2.5 volume ratio) co-solvent. Before use, the diluted solution was further diluted 5 times with either chlorobenzene (CB) or CB/acetonitrile (3:1 volume ratio) co-solvent. Si/SiO<sub>2</sub> was used as the substrate for the 2D perovskite growth. Si/SiO<sub>2</sub> substrates were cleaned by ultrasonication in isopropanol, acetone, water, and isopropanol again for 5 min; then dried using nitrogen gas. The substrates were then transferred into the glove box and preheated at 80 °C on a hot plate. 10 μL of the diluted solution was dropped onto the Si/SiO<sub>2</sub> surface and dried at 80 °C for 10 min. Thin sheets of (4T)<sub>2</sub>PbI<sub>4</sub> grew spontaneously as the solvent evaporated. All other ligands based 2D perovskite derivatives were synthesized using a similar procedure.

## 6.2.4 Material Characterization

### 6.2.4.1 Optical Characterization

Transient absorption spectra were measured using a femtosecond pump–probe system with a home-built transient absorption microscope. Laser pulses at 1030 nm with 200 fs duration were generated using a 400 kHz amplified Yb:KGW laser system (PHAROS, Light Conversion Ltd.). The probe beam was a white light continuum beam spanning the 450–800 nm spectral region, created by focusing 5% of the 1030 nm fundamental output onto a YAG crystal (4.0 mm thick). The remainder of the output was used to pump an optical parametric amplifier (OPA, TOPAS-Twins, Light Conversion Ltd.) to generate pump pulses with tunable photon energies for transient absorption experiments. For these measurements, the pump wavelength was 400 nm (20  $\mu$ W). The pump and probe beams were focused down with a reflective objective (40x, 0.5 NA).

PL images were taken using an Olympus microscope coupled with an X-CITE 120Q UV lamp. Steady-state photoluminescence and time-resolved photoluminescence measurements were performed by employing a home-built confocal micro-photoluminescence setup. A picosecond pulsed diode laser (Pico-Quant, LDH-P-C-450B) with an excitation wavelength of 447 nm (FWHM = 50 ps) and a repetition rate of 40 MHz was used to excite the sample for steady state measurements, which was focused by a 40 $\times$  (NA = 0.6) objective. The PL emission was collected with the same objective, dispersed with a monochromator (Andor Technology) and detected by a TE cooled charge coupled device (Andor Technology). For time resolved PL measurements, the excitation density was  $\sim 40$  nJ/cm<sup>2</sup>. PL dynamics were measured using a single photon avalanche diode (Pico-Quant, PDM series) and a single photon counting module (Pico-Quant). The time resolution of this setup is  $\sim 100$  ps. Further details on both experimental setups and schematics of the setups are covered in Chapter 2.

## 6.2.5 Results and Discussion

### 6.2.5.1 Efficient Energy Transfer and Charge Transfer Between Adjacent Organic and Inorganic Layers of 2D Perovskites

In this work, we investigate structurally-tunable organic-inorganic hybrid perovskite quantum wells in both nanocrystal and bulk forms. Figure 6.2.2 shows the organic ligands that are used for the large cation in the R site of the 2D structure –  $(R)_2(A)_{n-1}B_nX_{3n+1}$  (Figure 6.2.1). The ligands investigated are the electron rich tetrathiophene (methylated and non-methylated) and the electron-deficient 3,4-dicyanothiophene and 2,1,3-benzothiadiazole (for short, we name the molecules as 4T (4Tm), 4TCNm, and BTm; respectively – m indicating a methyl group present). Additionally, a short conjugated organic ligand is also studied which contains a bithiophene, this will be referred to as 2T. The electronic properties and band alignments are easily tuned with respect to the perovskite layer by altering the organic ligand.



Figure 6.2.2 Chemical structures of the newly designed conjugated organic ligands with an ammonium ion as the end group.

A simple vapor diffusion method at room temperature was used to successfully prepare bulk crystals for four of the hybrid materials,  $(BA)_2PbI_4$ ,  $(2T)_2PbI_4$ ,  $(4Tm)_2PbI_4$ , and  $(BTm)_2PbI_4$ . The ammonium ion terminated conjugated ligands can be used to grow molecularly-thin 2D crystals (down to a single quantum well thick) directly on Si/SiO<sub>2</sub> substrates from a ternary co-solvent.<sup>253</sup> Figure 6.2.3 a shows the optical microscope images of the assembled 2D crystals of

(2T)<sub>2</sub>PbI<sub>4</sub>, (4Tm)<sub>2</sub>PbI<sub>4</sub>, (4TCNm)<sub>2</sub>PbI<sub>4</sub> and (BTm)<sub>2</sub>PbI<sub>4</sub> and the images of the corresponding single quantum wells in the insets. 2D sheets with a lateral size of around 10 to 20 μm and well-defined square shapes were obtained. The thickness of these single quantum wells was characterized by atomic force microscopy. 2D crystals with thicknesses of ~ 3-4 nm were confirmed, indicating a single quantum well structure with only one layer of the PbI<sub>4</sub><sup>2-</sup> sheet sandwiched by two layers of the organic semiconducting ligands can be obtained.

Figure 6.2.3 b shows the corresponding photoluminescence (PL) images under UV irradiation and Figure 6.2.3 c shows the PL spectra of the mono-layer sheets (red curve) and the bulk crystals (dark red curve) with excitation by a 375 nm laser. The absorption and emission spectra of the pure organic ligands are shown in Figure 6.2.4 and Figure 6.2.5, respectively. For comparison, the PL spectrum of the previously reported 2D perovskite (BA)<sub>2</sub>PbI<sub>4</sub> is also shown (the grey dashed curves). (2T)<sub>2</sub>PbI<sub>4</sub> exhibits a green color, (4Tm)<sub>2</sub>PbI<sub>4</sub> and (4TCNm)<sub>2</sub>PbI<sub>4</sub> display no PL, and (BTm)<sub>2</sub>PbI<sub>4</sub> shows a red color. A mono-layer (2T)<sub>2</sub>PbI<sub>4</sub> crystal shows a strong and narrow green PL with a peak at 518.4 nm (full width at half maximum is 20 nm), which is very close to that of (BA)<sub>2</sub>PbI<sub>4</sub>, indicating that the PL originates from the inorganic layer. The PL of the (2T)<sub>2</sub>PbI<sub>4</sub> mono-layer is about 7 nm blue-shifted compared to the bulk crystal (525.2 nm), which is likely due to structural relaxation of the soft lattice. Similar effects are observed in (BA)<sub>2</sub>PbI<sub>4</sub> (Figure 6.2.3 c1 inset) and other systems.<sup>253</sup> A bi-layer (BTm)<sub>2</sub>PbI<sub>4</sub> crystal shows a strong red PL at ~660 nm, which is from the BTm ligands, while no PL from the inorganic layer is detected. The PL of the bi-layer is ~6 nm blue-shifted compared to the PL of the bulk crystal.

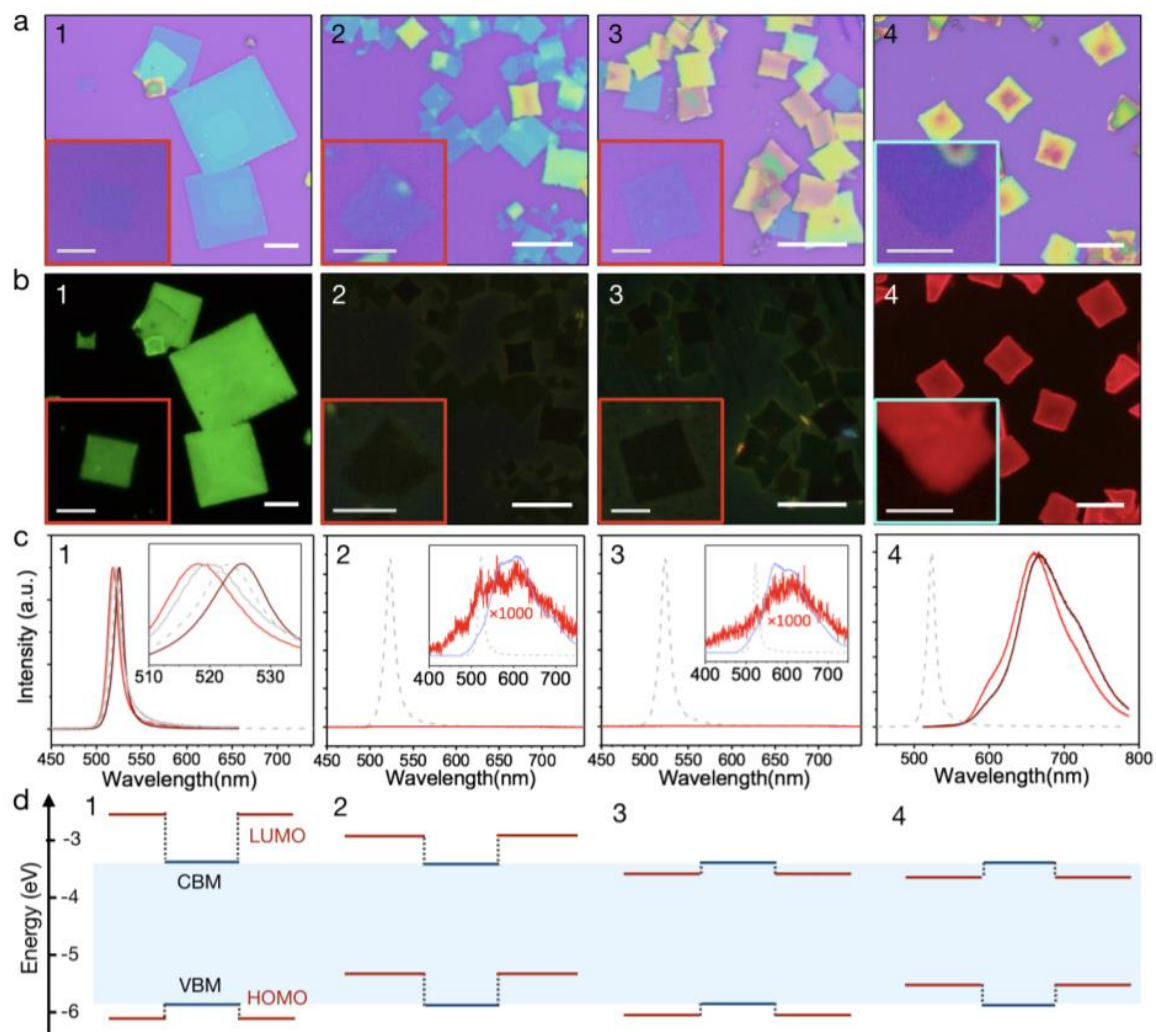


Figure 6.2.3 (a) Optical microscopy images of the assembled 2D crystals grown on  $SiO_2/Si$  substrates:  $(2T)_2PbI_4$  (a1),  $(4Tm)_2PbI_4$  (a2),  $(4TCNm)_2PbI_4$  (a3),  $(BTm)_2PbI_4$  (a4). All scale bars are 10  $\mu m$ . The insets are images for mono-layer thick single quantum well structures. All scale bars in the insets are 5  $\mu m$ . (b) Corresponding PL image of the assembled 2D crystals under UV excitation. All scale bars are 10  $\mu m$ . The insets are the PL images for the corresponding mono-layer thick single quantum well structures. All scale bars in the insets are 5  $\mu m$ . (c) Corresponding steady state PL spectra of the mono-layers (red curves), bulk crystals (dark red curves). In c1 inset,  $(BA)_2PbI_4$  mono-layers (grey solid curves) and bulk crystals (grey dashed curves) are shown for comparison. In c2 and c3 insets, the PL for the 4Tm and 4TCNm ligands (blue curves) are shown for comparison. The weak signals come from both the organic ligands and the perovskite layers. (d) Semi-quantified band structures of the hybrid 2D perovskite superlattices.

The PL results of  $(2T)_2PbI_4$  and  $(BTm)_2PbI_4$  indicate that energy resonates and transfers efficiently to the lowest energy emitter. For  $(4Tm)_2PbI_4$  and  $(4TCNm)_2PbI_4$ , emissions from both the inorganic layer and the organic layers are 99.9% quenched (Figure 6.2.3 c2 and c3 insets), suggesting efficient photo-induced charge separation and possible inter-layer exciton (or charge-transfer exciton) formation at the organic-inorganic interface.<sup>254</sup> Based on the steady-state PL study, the hybrid 2D crystals exhibit type I, type II, type II (reverse), and type I (reverse) band alignments for  $(2T)_2PbI_4$ ,  $(4Tm)_2PbI_4$ ,  $(4TCNm)_2PbI_4$  and  $(BTm)_2PbI_4$ , respectively.

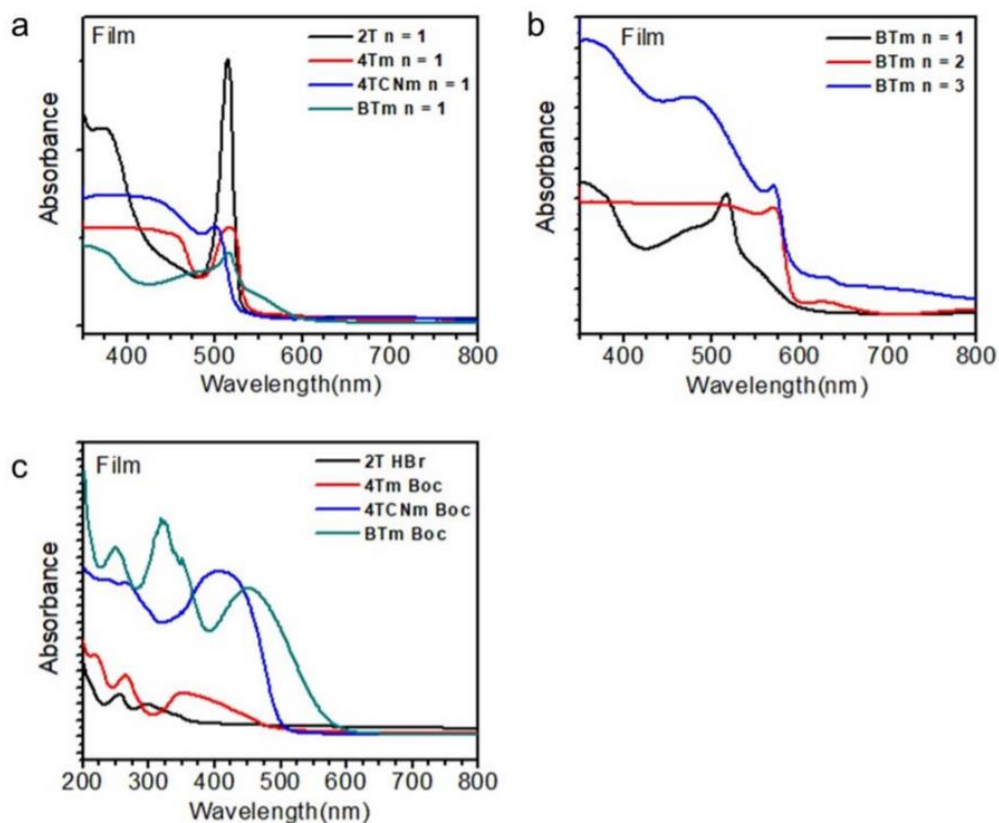


Figure 6.2.4 (a) Absorption spectra of polycrystalline thin films of 2D hybrid halide perovskites based on conjugated ligands. (b) Absorption spectra of polycrystalline thin films of 2D hybrid halide perovskites based on BT conjugated ligands with different thickness of the perovskite layer. (c) Absorption spectra of thin films of pure organic conjugated ligands.

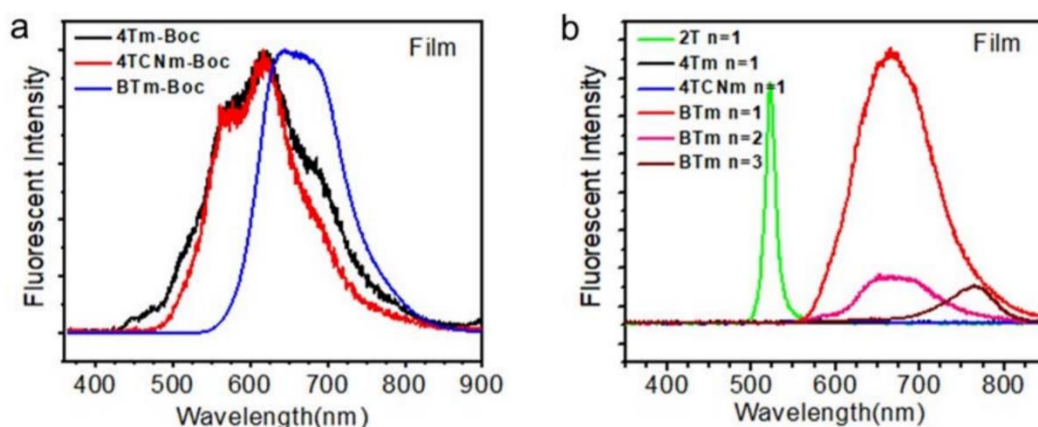


Figure 6.2.5 (a) Steady state photoluminescence spectra of thin films of pure organic conjugated ligands. (b) Steady state photoluminescence spectra of thin films of 2D hybrid halide perovskite based on conjugated ligands. Normalized steady state photoluminescence spectra of thin films of 4T (c) and 4TCN (d) based 2D perovskites.

The energy and charge transfer processes were further characterized via time-resolved PL spectroscopy and transient absorption (TA) spectroscopy. As shown in Figure 6.2.7 a2 and a3, the decrease of PL lifetime in  $(4Tm)_2PbI_4$  and  $(4TCNm)_2PbI_4$  is consistent with their type II band alignment. To elucidate the charge transfer time, we compared the exciton bleach dynamics in the new crystals to those in  $(BA)_2PbI_4$  where no charge transfer and exciton dissociation are expected (Figure 6.2.6 and Figure 6.2.7 b). The exciton bleach dynamics are extracted from the TA spectrum shown in Figure 6.2.6. The dynamics shown in Figure 6.2.7 b accentuate the impact that is observed when organic and inorganic components are together. To do this, we take the difference between the exciton dynamics of the perovskite ( $(BA)_2PbI_4$  – black curves) alone and hybrid quantum well sample (inorganic and organic together – red curves), which results in the blue curves of Figure 6.2.7 b. All the active components, including the inorganic  $PbI_4^{2-}$  layer and organic molecules, except for 2T, can be pumped by the excitation wavelength used (400 nm) and the charge/energy transfer processes can be monitored by exciton bleaching. In the case of 2T, its band gap is beyond our laser's excitation energy and the excited states of the 2T molecules are not

accessible. Therefore, there is no strong correlation in the TA spectra between  $(\text{BA})_2\text{PbI}_4$  and  $(2\text{T})_2\text{PbI}_4$  (Figure 6.2.7 b1), and the energy transfer time from 2T to  $\text{PbI}_4^{2-}$  layer was not extracted. The corresponding charge transfer time for  $(4\text{Tm})_2\text{PbI}_4$  and  $(4\text{TCNm})_2\text{PbI}_4$  was determined to be  $26 \pm 7$  and  $7 \pm 2$  ps, respectively.<sup>254</sup> For  $(\text{BTm})_2\text{PbI}_4$ , the decrease of the exciton bleach lifetime is consistent with its type I band alignment, the longer PL lifetime compared to  $(\text{BA})_2\text{PbI}_4$  mostly reflects the exciton lifetime of the BTm molecules. The corresponding energy transfer time was determined to be  $15 \pm 2$  ps. These efficient and ultrafast energy/charge transfer processes suggest potential applications in efficient solid-state light sources and high-gain photodetectors.

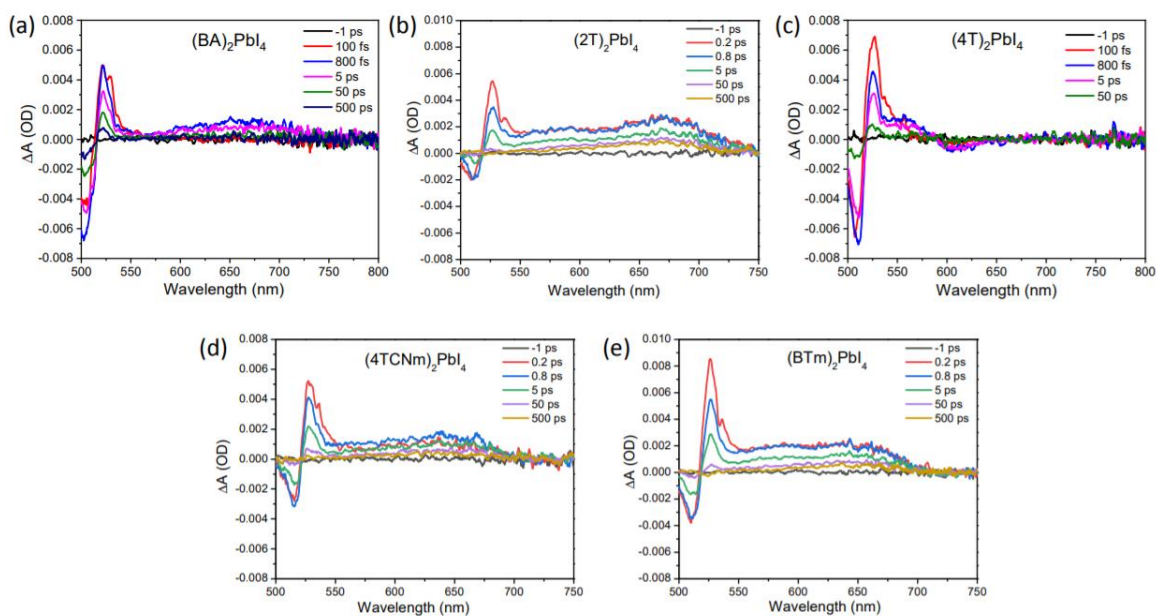


Figure 6.2.6 (a) Transient absorption spectra of a  $(\text{BA})_2\text{PbI}_4$  crystal. (b) Transient absorption spectra of a  $(2\text{T})_2\text{PbI}_4$  crystal. (c) Transient absorption spectra of a  $(4\text{Tm})_2\text{PbI}_4$  crystal. (d) Transient absorption spectra of a  $(4\text{TCNm})_2\text{PbI}_4$  crystal. (e) Transient absorption spectra of a  $(\text{BTm})_2\text{PbI}_4$  crystal.

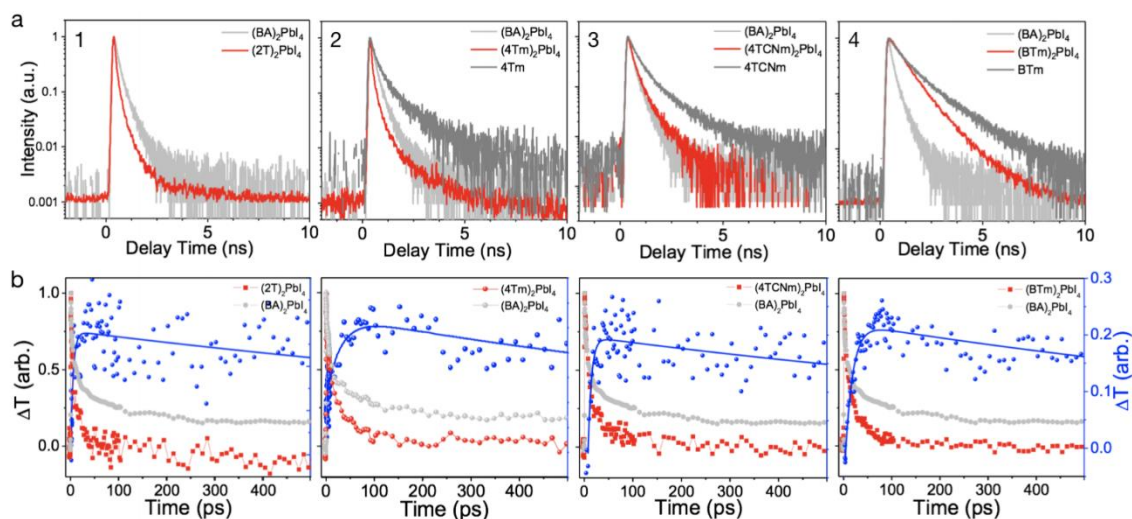


Figure 6.2.7 (a) Time-resolved PL spectra of (2T)<sub>2</sub>PbI<sub>4</sub> (a1), (4Tm)<sub>2</sub>PbI<sub>4</sub> (a2), (4TCNm)<sub>2</sub>PbI<sub>4</sub> (a3), (BTm)<sub>2</sub>PbI<sub>4</sub> (a4) 2D crystals. The PL decay curves for (BA)<sub>2</sub>PbI<sub>4</sub> (grey dashed curves) and pure organic ligands (deep grey curves) are shown for comparison. (b) Bleach dynamics and extraction of the energy and charge transfer time of the corresponding 2D crystals. The blue curves indicate the difference of exciton bleaching dynamics between the new 2D perovskites with (BA)<sub>2</sub>PbI<sub>4</sub>. Energy and charge transfer times were extracted based on these data.

In addition to the efficient charge/energy transfer processes, we have shown the remarkable stability of these materials. The ultrafast charge/energy transfer processes make these material suitable candidates for a variety of applications – however, perovskites are notorious for their instability. In this case, the large conjugated ligands are not only essential to tune the crystal morphology and electronic properties but are also to improve the stability of the halide perovskites. All perovskite materials are notorious for being unstable in air due to the detrimental effects of moisture. What better way to show stability to water, than to submerge the samples under water? Remarkably, we show that the new perovskite quantum wells are extremely stable. This is shown by Figure 6.2.8, where PL images of the samples under UV light illumination before and after submerging under water. (BA)<sub>2</sub>PbI<sub>4</sub> degraded and the PL disappeared immediately when coming into contact with water. The green emission of (2T)<sub>2</sub>PbI<sub>4</sub> was retained for about one minute and then started to degrade. (4Tm)<sub>2</sub>PbI<sub>4</sub>, (4TCNm)<sub>2</sub>PbI<sub>4</sub>, and (BTm)<sub>2</sub>PbI<sub>4</sub> showed no signs of

decomposition after 5 minutes under water (Figure 6.2.8). They also exhibit excellent thermal stability, showing no signs of decomposition up to 250 °C. The origin of this enhanced stability was investigated using molecular dynamics simulations of  $(\text{BA})_2\text{PbI}_4$ ,  $(2\text{T})_2\text{PbI}_4$ , and  $(\text{BTm})_2\text{PbI}_4$  with direct immersion in water. It was found that water penetrates the  $(\text{BA})_2\text{PbI}_4$  organic layer and completely dissolves the surface cations within 2 ns. The intermediate case of  $(2\text{T})_2\text{PbI}_4$  exhibits partial penetration of water into the organic layer. The most interesting result is the  $(\text{BT})_2\text{PbI}_4$  film, which exhibits minimal water penetration into the upper organic layer and the inorganic surface remains dehydrated. We presume that the bulky and hydrophobic organic conjugated groups were able to provide better protection to the perovskites, which results in dramatic enhancement of their environmental stability.

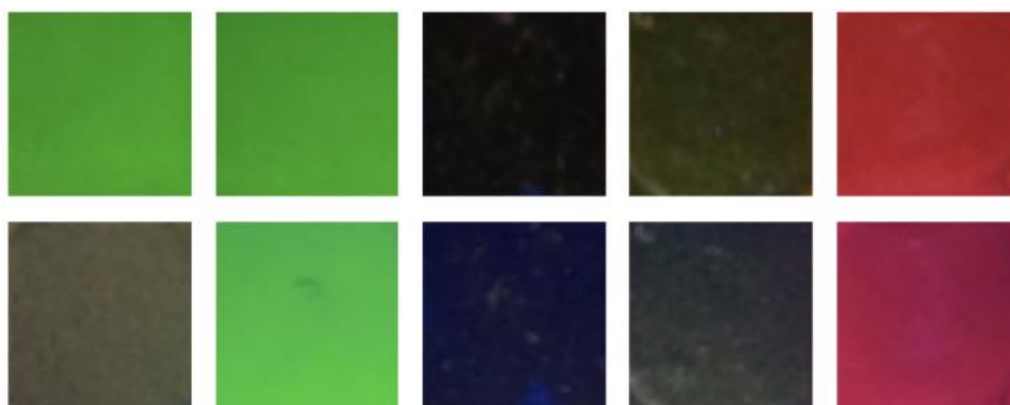


Figure 6.2.8 Photos of 2D hybrid halide perovskite thin films with different organic ligands under UV irradiation before (top) and after (bottom) immersion in water. From left to right:  $(\text{BA})_2\text{PbI}_4$ ,  $(2\text{T})_2\text{PbI}_4$ ,  $(4\text{Tm})_2\text{PbI}_4$ ,  $(4\text{TCNm})_2\text{PbI}_4$ ,  $(\text{BTm})_2\text{PbI}_4$ .

### 6.2.6 Conclusion

In summary of the 2D perovskite work, we have demonstrated that the organic and inorganic building blocks of hybrid perovskite materials can be manipulated to produce widely-tunable single-crystalline quantum wells. The overall optical and electronic properties are determined by the interaction of these two components. We observed ultrafast and efficient charge/energy transfer processes in these 2D perovskite quantum wells via transient absorption spectroscopy and other complementary optical measurements. We anticipate further studies on the physics of 2D hybrid perovskite single and multiple quantum wells towards enhanced light harvesting, light emission, charge transport properties, as well as other emerging new properties. This work provides a huge potential towards molecularly engineered solution-processed semiconductors quantum wells with strikingly high intrinsic stability for potential applications in nanoelectronics, optoelectronics, and photonics.

## REFERENCES

1. (IEA), I. E. A. *World Energy Outlook 2016*; 978-92-64-26495-3; 2016.
2. S. Lewis, N.; Crabtree, G., *Basic Research Needs for Solar Energy Utilization: report of the Basic Energy Sciences Workshop on Solar Energy Utilization, April 18-21, 2005*. 2005.
3. Hoffert, M. I.; Caldeira, K.; Benford, G.; Criswell, D. R.; Green, C.; Herzog, H.; Jain, A. K.; Kheshgi, H. S.; Lackner, K. S.; Lewis, J. S.; Lightfoot, H. D.; Manheimer, W.; Mankins, J. C.; Mauel, M. E.; Perkins, L. J.; Schlesinger, M. E.; Volk, T.; Wigley, T. M. L., Advanced technology paths to global climate stability: Energy for a greenhouse planet. *Science* **2002**, 298 (5595), 981-987.
4. (BP), B. P. *BP Statistical Review of World Energy June 2017*; 2017.
5. Shockley, W.; Queisser, H. J., Detailed Balance Limit of Efficiency of p-n Junction Solar Cells. *Journal of Applied Physics* **1961**, 32 (3), 510-519.
6. Rawat, R.; Lamba, R.; Kaushik, S. C., Thermodynamic study of solar photovoltaic energy conversion: An overview. *Renewable & Sustainable Energy Reviews* **2017**, 71, 630-638.
7. Ruppel, W.; Wurfel, P., UPPER LIMIT FOR THE CONVERSION OF SOLAR-ENERGY. *Ieee Transactions on Electron Devices* **1980**, 27 (4), 877-882.
8. Richter, A.; Hermle, M.; Glunz, S. W., Reassessment of the Limiting Efficiency for Crystalline Silicon Solar Cells. *Ieee Journal of Photovoltaics* **2013**, 3 (4), 1184-1191.
9. Graetzel, M.; Janssen, R. A. J.; Mitzi, D. B.; Sargent, E. H., Materials interface engineering for solution-processed photovoltaics. *Nature* **2012**, 488 (7411), 304-312.
10. Masetti, G.; Severi, M.; Solmi, S., MODELING OF CARRIER MOBILITY AGAINST CARRIER CONCENTRATION IN ARSENIC-DOPED, PHOSPHORUS-DOPED, AND BORON-DOPED SILICON. *Ieee Transactions on Electron Devices* **1983**, 30 (7), 764-769.
11. Sze, S. M.; Ng, K. K., *Physics of Semiconductor Devices*. Third Edition ed.; John Wiley & Sons, INC: 2007.
12. Burschka, J.; Pellet, N.; Moon, S. J.; Humphry-Baker, R.; Gao, P.; Nazeeruddin, M. K.; Gratzel, M., Sequential deposition as a route to high-performance perovskite-sensitized solar cells. *Nature* **2013**, 499 (7458), 316-+.
13. Bi, D. Q.; Moon, S. J.; Haggman, L.; Boschloo, G.; Yang, L.; Johansson, E. M. J.; Nazeeruddin, M. K.; Gratzel, M.; Hagfeldt, A., Using a two-step deposition technique to prepare perovskite (CH<sub>3</sub>NH<sub>3</sub>PbI<sub>3</sub>) for thin film solar cells based on ZrO<sub>2</sub> and TiO<sub>2</sub> mesostructures. *Rsc Advances* **2013**, 3 (41), 18762-18766.
14. You, J. B.; Yang, Y. M.; Hong, Z. R.; Song, T. B.; Meng, L.; Liu, Y. S.; Jiang, C. Y.; Zhou, H. P.; Chang, W. H.; Li, G.; Yang, Y., Moisture assisted perovskite film growth for high performance solar cells. *Applied Physics Letters* **2014**, 105 (18).
15. Noel, N. K.; Abate, A.; Stranks, S. D.; Parrott, E. S.; Burlakov, V. M.; Goriely, A.; Snaith, H. J., Enhanced Photoluminescence and Solar Cell Performance via Lewis Base Passivation of Organic Inorganic Lead Halide Perovskites. *Acs Nano* **2014**, 8 (10), 9815-9821.
16. Chang, J. J.; Zhu, H.; Xiao, J. X.; Isikgor, F. H.; Lin, Z. H.; Hao, Y.; Zeng, K. Y.; Xu, Q. H.; Ouyang, J. Y., Enhancing the planar heterojunction perovskite solar cell performance through tuning the precursor ratio. *Journal of Materials Chemistry A* **2016**, 4 (20), 7943-7949.

17. Dequilettes, D. W.; Jariwala, S.; Burke, S.; Ziffer, M. E.; Wang, J. T. W.; Snaith, H. J.; Ginger, D. S., Tracking Photoexcited Carriers in Hybrid Perovskite Semiconductors: Trap-Dominated Spatial Heterogeneity and Diffusion. *Acs Nano* **2017**, *11* (11), 11488-11496.
18. Eperon, G. E.; Moerman, D.; Ginger, D. S., Anticorrelation between Local Photoluminescence and Photocurrent Suggests Variability in Contact to Active Layer in Perovskite Solar Cells. *Acs Nano* **2016**, *10* (11), 10258-10266.
19. Clark, K. A.; Krueger, E. L.; Vanden Bout, D. A., Direct Measurement of Energy Migration in Supramolecular Carbocyanine Dye Nanotubes. *Journal of Physical Chemistry Letters* **2014**, *5* (13), 2274-2282.
20. Kuciauskas, D.; Myers, T. H.; Barnes, T. M.; Jensen, S. A.; Motz, A. M. A., Time-resolved correlative optical microscopy of charge-carrier transport, recombination, and space-charge fields in CdTe heterostructures. *Applied Physics Letters* **2017**, *110* (8).
21. Guo, Z.; Manser, J. S.; Wan, Y.; Kamat, P. V.; Huang, L. B., Spatial and temporal imaging of long-range charge transport in perovskite thin films by ultrafast microscopy. *Nature Communications* **2015**, *6*.
22. Wan, Y.; Guo, Z.; Zhu, T.; Yan, S. X.; Johnson, J.; Huang, L. B., Cooperative singlet and triplet exciton transport in tetracene crystals visualized by ultrafast microscopy. *Nature Chemistry* **2015**, *7* (10), 785-792.
23. Huang, L. B.; Cheng, J. X., Nonlinear Optical Microscopy of Single Nanostructures. *Annual Review of Materials Research, Vol 43* **2013**, *43*, 213-236.
24. Devadas, M. S.; Devkota, T.; Johns, P.; Li, Z. M.; Lo, S. S.; Yu, K.; Huang, L. B.; Hartland, G. V., Imaging nano-objects by linear and nonlinear optical absorption microscopies. *Nanotechnology* **2015**, *26* (35).
25. Chakhmouradian, A. R.; Woodward, P. M., Celebrating 175 years of perovskite research: a tribute to Roger H. Mitchell. *Physics and Chemistry of Minerals* **2014**, *41* (6), 387-391.
26. Kalendova, A.; Vesely, D.; Kalenda, P., Anticorrosion pigment based on calcium titanate with a perovskite structure. *Pigment & Resin Technology* **2007**, *36* (3), 123-133.
27. Kalendova, A.; Vesely, D.; Kalenda, P., Pigments with Ti<sup>4+</sup>-Zn<sup>2+</sup>, Ca<sup>2+</sup>, Sr<sup>2+</sup>, Mg<sup>2+</sup>-based on mixed metal oxides with spinel and perovskite structures for organic coatings. *Pigment & Resin Technology* **2007**, *36* (1), 3-17.
28. Crystal Structure of Barium Titanate. *Nature* **1945**, *155*, 484.
29. Gunter, P., HISTORY OF FERROELECTRICITY .5. ELECTROOPTICAL EFFECTS IN FERROELECTRICS. *Ferroelectrics* **1987**, *74* (3-4), 305-307.
30. MØLLER, C. K., Crystal Structure and Photoconductivity of Cæsium Plumbahalides. *Nature* **1958**, *182*, 1436.
31. Weber, D., CH<sub>3</sub>NH<sub>3</sub>PbX<sub>3</sub>, ein Pb(II)-System mit kubischer Perowskitstruktur / CH<sub>3</sub>NH<sub>3</sub>PbX<sub>3</sub>, a Pb(II)-System with Cubic Perovskite Structure. In *Zeitschrift für Naturforschung B*, 1978; Vol. 33, p 1443.
32. Era, M.; Morimoto, S.; Tsutsui, T.; Saito, S., ORGANIC-INORGANIC HETEROSTRUCTURE ELECTROLUMINESCENT DEVICE USING A LAYERED PEROVSKITE SEMICONDUCTOR (C<sub>6</sub>H<sub>5</sub>C<sub>2</sub>H<sub>4</sub>NH<sub>3</sub>)<sub>2</sub>PbI<sub>4</sub>. *Applied Physics Letters* **1994**, *65* (6), 676-678.
33. Era, M.; Morimoto, S.; Tsutsui, T.; Saito, S., Electroluminescent device using two dimensional semiconductor (C<sub>6</sub>H<sub>5</sub>C<sub>2</sub>H<sub>4</sub>NH<sub>3</sub>)<sub>2</sub>PbI<sub>4</sub> as an emitter. *Synthetic Metals* **1995**, *71* (1), 2013-2014.

34. Mitzi, D. B.; Wang, S.; Feild, C. A.; Chess, C. A.; Guloy, A. M., CONDUCTING LAYERED ORGANIC-INORGANIC HALIDES CONTAINING (110)-ORIENTED PEROVSKITE SHEETS. *Science* **1995**, *267* (5203), 1473-1476.
35. Chondroudis, K.; Mitzi, D. B., Electroluminescence from an organic-inorganic perovskite incorporating a quaterthiophene dye within lead halide perovskite layers. *Chem. Mater.* **1999**, *11* (11), 3028-3030.
36. Kagan, C. R.; Mitzi, D. B.; Dimitrakopoulos, C. D., Organic-inorganic hybrid materials as semiconducting channels in thin-film field-effect transistors. *Science* **1999**, *286* (5441), 945-947.
37. Mitzi, D. B.; Dimitrakopoulos, C. D.; Kosbar, L. L., Structurally tailored organic-inorganic perovskites: Optical properties and solution-processed channel materials for thin-film transistors. *Chemistry of Materials* **2001**, *13* (10), 3728-3740.
38. Mitzi, D. B.; Dimitrakopoulos, C. D.; Rosner, J.; Medeiros, D. R.; Xu, Z. T.; Noyan, C., Hybrid field-effect transistor based on a low-temperature melt-processed channel layer. *Advanced Materials* **2002**, *14* (23), 1772-+.
39. Hattori, T.; Taira, T.; Era, M.; Tsutsui, T.; Saito, S., Highly efficient electroluminescence from a heterostructure device combined with emissive layered-perovskite and an electron-transporting organic compound. *Chemical Physics Letters* **1996**, *254* (1-2), 103-108.
40. Kojima, A.; Teshima, K.; Shirai, Y.; Miyasaka, T., Organometal Halide Perovskites as Visible-Light Sensitizers for Photovoltaic Cells. *Journal of the American Chemical Society* **2009**, *131* (17), 6050-6051.
41. Chen, J.; Park, N.-G., Inorganic Hole Transporting Materials for Stable and High Efficiency Perovskite Solar Cells. *The Journal of Physical Chemistry C* **2018**, *122* (25), 14039-14063.
42. Yang, W. S.; Park, B. W.; Jung, E. H.; Jeon, N. J.; Kim, Y. C.; Lee, D. U.; Shin, S. S.; Seo, J.; Kim, E. K.; Noh, J. H.; Seok, S. I., Iodide management in formamidinium-lead-halide-based perovskite layers for efficient solar cells. *Science* **2017**, *356* (6345), 1376-+.
43. Manser, J. S.; Christians, J. A.; Kamat, P. V., Intriguing Optoelectronic Properties of Metal Halide Perovskites. *Chemical Reviews* **2016**, *116* (21), 12956-13008.
44. Zhu, H.; Miyata, K.; Fu, Y.; Wang, J.; Joshi, P. P.; Niesner, D.; Williams, K. W.; Jin, S.; Zhu, X. Y., Screening in crystalline liquids protects energetic carriers in hybrid perovskites. *Science* **2016**, *353* (6306), 1409-1413.
45. Whitfield, P. S.; Herron, N.; Guise, W. E.; Page, K.; Cheng, Y. Q.; Milas, I.; Crawford, M. K., Structures, Phase Transitions and Tricritical Behavior of the Hybrid Perovskite Methyl Ammonium Lead Iodide. *Scientific Reports* **2016**, *6*, 35685.
46. Hoke, E. T.; Slotcavage, D. J.; Dohner, E. R.; Bowring, A. R.; Karunadasa, H. I.; McGehee, M. D., Reversible photo-induced trap formation in mixed-halide hybrid perovskites for photovoltaics. *Chemical Science* **2015**, *6* (1), 613-617.
47. Saliba, M.; Matsui, T.; Domanski, K.; Seo, J. Y.; Ummadisingu, A.; Zakeeruddin, S. M.; Correa-Baena, J. P.; Tress, W. R.; Abate, A.; Hagfeldt, A.; Gratzel, M., Incorporation of rubidium cations into perovskite solar cells improves photovoltaic performance. *Science* **2016**, *354* (6309), 206-209.
48. McMeekin, D. P.; Sadoughi, G.; Rehman, W.; Eperon, G. E.; Saliba, M.; Hoerantner, M. T.; Haghighirad, A.; Sakai, N.; Korte, L.; Rech, B.; Johnston, M. B.; Herz, L. M.; Snaith, H. J., A mixed-cation lead mixed-halide perovskite absorber for tandem solar cells. *Science* **2016**, *351* (6269), 151-155.

49. Saliba, M.; Matsui, T.; Seo, J. Y.; Domanski, K.; Correa-Baena, J. P.; Nazeeruddin, M. K.; Zakeeruddin, S. M.; Tress, W.; Abate, A.; Hagfeldt, A.; Gratzel, M., Cesium-containing triple cation perovskite solar cells: improved stability, reproducibility and high efficiency. *Energy & Environmental Science* **2016**, *9* (6), 1989-1997.
50. Yi, C.; Luo, J.; Meloni, S.; Boziki, A.; Ashari-Astani, N.; Graetzel, C.; Zakeeruddin, S. M.; Roethlisberger, U.; Graetzel, M., Entropic stabilization of mixed A-cation ABX<sub>3</sub> metal halide perovskites for high performance perovskite solar cells. *Energy & Environmental Science* **2016**, *9* (2), 656-662.
51. Jeon, N. J.; Noh, J. H.; Yang, W. S.; Kim, Y. C.; Ryu, S.; Seo, J.; Seok, S. I., Compositional engineering of perovskite materials for high-performance solar cells. *Nature* **2015**, *517* (7535), 476-+.
52. Nie, W. Y.; Tsai, H. H.; Asadpour, R.; Blancon, J. C.; Neukirch, A. J.; Gupta, G.; Crochet, J. J.; Chhowalla, M.; Tretiak, S.; Alam, M. A.; Wang, H. L.; Mohite, A. D., High-efficiency solution-processed perovskite solar cells with millimeter-scale grains. *Science* **2015**, *347* (6221), 522-525.
53. Fu, Y.; Meng, F.; Rowley, M. B.; Thompson, B. J.; Shearer, M. J.; Ma, D.; Hamers, R. J.; Wright, J. C.; Jin, S., Solution Growth of Single Crystal Methylammonium Lead Halide Perovskite Nanostructures for Optoelectronic and Photovoltaic Applications. *Journal of the American Chemical Society* **2015**, *137* (17), 5810-5818.
54. García de Arquer, F. P.; Sargent, E. H., Perovskite nanowires find an edge. *Nature Electronics* **2018**, *1* (7), 380-381.
55. Feng, J.; Gong, C.; Gao, H.; Wen, W.; Gong, Y.; Jiang, X.; Zhang, B.; Wu, Y.; Wu, Y.; Fu, H.; Jiang, L.; Zhang, X., Single-crystalline layered metal-halide perovskite nanowires for ultrasensitive photodetectors. *Nature Electronics* **2018**, *1* (7), 404-410.
56. Wu, J.; Ye, F.; Yang, W.; Xu, Z.; Luo, D.; Su, R.; Zhang, Y.; Zhu, R.; Gong, Q., Perovskite Single-Crystal Microarrays for Efficient Photovoltaic Devices. *Chemistry of Materials* **2018**, *30* (14), 4590-4596.
57. Cho, H.; Jeong, S.-H.; Park, M.-H.; Kim, Y.-H.; Wolf, C.; Lee, C.-L.; Heo, J. H.; Sadhanala, A.; Myoung, N.; Yoo, S.; Im, S. H.; Friend, R. H.; Lee, T.-W., Overcoming the electroluminescence efficiency limitations of perovskite light-emitting diodes. *Science* **2015**, *350* (6265), 1222-1225.
58. Stranks, S. D.; Snaith, H. J., Metal-halide perovskites for photovoltaic and light-emitting devices. *Nature Nanotechnology* **2015**, *10* (5), 391-402.
59. Li, G.; Rivarola, F. W. R.; Davis, N. J. L. K.; Bai, S.; Jellicoe, T. C.; de la Pena, F.; Hou, S.; Ducati, C.; Gao, F.; Friend, R. H.; Greenham, N. C.; Tan, Z.-K., Highly Efficient Perovskite Nanocrystal Light-Emitting Diodes Enabled by a Universal Crosslinking Method. *Advanced Materials* **2016**, *28* (18), 3528-+.
60. Zhang, L.; Yang, X.; Jiang, Q.; Wang, P.; Yin, Z.; Zhang, X.; Tan, H.; Yang, Y.; Wei, M.; Sutherland, B. R.; Sargent, E. H.; You, J., Ultra-bright and highly efficient inorganic based perovskite light-emitting diodes. *Nature Communications* **2017**, *8*, 15640.
61. Yang, X.; Zhang, X.; Deng, J.; Chu, Z.; Jiang, Q.; Meng, J.; Wang, P.; Zhang, L.; Yin, Z.; You, J., Efficient green light-emitting diodes based on quasi-two-dimensional composition and phase engineered perovskite with surface passivation. *Nature Communications* **2018**, *9* (1), 570.
62. Sutherland, B. R.; Sargent, E. H., Perovskite photonic sources. *Nature Photonics* **2016**, *10*, 295.

63. Deschler, F.; Price, M.; Pathak, S.; Klintberg, L. E.; Jarausch, D. D.; Higler, R.; Huttner, S.; Leijtens, T.; Stranks, S. D.; Snaith, H. J.; Atature, M.; Phillips, R. T.; Friend, R. H., High Photoluminescence Efficiency and Optically Pumped Lasing in Solution-Processed Mixed Halide Perovskite Semiconductors. *Journal of Physical Chemistry Letters* **2014**, *5* (8), 1421-1426.
64. Yuan, L.; Huang, L. B., Exciton dynamics and annihilation in WS<sub>2</sub> 2D semiconductors. *Nanoscale* **2015**, *7* (16), 7402-7408.
65. Wu, K. W.; Bera, A.; Ma, C.; Du, Y. M.; Yang, Y.; Li, L.; Wu, T., Temperature-dependent excitonic photoluminescence of hybrid organometal halide perovskite films. *Physical Chemistry Chemical Physics* **2014**, *16* (41), 22476-22481.
66. Yamada, Y.; Nakamura, T.; Endo, M.; Wakamiya, A.; Kanemitsu, Y., Photoelectronic Responses in Solution-Processed Perovskite CH<sub>3</sub>NH<sub>3</sub>PbI<sub>3</sub> Solar Cells Studied by Photoluminescence and Photoabsorption Spectroscopy. *Ieee Journal of Photovoltaics* **2015**, *5* (1), 401-405.
67. Miyata, A.; Mitioglu, A.; Plochocka, P.; Portugall, O.; Wang, J. T. W.; Stranks, S. D.; Snaith, H. J.; Nicholas, R. J., Direct measurement of the exciton binding energy and effective masses for charge carriers in organic-inorganic tri-halide perovskites. *Nature Physics* **2015**, *11* (7), 582-U94.
68. Sun, S.; Salim, T.; Mathews, N.; Duchamp, M.; Boothroyd, C.; Xing, G.; Sum, T. C.; Lam, Y. M., The origin of high efficiency in low-temperature solution-processable bilayer organometal halide hybrid solar cells. *Energy & Environmental Science* **2014**, *7* (1), 399-407.
69. Yang, X.; Yan, X. L.; Wang, Y. C.; Chen, W.; Wang, R. Z.; Wang, W. W.; Li, H.; Ma, W. L.; Sheng, C. X., Photoluminescence in Organometal Halide Perovskites: Free Carrier Versus Exciton. *Ieee Journal of Photovoltaics* **2017**, *7* (2), 513-517.
70. Yang, W. C.; Yao, Y.; Wu, C. Q., Origin of the high open circuit voltage in planar heterojunction perovskite solar cells: Role of the reduced bimolecular recombination. *Journal of Applied Physics* **2015**, *117* (9).
71. Elliott, R. J., Intensity of Optical Absorption by Excitons. *Physical Review* **1957**, *108* (6), 1384-1389.
72. Wannier, G. H., The Structure of Electronic Excitation Levels in Insulating Crystals. *Physical Review* **1937**, *52* (3), 191-197.
73. Zhao, Y. X.; Zhu, K., Charge Transport and Recombination in Perovskite (CH<sub>3</sub>NH<sub>3</sub>)PbI<sub>3</sub> Sensitized TiO<sub>2</sub> Solar Cells. *Journal of Physical Chemistry Letters* **2013**, *4* (17), 2880-2884.
74. Amani, M.; Lien, D. H.; Kiriya, D.; Xiao, J.; Azcatl, A.; Noh, J.; Madhupathy, S. R.; Addou, R.; Santosh, K. C.; Dubey, M.; Cho, K.; Wallace, R. M.; Lee, S. C.; He, J. H.; Ager, J. W.; Zhang, X.; Yablonovitch, E.; Javey, A., Near-unity photoluminescence quantum yield in MoS<sub>2</sub>. *Science* **2015**, *350* (6264), 1065-1068.
75. Wang, H. N.; Zhang, C. J.; Rana, F., Ultrafast Dynamics of Defect-Assisted Electron Hole Recombination in Mono layer MoS<sub>2</sub>. *Nano Letters* **2015**, *15* (1), 339-345.
76. Herz, L. M., Charge-Carrier Dynamics in Organic-Inorganic Metal Halide Perovskites. *Annual Review of Physical Chemistry, Vol 67* **2016**, *67*, 65-89.
77. Yang, M.; Zeng, Y.; Li, Z.; Kim, D. H.; Jiang, C.-S.; van de Lagemaat, J.; Zhu, K., Do grain boundaries dominate non-radiative recombination in CH<sub>3</sub>NH<sub>3</sub>PbI<sub>3</sub> perovskite thin films? *Physical Chemistry Chemical Physics* **2017**, *19* (7), 5043-5050.

78. Stavrakas, C.; Zhumeckenov, A. A.; Brenes, R.; Abdi-Jalebi, M.; Bulović, V.; Bakr, O. M.; Barnard, E. S.; Stranks, S. D., Probing buried recombination pathways in perovskite structures using 3D photoluminescence tomography. *Energy & Environmental Science* **2018**, *11* (10), 2846-2852.
79. Sheng, C. X.; Zhang, C.; Zhai, Y. X.; Mielczarek, K.; Wang, W. W.; Ma, W. L.; Zakhidov, A.; Vardeny, Z. V., Exciton versus Free Carrier Photogeneration in Organometal Trihalide Perovskites Probed by Broadband Ultrafast Polarization Memory Dynamics. *Physical Review Letters* **2015**, *114* (11).
80. Zhai, Y. X.; Sheng, C. X.; Zhang, C.; Vardeny, Z. V., Ultrafast Spectroscopy of Photoexcitations in Organometal Trihalide Perovskites. *Advanced Functional Materials* **2016**, *26* (10), 1617-1627.
81. Johnston, M. B.; Herz, L. M., Hybrid Perovskites for Photovoltaics: Charge-Carrier Recombination, Diffusion, and Radiative Efficiencies. *Accounts of Chemical Research* **2016**, *49* (1), 146-154.
82. Yang, Y.; Yang, M.; Li, Z.; Crisp, R.; Zhu, K.; Beard, M. C., Comparison of Recombination Dynamics in CH<sub>3</sub>NH<sub>3</sub>PbBr<sub>3</sub> and CH<sub>3</sub>NH<sub>3</sub>PbI<sub>3</sub> Perovskite Films: Influence of Exciton Binding Energy. *The Journal of Physical Chemistry Letters* **2015**, *6* (23), 4688-4692.
83. Hangleiter, A.; Häcker, R., Enhancement of band-to-band Auger recombination by electron-hole correlations. *Physical Review Letters* **1990**, *65* (2), 215-218.
84. Zhao, W. J.; Ghorannevis, Z.; Chu, L. Q.; Toh, M. L.; Kloc, C.; Tan, P. H.; Eda, G., Evolution of Electronic Structure in Atomically Thin Sheets of WS<sub>2</sub> and WSe<sub>2</sub>. *Acs Nano* **2013**, *7* (1), 791-797.
85. Snellenburg, J.; Laptенок, S.; Seger, R.; M Mullen, K.; Van Stokkum, I., *Glotaran: A Java-based graphical user interface for the R package TIMP*. 2012; Vol. 49, p 1-22.
86. Akselrod, G. M.; Deotare, P. B.; Thompson, N. J.; Lee, J.; Tisdale, W. A.; Baldo, M. A.; Menon, V. M.; Bulović, V., Visualization of exciton transport in ordered and disordered molecular solids. *Nature Communications* **2014**, *5*, 3646.
87. Chong, S.; Min, W.; Xie, X. S., Ground-State Depletion Microscopy: Detection Sensitivity of Single-Molecule Optical Absorption at Room Temperature. *The Journal of Physical Chemistry Letters* **2010**, *1* (23), 3316-3322.
88. Blatter, G.; Greuter, F., Carrier transport through grain boundaries in semiconductors. *Physical Review B* **1986**, *33* (6), 3952-3966.
89. Gaury, B.; Haney, P. M., Charged Grain Boundaries and Carrier Recombination in Polycrystalline Thin-Film Solar Cells. *Phys. Rev. Applied* **2017**, *8* (5), 054026.
90. Lee, M. M.; Teuscher, J.; Miyasaka, T.; Murakami, T. N.; Snaith, H. J., Efficient hybrid solar cells based on meso-superstructured organometal halide perovskites. *Science* **2012**, *338* (6107), 643-647.
91. Burschka, J.; Pellet, N.; Moon, S.-J.; Humphry-Baker, R.; Gao, P.; Nazeeruddin, M. K.; Grätzel, M., Sequential deposition as a route to high-performance perovskite-sensitized solar cells. *Nature* **2013**, *499* (7458), 316-319.
92. Liu, D.; Kelly, T. L., Perovskite solar cells with a planar heterojunction structure prepared using room-temperature solution processing techniques. *Nature Photonics* **2014**, *8* (2), 133-138.

93. Jeon, N. J.; Noh, J. H.; Yang, W. S.; Kim, Y. C.; Ryu, S.; Seo, J.; Seok, S. I., Compositional engineering of perovskite materials for high-performance solar cells. *Nature* **2015**, *517* (7535), 476-480.
94. Tsai, H.; Nie, W.; Blancon, J.-C.; Stoumpos, C. C.; Asadpour, R.; Harutyunyan, B.; Neukirch, A. J.; Verduzco, R.; Crochet, J. J.; Tretiak, S.; Pedesseau, L.; Even, J.; Alam, M. A.; Gupta, G.; Lou, J.; Ajayan, P. M.; Bedzyk, M. J.; Kanatzidis, M. G.; Mohite, A. D., High-efficiency two-dimensional Ruddlesden–Popper perovskite solar cells. *Nature* **2016**, *536* (7616), 312-316.
95. Saliba, M.; Matsui, T.; Domanski, K.; Seo, J.-Y.; Ummadisingu, A.; Zakeeruddin, S. M.; Correa-Baena, J.-P.; Tress, W. R.; Abate, A.; Hagfeldt, A., Incorporation of rubidium cations into perovskite solar cells improves photovoltaic performance. *Science* **2016**, *354* (6309), 206-209.
96. McMeekin, D. P.; Sadoughi, G.; Rehman, W.; Eperon, G. E.; Saliba, M.; Hörantner, M. T.; Haghighirad, A.; Sakai, N.; Korte, L.; Rech, B., A mixed-cation lead mixed-halide perovskite absorber for tandem solar cells. *Science* **2016**, *351* (6269), 151-155.
97. Wehrenfennig, C.; Eperon, G. E.; Johnston, M. B.; Snaith, H. J.; Herz, L. M., High Charge Carrier Mobilities and Lifetimes in Organolead Trihalide Perovskites. *Advanced Materials* **2013**, *26* (10), 1584-1589.
98. Manser, J. S.; Kamat, P. V., Band filling with free charge carriers in organometal halide perovskites. *Nature Photonics* **2014**, *8* (9), 737-743.
99. Chen, K.; Barker, A. J.; Morgan, F. L. C.; Halpert, J. E.; Hodgkiss, J. M., Effect of Carrier Thermalization Dynamics on Light Emission and Amplification in Organometal Halide Perovskites. *J. Phys. Chem. Lett.* **2015**, *6* (1), 153-158.
100. Chen, Y.; Yi, H. T.; Wu, X.; Haroldson, R.; Gartstein, Y. N.; Rodionov, Y. I.; Tikhonov, K. S.; Zakhidov, A.; Zhu, X. Y.; Podzorov, V., Extended carrier lifetimes and diffusion in hybrid perovskites revealed by Hall effect and photoconductivity measurements. *Nature Communications* **2016**, *7*, 12253.
101. Herz, L. M., Charge-Carrier Dynamics in Organic-Inorganic Metal Halide Perovskites. *Annu. Rev. Phys. Chem.* **2016**, *67* (1), 65-89.
102. Chen, T.; Chen, W.-L.; Foley, B. J.; Lee, J.; Ruff, J. P. C.; Ko, J. Y. P.; Brown, C. M.; Harriger, L. W.; Zhang, D.; Park, C.; Yoon, M.; Chang, Y.-M.; Choi, J. J.; Lee, S.-H., Origin of long lifetime of band-edge charge carriers in organic–inorganic lead iodide perovskites. *Proceedings of the National Academy of Sciences* **2017**, *114* (29), 7519-7524.
103. Dong, Q.; Fang, Y.; Shao, Y.; Mulligan, P.; Qiu, J.; Cao, L.; Huang, J., Electron-hole diffusion lengths > 175  $\mu\text{m}$  in solution-grown  $\text{CH}_3\text{NH}_3\text{PbI}_3$  single crystals. *Science* **2015**, *347* (6225), 967-970.
104. Nie, W.; Tsai, H.; Asadpour, R.; Blancon, J.-C.; Neukirch, A. J.; Gupta, G.; Crochet, J. J.; Chhowalla, M.; Tretiak, S.; Alam, M. A.; Wang, H.-L.; Mohite, A. D., High-efficiency solution-processed perovskite solar cells with millimeter-scale grains. *Science* **2015**, *347* (6221), 522-525.
105. Xing, G.; Mathews, N.; Sun, S.; Lim, S. S.; Lam, Y. M.; Grätzel, M.; Mhaisalkar, S.; Sum, T. C., Long-range balanced electron-and hole-transport lengths in organic-inorganic  $\text{CH}_3\text{NH}_3\text{PbI}_3$ . *Science* **2013**, *342* (6156), 344-347.

106. Shi, D.; Adinolfi, V.; Comin, R.; Yuan, M.; Alarousu, E.; Buin, A.; Chen, Y.; Hoogland, S.; Rothenberger, A.; Katsiev, K.; Losovyj, Y.; Zhang, X.; Dowben, P. A.; Mohammed, O. F.; Sargent, E. H.; Bakr, O. M., Low trap-state density and long carrier diffusion in organolead trihalide perovskite single crystals. *Science* **2015**, *347* (6221), 519-522.
107. Guo, Z.; Manser, J. S.; Wan, Y.; Kamat, P. V.; Huang, L., Spatial and temporal imaging of long-range charge transport in perovskite thin films by ultrafast microscopy. *Nature Communications* **2015**, *6*, 7471.
108. Liu, S.; Wang, L.; Lin, W.-C.; Sucharitakul, S.; Burda, C.; Gao, X. P. A., Imaging the Long Transport Lengths of Photo-generated Carriers in Oriented Perovskite Films. *Nano Lett.* **2016**, *16* (12), 7925-7929.
109. Leijtens, T.; Eperon, G. E.; Barker, A. J.; Grancini, G.; Zhang, W.; Ball, J. M.; Kandada, A. R. S.; Snaith, H. J.; Petrozza, A., Carrier trapping and recombination: the role of defect physics in enhancing the open circuit voltage of metal halide perovskite solar cells. *Energy Environ. Sci.* **2016**, *9* (11), 3472-3481.
110. Yi, H. T.; Wu, X.; Zhu, X.; Podzorov, V., Intrinsic Charge Transport across Phase Transitions in Hybrid Organo-Inorganic Perovskites. *Adv Mater* **2016**, *28* (30), 6509-14.
111. Brenner, T. M.; Egger, D. A.; Kronik, L.; Hodes, G.; Cahen, D., Hybrid organic—inorganic perovskites: low-cost semiconductors with intriguing charge-transport properties. *Nat. Rev. Mater.* **2016**, *1* (1), 15007.
112. Lee, J.-W.; Bae, S.-H.; De Marco, N.; Hsieh, Y.-T.; Dai, Z.; Yang, Y., The role of grain boundaries in perovskite solar cells. *Materials Today Energy* **2017**.
113. Jankowska, J.; Long, R.; Prezhdo, O. V., Quantum Dynamics of Photogenerated Charge Carriers in Hybrid Perovskites: Dopants, Grain Boundaries, Electric Order, and Other Realistic Aspects. *ACS Energy Letters* **2017**, *2* (7), 1588-1597.
114. Li, W.; Liu, J.; Bai, F.-Q.; Zhang, H.-X.; Prezhdo, O. V., Hole Trapping by Iodine Interstitial Defects Decreases Free Carrier Losses in Perovskite Solar Cells: A Time-Domain Ab Initio Study. *ACS Energy Letters* **2017**, *2* (6), 1270-1278.
115. Chu, Z.; Yang, M.; Schulz, P.; Wu, D.; Ma, X.; Seifert, E.; Sun, L.; Li, X.; Zhu, K.; Lai, K., Impact of grain boundaries on efficiency and stability of organic-inorganic trihalide perovskites. *Nature Communications* **2017**, *8* (1), 2230.
116. Sherkar, T. S.; Momblona, C.; Gil-Escrig, L.; Ávila, J.; Sessolo, M.; Bolink, H. J.; Koster, L. J. A., Recombination in Perovskite Solar Cells: Significance of Grain Boundaries, Interface Traps, and Defect Ions. *ACS Energy Lett.* **2017**, *2* (5), 1214-1222.
117. Shih, M. C.; Li, S. S.; Hsieh, C.-H.; Wang, Y.-C.; Yang, H.-D.; Chiu, Y. P.; Chang, C.-S.; Chen, C. W., Spatially Resolved Imaging on Photocarrier Generations and Band Alignments at Perovskite/PbI<sub>2</sub> Heterointerfaces of Perovskite Solar Cells by Light-Modulated Scanning Tunneling Microscopy. *Nano Lett.* **2017**, *17* (2), 1154-1160.
118. deQuilettes, D. W.; Vorpahl, S. M.; Stranks, S. D.; Nagaoka, H.; Eperon, G. E.; Ziffer, M. E.; Snaith, H. J.; Ginger, D. S., Impact of microstructure on local carrier lifetime in perovskite solar cells. *Science* **2015**, *348* (6235), 683-686.
119. Simpson, M. J.; Doughty, B.; Yang, B.; Xiao, K.; Ma, Y.-Z., Imaging Electronic Trap States in Perovskite Thin Films with Combined Fluorescence and Femtosecond Transient Absorption Microscopy. *J. Phys. Chem. Lett.* **2016**, *7* (9), 1725-1731.
120. Draguta, S.; Thakur, S.; Morozov, Y. V.; Wang, Y.; Manser, J. S.; Kamat, P. V.; Kuno, M., Spatially Non-uniform Trap State Densities in Solution-Processed Hybrid Perovskite Thin Films. *J. Phys. Chem. Lett.* **2016**, *7* (4), 715-721.

121. Tian, W.; Cui, R.; Leng, J.; Liu, J.; Li, Y.; Zhao, C.; Zhang, J.; Deng, W.; Lian, T.; Jin, S., Limiting Perovskite Solar Cell Performance by Heterogeneous Carrier Extraction. *Angewandte Chemie* **2016**, *128* (42), 13261-13265.
122. Draguta, S.; Christians, J. A.; Morozov, Y. V.; Mucunzi, A.; Manser, J. S.; Kamat, P. V.; Luther, J. M.; Kuno, M., A quantitative and spatially resolved analysis of the performance-bottleneck in high efficiency, planar hybrid perovskite solar cells. *Energy Environ. Sci.* **2018**, *116*, 12956.
123. Nah, S.; Spokoyny, B.; Jiang, X.; Stoumpos, C.; Soe, C. M. M.; Kanatzidis, M. G.; Harel, E., Transient Sub-bandgap States in Halide Perovskite Thin Films. *Nano Lett.* **2018**, *18* (2), 827-831.
124. Gujar, T. P.; Unger, T.; Schonleber, A.; Fried, M.; Panzer, F.; van Smaalen, S.; Kohler, A.; Thelakkat, M., The role of PbI<sub>2</sub> in CH<sub>3</sub>NH<sub>3</sub>PbI<sub>3</sub> perovskite stability, solar cell parameters and device degradation. *Physical Chemistry Chemical Physics* **2018**, *20* (1), 605-614.
125. Saliba, M.; Correa-Baena, J.-P.; Grätzel, M.; Hagfeldt, A.; Abate, A., Perovskite Solar Cells: From the Atomic Level to Film Quality and Device Performance. *Angewandte Chemie International Edition* **2018**, *53*, 3151.
126. MacDonald, G. A.; Heveran, C. M.; Yang, M.; Moore, D.; Zhu, K.; Ferguson, V. L.; Killgore, J. P.; DelRio, F. W., Determination of the True Lateral Grain Size in Organic-Inorganic Halide Perovskite Thin Films. *ACS Appl. Mater. Interfaces* **2017**, *9* (39), 33565-33570.
127. Du, T.; Burgess, C. H.; Kim, J.; Zhang, J.; Durrant, J. R.; McLachlan, M. A., Formation, location and beneficial role of PbI<sub>2</sub> in lead halide perovskite solar cells. *Sustainable Energy & Fuels* **2017**, *1* (1), 119-126.
128. Jacobsson, T. J.; Correa-Baena, J.-P.; Halvani Anaraki, E.; Philippe, B.; Stranks, S. D.; Bouduban, M. E. F.; Tress, W.; Schenk, K.; Teuscher, J.; Moser, J.-E.; Rensmo, H.; Hagfeldt, A., Unreacted PbI<sub>2</sub> as a Double-Edged Sword for Enhancing the Performance of Perovskite Solar Cells. *Journal of the American Chemical Society* **2016**, *138* (32), 10331-10343.
129. Yang, M.; Zhou, Y.; Zeng, Y.; Jiang, C. S.; Padture, N. P.; Zhu, K., Square-Centimeter Solution-Processed Planar CH<sub>3</sub>NH<sub>3</sub>PbI<sub>3</sub> Perovskite Solar Cells with Efficiency Exceeding 15%. *Advanced Materials* **2015**, *27* (41), 6363-6370.
130. Ziang, X.; Shifeng, L.; Laixiang, Q.; Shuping, P.; Wei, W.; Yu, Y.; Li, Y.; Zhijian, C.; Shufeng, W.; Honglin, D.; Minghui, Y.; Qin, G. G., Refractive index and extinction coefficient of CH<sub>3</sub>NH<sub>3</sub>PbI<sub>3</sub> studied by spectroscopic ellipsometry. *Optical Materials Express* **2015**, *5* (1), 29-43.
131. D'Innocenzo, V.; Srimath Kandada, A. R.; De Bastiani, M.; Gandini, M.; Petrozza, A., Tuning the Light Emission Properties by Band Gap Engineering in Hybrid Lead Halide Perovskite. *Journal of the American Chemical Society* **2014**, *136* (51), 17730-17733.
132. Guo, Z.; Wan, Y.; Yang, M. J.; Snaider, J.; Zhu, K.; Huang, L. B., Long-range hot-carrier transport in hybrid perovskites visualized by ultrafast microscopy. *Science* **2017**, *356* (6333), 59-+.
133. Frost, J. M., Calculating polaron mobility in halide perovskites. *Phys. Rev. B* **2017**, *96* (19), 195202.

134. Xing, G.; Mathews, N.; Sun, S.; Lim, S. S.; Lam, Y. M.; Grätzel, M.; Mhaisalkar, S.; Sum, T. C., Long-Range Balanced Electron- and Hole-Transport Lengths in Organic-Inorganic  $\text{CH}_3\text{NH}_3\text{PbI}_3$ . *Science* **2013**, *342* (6156), 344.
135. MacDonald, G. A.; Yang, M.; Berweger, S.; Killgore, J. P.; Kabos, P.; Berry, J. J.; Zhu, K.; DelRio, F. W., Methylammonium lead iodide grain boundaries exhibit depth-dependent electrical properties. *Energy & Environmental Science* **2016**, *9* (12), 3642-3649.
136. Alberi, K.; Fluegel, B.; Moutinho, H.; Dhere, R. G.; Li, J. V.; Mascarenhas, A., Measuring long-range carrier diffusion across multiple grains in polycrystalline semiconductors by photoluminescence imaging. *Nature Communications* **2013**, *4*, 2699.
137. Ross, R. T.; Nozik, A. J., EFFICIENCY OF HOT-CARRIER SOLAR-ENERGY CONVERTERS. *Journal of Applied Physics* **1982**, *53* (5), 3813-3818.
138. Shah, J., HOT CARRIERS IN QUASI-2-D POLAR SEMICONDUCTORS. *Ieee Journal of Quantum Electronics* **1986**, *22* (9), 1728-1743.
139. Nozik, A. J., Spectroscopy and hot electron relaxation dynamics in semiconductor quantum wells and quantum dots. *Annu Rev Phys Chem* **2001**, *52* (1), 193-231.
140. Reggiani, L., *Hot-Electron Transport in Semiconductors*. Springer Berlin Heidelberg: Berlin, Heidelberg, 1985; Vol. 58.
141. Hu, B.; EA, d. S.; Knox, W.; Cunningham, J.; Nuss, M.; Kuznetsov, A.; Chuang, S., Identifying the distinct phases of carrier transport in semiconductors with 10 fs resolution. *Physical Review Letters* **1995**, *74* (9), 1689-1692.
142. Bernardi, M.; Vigil-Fowler, D.; Lischner, J.; Neaton, J. B.; Louie, S. G., Ab Initio Study of Hot Carriers in the First Picosecond after Sunlight Absorption in Silicon. *Physical Review Letters* **2014**, *112* (25).
143. Bernardi, M.; Vigil-Fowler, D.; Ong, C. S.; Neaton, J. B.; Louie, S. G., Ab initio study of hot electrons in GaAs. *Proceedings of the National Academy of Sciences of the United States of America* **2015**, *112* (17), 5291-5296.
144. Lock, D.; Rusimova, K. R.; Pan, T. L.; Palmer, R. E.; Sloan, P. A., Atomically resolved real-space imaging of hot electron dynamics. *Nature Communications* **2015**, *6*.
145. Dong, Q. F.; Fang, Y. J.; Shao, Y. C.; Mulligan, P.; Qiu, J.; Cao, L.; Huang, J. S., Electron-hole diffusion lengths  $> 175 \mu\text{m}$  in solution-grown  $\text{CH}_3\text{NH}_3\text{PbI}_3$  single crystals. *Science* **2015**, *347* (6225), 967-970.
146. Yang, Y.; Ostrowski, D. P.; France, R. M.; Zhu, K.; van de Lagemaat, J.; Luther, J. M.; Beard, M. C., Observation of a hot-phonon bottleneck in lead-iodide perovskites. *Nature Photonics* **2016**, *10* (1), 53-59.
147. Zhu, H. M.; Miyata, K.; Fu, Y. P.; Wang, J.; Joshi, P. P.; Niesner, D.; Williams, K. W.; Jin, S.; Zhu, X. Y., Screening in crystalline liquids protects energetic carriers in hybrid perovskites. *Science* **2016**, *353* (6306), 1409-1413.
148. Niesner, D.; Zhu, H.; Miyata, K.; Joshi, P. P.; Evans, T. J. S.; Kudisch, B. J.; Trinh, M. T.; Marks, M.; Zhu, X. Y., Persistent Energetic Electrons in Methylammonium Lead Iodide Perovskite Thin Films. *Journal of the American Chemical Society* **2016**, *138* (48), 15717-15726.
149. Chang, A. Y.; Cho, Y. J.; Chen, K. C.; Chen, C. W.; Kinaci, A.; Diroll, B. T.; Wagner, M. J.; Chan, M. K. Y.; Lin, H. W.; Schaller, R. D., Slow Organic- to- Inorganic Sub-Lattice Thermalization in Methylammonium Lead Halide Perovskites Observed by Ultrafast Photoluminescence. *Advanced Energy Materials* **2016**.

150. Li, M. J.; Bhaumik, S.; Goh, T. W.; Kumar, M. S.; Yantara, N.; Gratzel, M.; Mhaisalkar, S.; Mathews, N.; Sum, T. C., Slow cooling and highly efficient extraction of hot carriers in colloidal perovskite nanocrystals. *Nature Communications* **2017**, *8*.
151. Manser, J. S.; Kamat, P. V., Band filling with free charge carriers in organonietal halide perovskites. *Nature Photonics* **2014**, *8* (9), 737-743.
152. Chen, K.; Barker, A. J.; Morgan, F. L. C.; Halpert, J. E.; Hodgkiss, J. M., Effect of Carrier Thermalization Dynamics on Light Emission and Amplification in Organometal Halide Perovskites. *Journal of Physical Chemistry Letters* **2015**, *6* (1), 153-158.
153. Gabriel, M. M.; Kirschbrown, J. R.; Christesen, J. D.; Pinion, C. W.; Zigler, D. F.; Grumstrup, E. M.; Mehl, B. P.; Cating, E. E. M.; Cahoon, J. F.; Papanikolas, J. M., Direct Imaging of Free Carrier and Trap Carrier Motion in Silicon Nanowires by Spatially-Separated Femtosecond Pump-Probe Microscopy. *Nano Letters* **2013**, *13* (3), 1336-1340.
154. Kravtsov, V.; Ulbricht, R.; Atkin, J.; Raschke, M. B., Plasmonic nanofocused four-wave mixing for femtosecond near-field imaging. *Nature Nanotechnology* **2016**, *11* (5), 459-+.
155. Man, M. K. L.; Margiolakis, A.; Deckoff-Jones, S.; Harada, T.; Wong, E. L.; Krishna, M. B. M.; Madeo, J.; Winchester, A.; Lei, S.; Vajtai, R.; Ajayan, P. M.; Dani, K. M., Imaging the motion of electrons across semiconductor heterojunctions. *Nature Nanotechnology* **2017**, *12* (1), 36-40.
156. Yang, M.; Zhou, Y.; Zeng, Y.; Jiang, C.-S.; Padture, N. P.; Zhu, K., Square-Centimeter Solution-Processed Planar CH<sub>3</sub>NH<sub>3</sub>PbI<sub>3</sub> Perovskite Solar Cells with Efficiency Exceeding 15%. **2015**, *27* (41), 6363-6370.
157. Lu, J. G.; Fujita, S.; Kawaharamura, T.; Nishinaka, H.; Kamada, Y.; Ohshima, T.; Ye, Z. Z.; Zeng, Y. J.; Zhang, Y. Z.; Zhu, L. P.; He, H. P.; Zhao, B. H., Carrier concentration dependence of band gap shift in n-type ZnO:Al films. *Journal of Applied Physics* **2007**, *101* (8), 083705.
158. Price, M. B.; Butkus, J.; Jellicoe, T. C.; Sadhanala, A.; Briane, A.; Halpert, J. E.; Broch, K.; Hodgkiss, J. M.; Friend, R. H.; Deschler, F., Hot-carrier cooling and photoinduced refractive index changes in organic-inorganic lead halide perovskites. *Nature Communications* **2015**, *6*.
159. Trinh, M. T.; Wu, X. X.; Niesner, D.; Zhu, X. Y., Many-body interactions in photo-excited lead iodide perovskite. *Journal of Materials Chemistry A* **2015**, *3* (17), 9285-9290.
160. Jain, S. C.; McGregor, J. M.; Roulston, D. J., Band- gap narrowing in novel III- V semiconductors. *Journal of Applied Physics* **1990**, *68* (7), 3747-3749.
161. Kawai, H.; Giorgi, G.; Marini, A.; Yamashita, K., The Mechanism of Slow Hot-Hole Cooling in Lead-Iodide Perovskite: First-Principles Calculation on Carrier Lifetime from Electron–Phonon Interaction. *Nano Lett.* **2015**, *15* (5), 3103-3108.
162. Menéndez-Proupin, E.; Palacios, P.; Wahnón, P.; Conesa, J. C., Self-consistent relativistic band structure of the  $\text{CH}_3\text{NH}_3\text{PbI}_3$  perovskite. *Physical Review B* **2014**, *90* (4), 045207.
163. Reid, O. G.; Yang, M.; Kopidakis, N.; Zhu, K.; Rumbles, G., Grain-Size-Limited Mobility in Methylammonium Lead Iodide Perovskite Thin Films. *ACS Energy Lett.* **2016**, *1* (3), 561-565.
164. Brenner, T. M.; Egger, D. A.; Rappe, A. M.; Kronik, L.; Hodes, G.; Cahen, D., Are Mobilities in Hybrid Organic–Inorganic Halide Perovskites Actually “High”? *The Journal of Physical Chemistry Letters* **2015**, *6* (23), 4754-4757.

165. Brenner, T. M.; Egger, D. A.; Kronik, L.; Hodes, G.; Cahen, D., Hybrid organic—inorganic perovskites: low-cost semiconductors with intriguing charge-transport properties. *Nature Reviews Materials* **2016**, *1*, 15007.
166. Hayes, J.; Levi, A., Dynamics of extreme nonequilibrium electron transport in GaAs. *IEEE Journal of Quantum Electronics* **1986**, *22* (9), 1744-1752.
167. III, D. J. S.; Gupta, G.; Li, H.; Keller, S.; Mishra, U. K., Measurement of the hot electron mean free path and the momentum relaxation rate in GaN. **2014**, *105* (26), 263506.
168. Leheny, R. F.; Shah, J.; Fork, R. L.; Shank, C. V.; Migus, A., DYNAMICS OF HOT CARRIER COOLING IN PHOTOEXCITED GAAS. *Solid State Communications* **1979**, *31* (11), 809-813.
169. Frost, J. M.; Whalley, L. D.; Walsh, A., Slow Cooling of Hot Polarons in Halide Perovskite Solar Cells. *ACS Energy Lett.* **2017**, *2* (12), 2647-2652.
170. Guo, Z.; Wu, X.; Zhu, T.; Zhu, X.; Huang, L., Electron–Phonon Scattering in Atomically Thin 2D Perovskites. *ACS Nano* **2016**, *10* (11), 9992-9998.
171. Yang, J.; Wen, X.; Xia, H.; Sheng, R.; Ma, Q.; Kim, J.; Tapping, P.; Harada, T.; Kee, T. W.; Huang, F.; Cheng, Y.-B.; Green, M.; Ho-Baillie, A.; Huang, S.; Shrestha, S.; Patterson, R.; Conibeer, G., Acoustic-optical phonon up-conversion and hot-phonon bottleneck in lead-halide perovskites. *Nature Communications* **2017**, *8*, 14120.
172. Monahan, D. M.; Guo, L.; Lin, J.; Dou, L.; Yang, P.; Fleming, G. R., Room-Temperature Coherent Optical Phonon in 2D Electronic Spectra of CH<sub>3</sub>NH<sub>3</sub>PbI<sub>3</sub> Perovskite as a Possible Cooling Bottleneck. *J. Phys. Chem. Lett.* **2017**, 3211-3215.
173. Fu, J.; Xu, Q.; Han, G.; Wu, B.; Huan, C. H. A.; Leek, M. L.; Sum, T. C., Hot carrier cooling mechanisms in halide perovskites. *Nature Communications* **2017**, *8* (1), 1300.
174. Conibeer, G.; Ekins-Daukes, N.; Guillemoles, J.-F.; König, D.; Cho, E.-C.; Jiang, C.-W.; Shrestha, S.; Green, M., Progress on hot carrier cells. *Solar Energy Materials and Solar Cells* **2009**, *93* (6-7), 713-719.
175. Ridley, B. K., Hot phonons in high-field transport. *Semicond. Sci. Technol.* **1989**, *4* (12), 1142-1150.
176. Lazzeri, M.; Piscanec, S.; Mauri, F.; Ferrari, A. C.; Robertson, J., Electron Transport and Hot Phonons in Carbon Nanotubes. *Phys. Rev. Lett.* **2005**, *95* (23), 236802.
177. Reggiani, L., *Hot-Electron Transport in Semiconductors*. Springer: Berlin, 2006; p 275.
178. Pop, E., Energy dissipation and transport in nanoscale devices. *Nano Res.* **2010**, *3* (3), 147-169.
179. Von der Linde, D.; Lambrich, R., Direct measurement of hot-electron relaxation by picosecond spectroscopy. *Physical Review Letters* **1979**, *42* (16), 1090.
180. Shah, J., Photoexcited hot carriers: From cw to 6 fs in 20 years. *Solid state electronics* **1989**, *32* (12), 1051-1056.
181. Leitenstorfer, A.; Hunsche, S.; Shah, J.; Nuss, M. C.; Knox, W. H., Femtosecond high-field transport in compound semiconductors. *Phys. Rev. B* **2000**, *61* (24), 16642-16652.
182. Paulavičius, G.; Mitin, V. V.; Bannov, N. A., Coupled electron and nonequilibrium optical phonon transport in a GaAs quantum well. *Journal of Applied Physics* **1998**, *82* (11), 5580-5588.
183. Massaro, E. S.; Hill, A. H.; Grumstrup, E. M., Super-Resolution Structured Pump–Probe Microscopy. *ACS Photonics* **2016**, *3* (4), 501-506.

184. Man, M. K.; Margiolakis, A.; Deckoff-Jones, S.; Harada, T.; Wong, E. L.; Krishna, M. B.; Madeo, J.; Winchester, A.; Lei, S.; Vajtai, R.; Ajayan, P. M.; Dani, K. M., Imaging the motion of electrons across semiconductor heterojunctions. *Nat Nanotechnol* **2017**, *12* (1), 36-40.
185. Liao, B.; Najafi, E.; Li, H.; Minnich, A. J.; Zewail, A. H., Photo-excited hot carrier dynamics in hydrogenated amorphous silicon imaged by 4D electron microscopy. *Nature Nanotechnology* **2017**, *12*, 871.
186. Fu, Y.; Wu, T.; Wang, J.; Zhai, J.; Shearer, M. J.; Zhao, Y.; Hamers, R. J.; Kan, E.; Deng, K.; Zhu, X. Y.; Jin, S., Stabilization of the Metastable Lead Iodide Perovskite Phase via Surface Functionalization. *Nano Letters* **2017**, *17* (7), 4405-4414.
187. Xie, L.-Q.; Chen, L.; Nan, Z.-A.; Lin, H.-X.; Wang, T.; Zhan, D.-P.; Yan, J.-W.; Mao, B.-W.; Tian, Z.-Q., Understanding the Cubic Phase Stabilization and Crystallization Kinetics in Mixed Cations and Halides Perovskite Single Crystals. *Journal of the American Chemical Society* **2017**, *139* (9), 3320-3323.
188. Zhang, M.; Yun, J. S.; Ma, Q.; Zheng, J.; Lau, C. F. J.; Deng, X.; Kim, J.; Kim, D.; Seidel, J.; Green, M. A.; Huang, S.; Ho-Baillie, A. W. Y., High-Efficiency Rubidium-Incorporated Perovskite Solar Cells by Gas Quenching. *ACS Energy Letters* **2017**, *2* (2), 438-444.
189. Philippe, B.; Saliba, M.; Correa-Baena, J.-P.; Cappel, U. B.; Turren-Cruz, S.-H.; Grätzel, M.; Hagfeldt, A.; Rensmo, H., Chemical Distribution of Multiple Cation (Rb<sup>+</sup>, Cs<sup>+</sup>, MA<sup>+</sup>, and FA<sup>+</sup>) Perovskite Materials by Photoelectron Spectroscopy. *Chemistry of Materials* **2017**, *29* (8), 3589-3596.
190. Richter, J. M.; Branchi, F.; de Almeida Camargo, F. V.; Zhao, B.; Friend, R. H.; Cerullo, G.; Deschler, F., Ultrafast carrier thermalization in lead iodide perovskite probed with two-dimensional electronic spectroscopy. *Nature Communications* **2017**, *8* (1), 376.
191. Ryan, J. F.; Taylor, R. A.; Turberfield, A. J.; Maciel, A.; Worlock, J. M.; Gossard, A. C.; Wiegmann, W., Time-Resolved Photoluminescence of Two-Dimensional Hot Carriers in GaAs-AlGaAs Heterostructures. *Phys. Rev. Lett.* **1984**, *53* (19), 1841-1844.
192. Miyata, K.; Meggiolaro, D.; Trinh, M. T.; Joshi, P. P.; Mosconi, E.; Jones, S. C.; De Angelis, F.; Zhu, X. Y., Large polarons in lead halide perovskites. *Science Advances* **2017**, *3* (8), e1701217.
193. Bretschneider, S. A.; Ivanov, I.; Wang, H. I.; Miyata, K.; Zhu, X.; Bonn, M., Quantifying Polaron Formation and Charge Carrier Cooling in Lead-Iodide Perovskites. **2018**, *30* (29), 1707312.
194. Emin, D., *Polarons*. Cambridge University Press: 2013.
195. Park, M.; Neukirch, A. J.; Reyes-Lillo, S. E.; Lai, M.; Ellis, S. R.; Dietze, D.; Neaton, J. B.; Yang, P.; Tretiak, S.; Mathies, R. A., Excited-state vibrational dynamics toward the polaron in methylammonium lead iodide perovskite. *Nature Communications* **2018**, *9* (1), 2525.
196. Miyata, K.; Atallah, T. L.; Zhu, X. Y., Lead halide perovskites: Crystal-liquid duality, phonon glass electron crystals, and large polaron formation. *Science Advances* **2017**, *3* (10), e1701469.
197. Hill, A. H.; Smyser, K. E.; Kennedy, C. L.; Massaro, E. S.; Grumstrup, E. M., Screened Charge Carrier Transport in Methylammonium Lead Iodide Perovskite Thin Films. *The Journal of Physical Chemistry Letters* **2017**, *8* (5), 948-953.

198. Snaider, J. M.; Guo, Z.; Wang, T.; Yang, M.; Yuan, L.; Zhu, K.; Huang, L., Ultrafast Imaging of Carrier Transport across Grain Boundaries in Hybrid Perovskite Thin Films. *ACS Energy Letters* **2018**, *3* (6), 1402-1408.
199. Jacoboni, C.; Reggiani, L., The Monte Carlo method for the solution of charge transport in semiconductors with applications to covalent materials. *Reviews of Modern Physics* **1983**, *55* (3), 645-705.
200. Schüttler, H. B.; Holstein, T., Dynamics and transport of a large acoustic polaron in one dimension. *Annals of Physics* **1986**, *166* (1), 93-163.
201. Miyata, K.; Zhu, X. Y., Ferroelectric large polarons. *Nature Materials* **2018**, *17* (5), 379-381.
202. Katan, C.; Mohite, A. D.; Even, J., Entropy in halide perovskites. *Nature Materials* **2018**, *17* (5), 377-379.
203. Mickevičius, R.; Mitin, V.; Paulavičius, G.; Kochelap, V.; Strocio, M. A.; Iafrate, G. J., Hot-phonon effects on electron transport in quantum wires. *Journal of Applied Physics* **1996**, *80* (9), 5145-5149.
204. Li, W.; Wang, Z.; Deschler, F.; Gao, S.; Friend, R. H.; Cheetham, A. K., Chemically diverse and multifunctional hybrid organic-inorganic perovskites. *Nature Reviews Materials* **2017**, *2*, 16099.
205. Madjet, M. E.; Berdiyrov, G. R.; El-Mellouhi, F.; Alharbi, F. H.; Akimov, A. V.; Kais, S., Cation Effect on Hot Carrier Cooling in Halide Perovskite Materials. *The Journal of Physical Chemistry Letters* **2017**, *8* (18), 4439-4445.
206. Needleman, D. B.; Poindexter, J. R.; Kurchin, R. C.; Marius Peters, I.; Wilson, G.; Buonassisi, T., Economically sustainable scaling of photovoltaics to meet climate targets. *Energy & Environmental Science* **2016**, *9* (6), 2122-2129.
207. Song, Z.; McElvany, C. L.; Phillips, A. B.; Celik, I.; Krantz, P. W.; Wathage, S. C.; Liyanage, G. K.; Apul, D.; Heben, M. J., A techno-economic analysis of perovskite solar module manufacturing with low-cost materials and techniques. *Energy & Environmental Science* **2017**, *10* (6), 1297-1305.
208. Page, N. N. C. F. P. H. [www.nrel.gov/ncpv](http://www.nrel.gov/ncpv) (accessed July 30, 2016).
209. Eperon, G. E.; Stranks, S. D.; Menelaou, C.; Johnston, M. B.; Herz, L. M.; Snaith, H. J., Formamidinium lead trihalide: a broadly tunable perovskite for efficient planar heterojunction solar cells. *Energy & Environmental Science* **2014**, *7* (3), 982-988.
210. Lee, J.-W.; Kim, D.-H.; Kim, H.-S.; Seo, S.-W.; Cho, S. M.; Park, N.-G., Formamidinium and Cesium Hybridization for Photo- and Moisture-Stable Perovskite Solar Cell. *Advanced Energy Materials* **2015**, *5* (20), 1501310-n/a.
211. Li, Z.; Yang, M.; Park, J.-S.; Wei, S.-H.; Berry, J. J.; Zhu, K., Stabilizing Perovskite Structures by Tuning Tolerance Factor: Formation of Formamidinium and Cesium Lead Iodide Solid-State Alloys. *Chemistry of Materials* **2016**, *28* (1), 284-292.
212. Bi, D.; Tress, W.; Dar, M. I.; Gao, P.; Luo, J.; Renevier, C.; Schenk, K.; Abate, A.; Giordano, F.; Correa Baena, J.-P.; Decoppet, J.-D.; Zakeeruddin, S. M.; Nazeeruddin, M. K.; Grätzel, M.; Hagfeldt, A., Efficient luminescent solar cells based on tailored mixed-cation perovskites. *Science Advances* **2016**, *2* (1).
213. Yang, W. S.; Park, B.-W.; Jung, E. H.; Jeon, N. J.; Kim, Y. C.; Lee, D. U.; Shin, S. S.; Seo, J.; Kim, E. K.; Noh, J. H.; Seok, S. I., Iodide management in formamidinium-lead-halide-based perovskite layers for efficient solar cells. *Science* **2017**, *356* (6345), 1376-1379.

214. Yi, C.; Luo, J.; Meloni, S.; Boziki, A.; Ashari-Astani, N.; Gratzel, C.; Zakeeruddin, S. M.; Rothlisberger, U.; Gratzel, M., Entropic stabilization of mixed A-cation ABX<sub>3</sub> metal halide perovskites for high performance perovskite solar cells. *Energy & Environmental Science* **2016**, *9* (2), 656-662.
215. Saliba, M.; Matsui, T.; Seo, J.-Y.; Domanski, K.; Correa-Baena, J.-P.; Nazeeruddin, M. K.; Zakeeruddin, S. M.; Tress, W.; Abate, A.; Hagfeldt, A.; Gratzel, M., Cesium-containing triple cation perovskite solar cells: improved stability, reproducibility and high efficiency. *Energy & Environmental Science* **2016**, *9* (6), 1989-1997.
216. Pellet, N.; Gao, P.; Gregori, G.; Yang, T. Y.; Nazeeruddin, M. K.; Maier, J.; Grätzel, M., Mixed-Organic-Cation Perovskite Photovoltaics for Enhanced Solar-Light Harvesting. *Angewandte Chemie International Edition* **2014**, *53* (12), 3151-3157.
217. Saliba, M.; Matsui, T.; Domanski, K.; Seo, J.-Y.; Ummadisingu, A.; Zakeeruddin, S. M.; Correa-Baena, J.-P.; Tress, W. R.; Abate, A.; Hagfeldt, A.; Grätzel, M., Incorporation of rubidium cations into perovskite solar cells improves photovoltaic performance. *Science* **2016**, *354* (6309), 206-209.
218. Turren-Cruz, S.-H.; Saliba, M.; Mayer, M. T.; Juarez-Santiesteban, H.; Mathew, X.; Nienhaus, L.; Tress, W.; Erodici, M. P.; Sher, M.-J.; Bawendi, M. G.; Gratzel, M.; Abate, A.; Hagfeldt, A.; Correa-Baena, J.-P., Enhanced charge carrier mobility and lifetime suppress hysteresis and improve efficiency in planar perovskite solar cells. *Energy & Environmental Science* **2018**.
219. Bu, T.; Liu, X.; Zhou, Y.; Yi, J.; Huang, X.; Luo, L.; Xiao, J.; Ku, Z.; Peng, Y.; Huang, F.; Cheng, Y.-B.; Zhong, J., A novel quadruple-cation absorber for universal hysteresis elimination for high efficiency and stable perovskite solar cells. *Energy & Environmental Science* **2017**, *10* (12), 2509-2515.
220. Stuckelberger, M.; West, B.; Nietzold, T.; Lai, B.; Maser, J. M.; Rose, V.; Bertoni, M. I., Engineering solar cells based on correlative X-ray microscopy. *Journal of Materials Research* **2017**, *32* (10), 1825-1854.
221. McMeekin, D. P.; Sadoughi, G.; Rehman, W.; Eperon, G. E.; Saliba, M.; Hörantner, M. T.; Haghighirad, A.; Sakai, N.; Korte, L.; Rech, B.; Johnston, M. B.; Herz, L. M.; Snaith, H. J., A mixed-cation lead mixed-halide perovskite absorber for tandem solar cells. *Science* **2016**, *351* (6269), 151-155.
222. Jesper Jacobsson, T.; Correa-Baena, J.-P.; Pazoki, M.; Saliba, M.; Schenk, K.; Gratzel, M.; Hagfeldt, A., Exploration of the compositional space for mixed lead halogen perovskites for high efficiency solar cells. *Energy & Environmental Science* **2016**, *9* (5), 1706-1724.
223. Appavoo, K.; Nie, W.; Blancon, J.-C.; Even, J.; Mohite, A. D.; Sfeir, M. Y., Ultrafast optical snapshots of hybrid perovskites reveal the origin of multiband electronic transitions. *Physical Review B* **2017**, *96* (19), 195308.
224. Wong, J.; Huang, J. L.; Varlamov, S.; Green, M. A.; Evans, R.; Keevers, M.; Egan, R. J., Structural inhomogeneities in polycrystalline silicon on glass solar cells and their effects on device characteristics. *Progress in Photovoltaics: Research and Applications* **2011**, *19* (6), 695-705.

225. Correa Baena, J. P.; Steier, L.; Tress, W.; Saliba, M.; Neutzner, S.; Matsui, T.; Giordano, F.; Jacobsson, T. J.; Srimath Kandada, A. R.; Zakeeruddin, S. M.; Petrozza, A.; Abate, A.; Nazeeruddin, M. K.; Gratzel, M.; Hagfeldt, A., Highly efficient planar perovskite solar cells through band alignment engineering. *Energy & Environmental Science* **2015**, *8* (10), 2928-2934.
226. Levine, B. F., Quantum-well infrared photodetectors. *Journal of Applied Physics* **1993**, *74* (8), R1-R81.
227. Shuji, N.; Masayuki, S.; Shin-ichi, N.; Naruhito, I.; Takao, Y.; Toshio, M.; Hiroyuki, K.; Yasunobu, S., InGaN-Based Multi-Quantum-Well-Structure Laser Diodes. *Japanese Journal of Applied Physics* **1996**, *35* (1B), L74.
228. Hicks, L. D.; Dresselhaus, M. S., Effect of quantum-well structures on the thermoelectric figure of merit. *Physical Review B* **1993**, *47* (19), 12727-12731.
229. Ishihara, T.; Takahashi, J.; Goto, T., Exciton state in two-dimensional perovskite semiconductor  $(\text{C}_{10}\text{H}_{21}\text{NH}_3)_2\text{PbI}_4$ . *Solid State Communications* **1989**, *69* (9), 933-936.
230. Meresse, A.; Daoud, A., Bis(*n*-propylammonium) tetrachloroplumbate. *Acta Crystallographica Section C* **1989**, *45* (2), 194-196.
231. Mitzi, D. B.; Feild, C. A.; Harrison, W. T. A.; Guloy, A. M., Conducting tin halides with a layered organic-based perovskite structure. *Nature* **1994**, *369*, 467.
232. Mitzi, D. B.; Wang, S.; Feild, C. A.; Chess, C. A.; Guloy, A. M., Conducting Layered Organic-inorganic Halides Containing <110>-Oriented Perovskite Sheets. *Science* **1995**, *267* (5203), 1473-1476.
233. Papavassiliou, G. C., Three- and low-dimensional inorganic semiconductors. *Progress in Solid State Chemistry* **1997**, *25* (3-4), 125-270.
234. Borriello, I.; Cantele, G.; Ninno, D., Ab initio investigation of hybrid organic-inorganic perovskites based on tin halides. *Physical Review B* **2008**, *77* (23), 235214.
235. Lanty, G.; Jemli, K.; Wei, Y.; Leymarie, J.; Even, J.; Lauret, J. S.; Deleporte, E., Room-Temperature Optical Tunability and Inhomogeneous Broadening in 2D-Layered Organic-Inorganic Perovskite Pseudobinary Alloys. *Journal of Physical Chemistry Letters* **2014**, *5* (22), 3958-63.
236. Mitzi, D. B., Templating and structural engineering in organic-inorganic perovskites. *J. Chem. Soc., Dalton Trans.* **2001**, *0* (1), 1-12.
237. Saparov, B.; Mitzi, D. B., Organic-Inorganic Perovskites: Structural Versatility for Functional Materials Design. *Chem. Rev.* **2016**, *116* (7), 4558-96.
238. Cohen, B.-E.; Wierzbowska, M.; Etgar, L., High efficiency quasi 2D lead bromide perovskite solar cells using various barrier molecules. *Sustainable Energy & Fuels* **2017**, *1* (9), 1935-1943.
239. Braun, M.; Tuffentsammer, W.; Wachtel, H.; Wolf, H. C., Pyrene as emitting chromophore in organic-inorganic lead halide-based layered perovskites with different halides. *Chem. Phys. Lett.* **1999**, *307* (5-6), 373-378.
240. Mitzi, D. B.; Chondroudis, K.; Kagan, C. R., Design, structure, and optical properties of organic-inorganic perovskites containing an oligothiophene chromophore. *Inorganic Chemistry* **1999**, *38* (26), 6246-6256.
241. Takeoka, Y.; Asai, K.; Rikukawa, M.; Sanui, K., Incorporation of conjugated polydiacetylene systems into organic-inorganic quantum-well structures. *Chem. Commun.* **2001**, (24), 2592-2593.

242. Era, M.; Yoneda, S.; Sano, T.; Noto, M., Preparation of amphiphilic poly(thiophene)s and their application for the construction of organic-inorganic superlattices. *Thin Solid Films* **2003**, *438-439*, 322-325.
243. Zhu, X. H.; Mercier, N.; Frere, P.; Blanchard, P.; Roncali, J.; Allain, M.; Pasquier, C.; Riou, A., Effect of mono- versus di-ammonium cation of 2,2'-bithiophene derivatives on the structure of organic-inorganic hybrid materials based on iodo metallates. *Inorg. Chem.* **2003**, *42* (17), 5330-5339.
244. Ema, K.; Inomata, M.; Kato, Y.; Kunugita, H.; Era, M., Nearly perfect triplet-triplet energy transfer from Wannier excitons to naphthalene in organic-inorganic hybrid quantum-well materials. *Phys. Rev. Lett.* **2008**, *100* (25), 257401.
245. Era, M.; Kobayashi, T.; Sakaguchi, K.; Tsukamoto, E.; Oishi, Y., Electric conduction of PbBr-based layered perovskite organic-inorganic superlattice having carbazole chromophore-linked ammonium molecule as an organic layer. *Org. Electron.* **2013**, *14* (5), 1313-1317.
246. Papavassiliou, G. C.; Mousdis, G. A.; Pagona, G.; Karousis, N.; Vidali, M.-S., Room temperature enhanced blue-green, yellow-orange and red phosphorescence from some compounds of the type  $(\text{CH}_3\text{NH}_3)_{n-1}(1\text{-naphthylmethyl ammonium})_2\text{Pb}_n(\text{Cl}_x\text{Br}_{1-x})_{3n+1}$  (with  $n=1, 2$  and  $0 \leq x \leq 1$ ) and related observations from similar compounds. *J. Lumin.* **2014**, *149*, 287-291.
247. Evans, H. A.; Lehner, A. J.; Labram, J. G.; Fabini, D. H.; Barreda, O.; Smock, S. R.; Wu, G.; Chabynyc, M. L.; Seshadri, R.; Wudl, F., (TTF)Pb<sub>2</sub>I<sub>5</sub>: A Radical Cation-Stabilized Hybrid Lead Iodide with Synergistic Optoelectronic Signatures. *Chem. Mater.* **2016**, *28* (11), 3607-3611.
248. Cortecchia, D.; Soci, C.; Cametti, M.; Petrozza, A.; Marti-Rujas, J., Crystal Engineering of a Two-Dimensional Lead-Free Perovskite with Functional Organic Cations by Second-Sphere Coordination. *Chempluschem* **2017**, *82* (5), 681-685.
249. Du, K. Z.; Tu, Q.; Zhang, X.; Han, Q. W.; Liu, J.; Zauscher, S.; Mitzi, D. B., Two-Dimensional Lead(II) Halide-Based Hybrid Perovskites Templated by Acene Alkylamines: Crystal Structures, Optical Properties, and Piezoelectricity. *Inorg. Chem.* **2017**, *56* (15), 9291-9302.
250. Davydov, A. S., *Theory of Molecular Excitons*. Springer: 1971.
251. Barford, W.; Bursill, R. J., Theory of molecular excitons in the phenyl-based organic semiconductors. *Chemical Physics Letters* **1997**, *268* (5-6), 535-540.
252. Wannier, G. H., The structure of electronic excitation levels in insulating crystals. *Physical Review* **1937**, *52* (3), 0191-0197.
253. Dou, L. T.; Wong, A. B.; Yu, Y.; Lai, M. L.; Kornienko, N.; Eaton, S. W.; Fu, A.; Bischak, C. G.; Ma, J.; Ding, T. N.; Ginsberg, N. S.; Wang, L. W.; Alivisatos, A. P.; Yang, P. D., Atomically thin two-dimensional organic-inorganic hybrid perovskites. *Science* **2015**, *349* (6255), 1518-1521.
254. Zhu, T.; Yuan, L.; Zhao, Y.; Zhou, M.; Wan, Y.; Mei, J.; Huang, L., Highly mobile charge-transfer excitons in two-dimensional WS<sub>2</sub>/tetracene heterostructures. *Science Advances* **2018**, *4* (1), eaao3104.

## VITA

Jordan Snaider was born on August 31<sup>st</sup>, 1992 in Atlantic Beach, New York. Jordan is the son of Carol Snaider and André Snaider, and the brother of Chad Snaider and Sydney Snaider. He graduated from Seaford High School (Seaford, NY) in 2010, then attended St. John's University to begin his career in chemistry. Jordan earned his B.S. in Chemistry in 2014 and M.S. in Chemistry in 2015, under the guidance of Professor Gina Florio. Shortly after his M.S. thesis defense, he began studying charge carrier transport in perovskite materials under the guidance of Professor Libai Huang at Purdue University in June of 2015. Jordan is engaged to Christina Berti and will be married on September 28<sup>th</sup>, 2019. Together, they have three beautiful cats named Pepper, Pumpkin, and Patches and love spending time with them. Jordan is planning to start his career working under the United States Department of the Navy in early 2019.

## PUBLICATIONS

- Wang, T#.; **Snaider, J#.**; Buonassisi, T.; Correa-Baena, J. P.; Huang, L.B., Hot Carrier Transport Enhanced by Phonon Bottleneck in Hybrid Perovskites (Manuscript submitted)
- **Snaider, J.**; Guo, Z.; Wang, T.; Yang, M. J.; Zhu, K.; Huang, L. B., Ultrafast Imaging of Carrier Transport across Grain Boundaries in Hybrid Perovskite Thin Films **ACS Energy Letters** 2018, 3, 6, 1402-1408. DOI:10.1021/acseenergylett.8b00560
- Gao, Y.; Shi, E; **Snaider, J.**; Shiring, B.; Liang, C.; Liebman-Pelaez, A.; Yoo, P.; Deng, S.; Zeller, M.; Boudouris, B.; Liao, P.; Zhu, C.; Yu, Y.; Savoie, B.; Huang, L.B.; Dou, L., Molecularly Engineered Organic-Inorganic Hybrid Perovskites Quantum Wells (Manuscript submitted – Nature Chemistry)
- Correa-Baena; Luo; Brenner; **Snaider**; Sun; Jensen; Nienhaus; Wieghold; Poindexter; Meng; Wang; Lai; Bawendi; Huang; Fenning; Buonassisi, Homogenization of Halide Distribution and Carrier Dynamics in Alloyed Organic-Inorganic Perovskites. **Science** 2019
- Guo, Z.; Wan, Y.; Yang, M. J.; **Snaider, J.**; Zhu, K.; Huang, L. B., Long-range hot-carrier transport in hybrid perovskites visualized by ultrafast microscopy. **Science** 2017, 356 (6333), 59-62 DOI: 10.1126/science.aam7744
- Norcross, S; Trull1, K; **Snaider, J**; Doan, S; Tat, K; Huang, L.B.; Tantama, M, Extending roGFP Emission via FRET Relay Enables Simultaneous Dual Compartment Ratiometric Redox Imaging in Live Cells. **ACS Sensors** 2017, 2 (11), 1721-1729 DOI: 10.1021/acssensors.7b00689
- Wilcox, D; **Snaider, J**; Mukherjee, S; Yuan, L; Huang, L.B.; Savoie, B; Boudouris, B., Tuning the Interfacial and Energetic Interactions between a Photoexcited Conjugated Polymer and Open-Shell Small Molecules. **Soft Matter** 2019

## RESEARCH

## REPORT

## SOLAR CELLS

# Long-range hot-carrier transport in hybrid perovskites visualized by ultrafast microscopy

Zhi Guo,<sup>1</sup> Yan Wan,<sup>1</sup> Mengjin Yang,<sup>2</sup> Jordan Snaider,<sup>1</sup> Kai Zhu,<sup>2</sup> Libai Huang<sup>1\*</sup>

The Shockley-Queisser limit for solar cell efficiency can be overcome if hot carriers can be harvested before they thermalize. Recently, carrier cooling time up to 100 picoseconds was observed in hybrid perovskites, but it is unclear whether these long-lived hot carriers can migrate long distance for efficient collection. We report direct visualization of hot-carrier migration in methylammonium lead iodide (CH<sub>3</sub>NH<sub>3</sub>PbI<sub>3</sub>) thin films by ultrafast transient absorption microscopy, demonstrating three distinct transport regimes. Quasiballistic transport was observed to correlate with excess kinetic energy, resulting in up to 230 nanometers transport distance that could overcome grain boundaries. The nonequilibrium transport persisted over tens of picoseconds and ~600 nanometers before reaching the diffusive transport limit. These results suggest potential applications of hot-carrier devices based on hybrid perovskites.

Hot (nonequilibrium) carrier thermalization is one of the major sources for efficiency loss in solar cells (*1*). Such loss can be reverted if the hot carriers can be harvested before they equilibrate with the lattice, and the ultimate thermodynamic limit on conversion efficiency can be increased from the Shockley-Queisser limit of 33% to about 66% (*1, 2*). The main challenge for harvesting hot carriers is the relatively short distance they travel before losing their excess energy to the lattice, typically on the picosecond time scale (*3–8*). Hybrid organic-inorganic metal halide perovskites, such as CH<sub>3</sub>NH<sub>3</sub>PbI<sub>3</sub>, have emerged to be a class of highly efficient solar cell materials with remarkable charge transport properties, achieving efficiency above 20% (*9–13*). Recently, ultrafast spectroscopic measurements have revealed surprisingly long-lived hot carriers on the order of 100 ps in these hybrid perovskites (*14–18*).

The remarkably long hot-carrier lifetime in the hybrid perovskites, about two to three orders of magnitude longer than in conventional semiconductors, raises the question of whether hot carriers can be harvested to overcome the Shockley-Queisser limit. However, the current understanding on hot-carrier transport in hybrid perovskites is limited, despite efforts that have been devoted to studying carrier cooling dynamics (*14–21*). In particular, the crucial parameter of hot-carrier transport length must be comparable to the thickness necessary for photon absorption.

To correctly evaluate the potential of hot-carrier perovskite solar cells, measurements to provide quantitative results on the length scales of hot-

carrier transport in relation to carrier cooling time scales are necessary. Combining microscopy techniques with ultrafast optical pumping can be an effective solution for achieving simultaneous temporal and spatial resolutions of carrier dynamics (*22–25*). Here, we report on a direct visualization of hot-carrier transport in CH<sub>3</sub>NH<sub>3</sub>PbI<sub>3</sub> thin films using ultrafast transient absorption microscopy (TAM) with 50-nm spatial precision and 300-fs temporal resolution. These experiments revealed three distinct transport regimes, specifically, quasiballistic transport for the initial hot carriers, nonequilibrium transport for the protected long-lived hot carriers, and diffusive transport for the cooled carriers.

We performed measurements on a uniform and highly crystalline CH<sub>3</sub>NH<sub>3</sub>PbI<sub>3</sub> perovskite thin film deposited on a SiO<sub>2</sub> substrate, and a scanning electron microscopy (SEM) image is shown in fig. S1 of the supplementary materials (SM) (*26*). Solar cell efficiencies of ~18% have been achieved by using films fabricated with the same procedure (*27*). The absorption and photoluminescence spectra of the thin film investigated are shown in fig. S2 (*26*).

We first carried out ensemble transient absorption measurements to establish spectroscopic signatures for hot carriers (Fig. 1). Immediately after photoexcitation, a photoinduced absorption (PIA, negative change of transmission  $\Delta T/T$ ) band centered at 1.58 eV was observed whose amplitude ( $|\Delta T/T|$ ) increased as the pump photon energy increased (Fig. 1A). Global analysis (Fig. 1B) indicates that this PIA band is associated with a broadened ground-state bleach (GSB, positive  $\Delta T/T$ ) band with a high-energy tail consistent with Fermi-Dirac distribution at high carrier temperature. The PIA band resulted from the shifting of the band-gap energy  $\Delta E_g$ , which was a com-

bination of band-gap renormalization effect (narrowing the band gap by  $\Delta E_{\text{RGN}}$ ) and Burstein-Moss effect (or band-filling, widening the band gap by  $\Delta E_{\text{BM}}$ ), as described by  $\Delta E_g = \Delta E_{\text{BM}} - \Delta E_{\text{RGN}}$  (*28*). Because  $\Delta E_{\text{BM}}$  would not take effect until the hot carriers relax to the band edge, the red-shifted PIA band at 1.58 eV at 0 ps was due to  $\Delta E_{\text{RGN}}$  predominantly. The amplitude of the PIA band increased as the pump photon energy increased, which could be explained by the decreased occupation of the states near the band edge leading to a decreased  $\Delta E_{\text{BM}}$ . Once carriers cooled down and  $\Delta E_{\text{BM}}$  settled in, the PIA band at 1.58 eV decayed and a blue-shifted PIA band was observed (fig. S3) (*26*). Based on these observations, we assigned the PIA band at 1.58 eV to hot carriers, in agreement with previous reports (*29, 30*).

$\Delta T/T$  of the PIA band had a different dependence on carrier density  $n$  than that of the GSB band when probed at 1.58 eV (Fig. 1C).  $\Delta T/T$  of the GSB band scaled linearly with  $n$ , whereas  $\Delta T/T$  of the PIA band was proportional to  $n^{1/2}$ . Because  $\Delta T/T$  of the PIA band scaled linearly with  $\Delta E_{\text{RGN}}$ , as empirically shown in (*14*), this observation indicated that  $\Delta E_{\text{RGN}} \propto n^{1/2}$ . A  $n^{1/2}$  dependence for  $\Delta E_{\text{RGN}}$  is generally expected when carriers are weakly interacting, but an  $n^{1/2}$  term must be included when carrier-carrier interactions become more important (*28, 31*). For instance, the  $n^{1/2}$  dependence becomes dominant at  $n > 10^{17} \text{ cm}^{-3}$  for GaAs (*32*). The  $n^{1/2}$  dependence observed here implies that carrier-carrier interactions are not negligible for CH<sub>3</sub>NH<sub>3</sub>PbI<sub>3</sub>.

The PIA band decayed with a ~400-fs time constant when excited at 3.14 eV (Fig. 1B), which has been assigned to the emission of the longitudinal optical phonons (*14, 21, 32*). The lifetime for the PIA band shortened to ~280 fs when the pump photon energy was reduced to 1.97 eV (Fig. S4) (*26*). The decay of the PIA band was accompanied by the growth of the GSB band at the band edge (Fig. 1D). Also shown in Fig. 1D is a second and slower cooling process with a time constant of ~78 ps. The much slower cooling phase has been ascribed to the protection of the energetic carriers by the formation of large polarons (*15, 16*), hot phonon effects (carrier density  $> 10^{18} \text{ cm}^{-3}$ ) (*14*), and optical-acoustic phonon scattering (*17*).

We imaged hot-carrier transport initiated by two different pump photon energies: 3.14 eV (1.49 eV above band gap) and 1.97 eV (0.32 eV above band gap) with a probe photon energy of 1.58 eV. The pump beam was held at a fixed position while the probe beam was scanned relative to the pump with a pair of galvanometer scanners to form an image (see more details in the SM, fig. S5) (*23, 26, 33*). The precision in determining carrier propagation distance was dictated by the smallest measurable change in the excited state population profiles and not directly by the diffraction limit (*34*). This limit is ~50 nm for the current experimental conditions, as discussed in the SM (*26*). The carrier density for these measurements was  $\sim 4 \times 10^{17} \text{ cm}^{-3}$ , where Auger recombination and hot phonon effect were negligible (fig. S6) (*16, 26, 33*).

<sup>1</sup>Department of Chemistry, Purdue University, West Lafayette, IN 47907, USA. <sup>2</sup>National Renewable Energy Laboratory, 15013 Denver West Parkway, Golden, CO 80401, USA. \*Corresponding author. Email: libai-huang@purdue.edu

# Ultrafast Imaging of Carrier Transport across Grain Boundaries in Hybrid Perovskite Thin Films

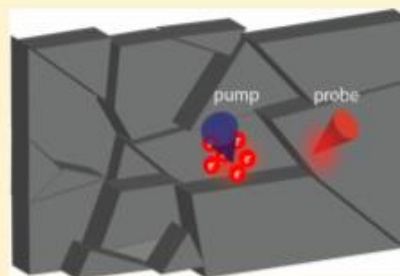
Jordan M. Snaider,<sup>†,‡,✉</sup> Zhi Guo,<sup>†,‡</sup> Ti Wang,<sup>†</sup> Mengjin Yang,<sup>‡</sup> Long Yuan,<sup>†</sup> Kai Zhu,<sup>‡,✉</sup> and Libai Huang<sup>✉,†,‡</sup>

<sup>†</sup>Department of Chemistry, Purdue University, West Lafayette, Indiana 47907, United States

<sup>‡</sup>Chemistry and Nanoscience Center, National Renewable Energy Laboratory, 15013 Denver West Parkway, Golden, Colorado 80401, United States

**S** Supporting Information

**ABSTRACT:** For optoelectronic devices based on polycrystalline semiconducting thin films, carrier transport across grain boundaries is an important process in defining efficiency. Here we employ transient absorption microscopy (TAM) to directly measure carrier transport within and across the boundaries in hybrid organic–inorganic perovskite thin films for solar cell applications with 50 nm spatial precision and 300 fs temporal resolution. By selectively imaging sub-bandgap states, our results show that lateral carrier transport is slowed down by these states at the grain boundaries. However, the long carrier lifetimes allow for efficient transport across the grain boundaries. The carrier diffusion constant is reduced by about a factor of 2 for micron-sized grain samples by the grain boundaries. For grain sizes on the order of ~200 nm, carrier transport over multiple grains has been observed within a time window of 5 ns. These observations explain both the shortened photoluminescence lifetimes at the boundaries as well as the seemingly benign nature of the grain boundaries in carrier generation.



Carrier transport in semiconductors is a crucial process that defines efficiency for optoelectronic devices including solar cells and light-emitting diodes. Many of these devices are fabricated from polycrystalline materials; therefore, transport across the grain boundaries is a major challenge in achieving optimal device performance.<sup>1,2</sup> Semiconducting hybrid organic–inorganic lead halide perovskites, such as CH<sub>3</sub>NH<sub>3</sub>PbI<sub>3</sub> (MAPbI<sub>3</sub>), have recently attracted significant research interest, motivated largely by the rapid rise in efficiency of solar cells, achieving above 22%.<sup>3–9</sup> The high efficiency of perovskite solar cells has been attributed to extraordinarily long carrier lifetimes,<sup>10–15</sup> long-range carrier diffusion,<sup>16–21</sup> and exceptional defect tolerance.<sup>22–25</sup> Because polycrystalline hybrid perovskite thin films employed in the solar cells are commonly grown by low-temperature solution processes, the formation of grain boundaries is inevitable.<sup>25</sup> The structural disorders at the boundaries could form defect states and potential barriers, leading to slow carrier transport.<sup>26,27</sup>

The impact of grain boundaries on carrier transport in hybrid perovskites has been indirectly demonstrated by the fact that the carrier diffusion lengths measured from polycrystalline thin films are significantly shorter than those of single crystals (a few

μm vs >100 μm).<sup>16–21</sup> Experimentally, grain boundaries are difficult to independently control and measure as they could depend on fabrication methods. More recently, scanning probe<sup>28–30</sup> and optical microscopy<sup>31–37</sup> approaches have been employed to spatially map carrier generation and dynamics at the grain boundaries. Recent theoretical studies have suggested that grain boundaries create shallow sub-bandgap states.<sup>26,38</sup> Despite these recent advances, the role of grain boundaries in hybrid perovskite thin films is currently under debate. Some have shown that the photoluminescence (PL) intensity of grain boundaries is overall weaker, exhibiting faster PL decays.<sup>37</sup> In contrast, others have reported that the PL lifetimes are not shorter compared to grain surfaces or grain interiors, which suggests that grain boundaries do not dominate nonradiative recombination in MAPbI<sub>3</sub> films.<sup>39–41</sup> Scanning probe measurements suggest that for encapsulated thin films with micron-sized grains grain boundaries are relatively benign to carrier generation and transport.<sup>28,42</sup> It has also been

Received: April 9, 2018

Accepted: May 21, 2018

Published: May 21, 2018

## Extending roGFP Emission via Förster-Type Resonance Energy Transfer Relay Enables Simultaneous Dual Compartment Ratiometric Redox Imaging in Live Cells

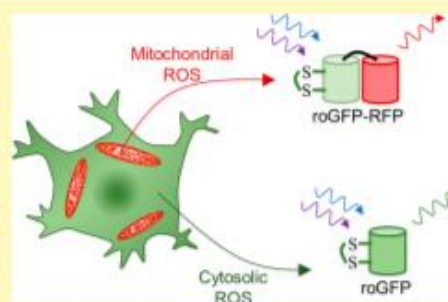
Stevie Norcross,<sup>†</sup> Keelan J. Trull,<sup>†</sup> Jordan Snaider,<sup>†</sup> Sara Doan,<sup>†</sup> Kiet Tat,<sup>†</sup> Libai Huang,<sup>†</sup> and Mathew Tantama<sup>\*,†,‡,§</sup>

<sup>†</sup>Department of Chemistry, <sup>‡</sup>Institute for Integrative Neuroscience, and <sup>§</sup>Institute of Inflammation, Immunology, and Infectious Disease, Purdue University, 560 Oval Drive, Box 68, West Lafayette, Indiana 47907, United States

 Supporting Information

**ABSTRACT:** Reactive oxygen species (ROS) mediate both intercellular and intraorganellar signaling, and ROS propagate oxidative stress between cellular compartments such as mitochondria and the cytosol. Each cellular compartment contains its own sources of ROS as well as antioxidant mechanisms, which contribute to dynamic fluctuations in ROS levels that occur during signaling, metabolism, and stress. However, the coupling of redox dynamics between cellular compartments has not been well studied because of the lack of available sensors to simultaneously measure more than one subcellular compartment in the same cell. Currently, the redox-sensitive green fluorescent protein, roGFP, has been used extensively to study compartment-specific redox dynamics because it provides a quantitative ratiometric readout and it is amenable to subcellular targeting as a genetically encoded sensor. Here, we report a new family of genetically encoded fluorescent protein sensors that extend the fluorescence emission of roGFP via Förster-type resonance energy transfer to an acceptor red fluorescent protein for dual-color live-cell microscopy. We characterize the redox and optical properties of the sensor proteins, and we demonstrate that they can be used to simultaneously measure cytosolic and mitochondrial ROS in living cells. Furthermore, we use these sensors to reveal cell-to-cell heterogeneity in redox coupling between the cytosol and mitochondria when neuroblastoma cells are exposed to reductive and metabolic stresses.

**KEYWORDS:** fluorescent protein, redox, reactive oxygen species, roGFP, FRET, ratiometric, live-cell imaging, mitochondria



Reduction–oxidation (redox) reactions must be kept in a careful balance in order to maintain healthy cell growth and function.<sup>1–3</sup> Loss of redox balance can lead to both reductive and oxidative stresses associated with aging, cancer, cardiovascular disease, and Parkinson's disease.<sup>4–7</sup> For example, reactive oxygen species (ROS), such as hydrogen peroxide (H<sub>2</sub>O<sub>2</sub>) and superoxide anion (O<sub>2</sub><sup>•−</sup>), can oxidize protein-bound cysteines and other molecular species during normal metabolism and signaling.<sup>8</sup> However, excess ROS can cause oxidative stress and damage that leads to loss of function or cell death. To prevent such pathologies, redox enzymes and cellular redox buffers such as glutathione (GSH) are critical for maintaining proper redox balance. Together, both enzymatic and nonenzymatic components make up a "redox network"<sup>1</sup> that contributes to homeostasis in the face of changing intracellular and environmental conditions faced by prokaryotes and eukaryotes.

Like metabolic and signaling networks, the redox network is spatially organized within a cell, and compartments such as the cytosol and mitochondria contain distinct sources of ROS as well as distinct antioxidant mechanisms involving redox

enzymes and redox buffers.<sup>1</sup> As a result, compartment-specific redox and ROS dynamics exist with varying degrees of cross-compartment coupling.<sup>9–12</sup> Redox coupling across compartments is a critical aspect of network response. For example, the production of mitochondrially derived cytosolic ROS plays an integral role in retrograde mitonuclear communication and stress response.<sup>13,14</sup> However, compartment-specific ROS dynamics and redox signaling between organelles has been poorly studied because of the lack of spectrally compatible redox probes that are available to simultaneously quantify redox in multiple compartments within the same living cell.

Currently, the redox-sensitive green fluorescent protein (roGFP) sensors are widely used to study redox biology across model species, including yeast, plants, and animals.<sup>15–21</sup> The roGFP sensors were originally developed by engineering two solvent-facing cysteines on the  $\beta$ -barrel of GFP.<sup>18</sup> Upon oxidation, the cysteines form a disulfide bond, causing a

Received: September 13, 2017

Accepted: October 26, 2017

Published: October 26, 2017